

# Radial structure, inflow and central mass of stationary radiative galaxy clusters

Curtis J. Saxton<sup>★</sup> and Kinwah Wu

*Mullard Space Science Laboratory, University College London, Holmbury St Mary, Dorking, Surrey RH5 6NT*

Accepted 2008 September 18. Received 2008 September 18; in original form 2008 June 11

## ABSTRACT

We analyse the radial structure of self-gravitating spheres consisting of multiple interpenetrating fluids, such as the X-ray emitting gas and the dark halo of a galaxy cluster. In these *dipolytropic* models, the adiabatic dark matter sits in equilibrium, while the gas develops a gradual, smooth, quasi-stationary cooling flow. Both affect and respond to the collective gravitational field. We find that all subsonic, radially continuous, steady solutions require a non-zero minimum central point mass. For Mpc-sized haloes with 7–10 effective degrees of freedom ( $F_2$ ), the minimum central mass is compatible with observations of supermassive black holes. Smaller gas mass influxes enable smaller central masses for wider ranges of  $F_2$ . The halo comprises a sharp spike around the central mass, embedded within a core of nearly constant density (at  $10^1$ – $10^{2.5}$  kpc scales), with outskirts that attenuate and naturally truncate at finite radius (several Mpc). The gas density resembles a broken power law in radius, but the temperature dips and peaks within the dark core. A finite minimum temperature occurs due to gravitational self-warming, without cold mass dropout nor needing regulatory heating. X-ray emission from the intracluster medium mimics a  $\beta$ -model plus bright compact nucleus. Near-sonic points in the gas flow are bottlenecks to the allowed steady solutions; the outermost are at kpc scales. These sites may preferentially develop cold mass dropout during strong perturbations off equilibrium. Within the sonic point, the profile of gas specific entropy is flatter than  $s \propto r^{1/2}$ , but this is a shallow ramp and not an isentropic core. When  $F_2$  is large, the inner halo spike is only marginally Jeans stable in the central parsec, suggesting that a large non-linear disturbance could trigger local dark collapse on to the central object.

**Key words:** accretion, accretion discs – hydrodynamics – cooling flows – galaxies: clusters: general – dark matter – X-rays: galaxies.

## 1 INTRODUCTION

Galaxy clusters consist of baryonic and dark matter in the cosmic ratio (Spergel et al. 2007). Black holes and the stars in galaxies and in the intracluster light only constitute a small (10–15 per cent) fraction of the baryons; and the intracluster X-ray emitting hot gas comprises the majority of the baryons (Lin, Mohr & Stanford 2003; Gonzalez, Zaritsky & Zabludoff 2007). Relaxed clusters are found to contain a round core of approximately constant density, attenuating into fringes below detection limits (Lea et al. 1973; Cavaliere & Fusco-Femiano 1976). There are also clusters with more centrally peaked core. They are thought to be systems with short radiative cooling time in comparison with the Hubble time. As radiative cooling causes the depletion of pressure support near the cluster centre, gas inevitably subsides inwards from the cluster outskirts, i.e. cooling

flows (Cowie & Binney 1977; Fabian & Nulsen 1977; Mathews & Bregman 1978).

Cooling flows have been linked with accretion onto, and star formation in the dominant galaxy in the cluster, and also the fuelling of their galactic nuclei (e.g. Silk 1976; Sarazin & O’Connell 1983; Fabian et al. 1984b; Nulsen, Stewart & Fabian 1984). Early models of cooling flow invoked a number of simple assumptions. In some fluid formulations for the cluster structure, a static global gravitational potential was used, and there was no consideration of gas or halo self-gravity. Kinetic and ram pressures were often not considered explicitly, and this caused a cooling runaway near the cluster centre, leading to a rapid deposition of a great amount of cold gas. Approximate deprojected cluster X-ray images indicated that the gas inflow rates  $\dot{m}$  diminishes nearer the cluster centre (Stewart et al. 1984; Thomas, Fabian & Nulsen 1987). This was taken as evidence for widely distributed ‘mass dropout’ – thermal instability spawning small, underpressured, invisibly cold clumps within a multiphase medium. Thermal conduction and magnetic

<sup>★</sup>E-mail: cjs2@mssl.ucl.ac.uk

fields were argued to be too weak to inhibit this instability and dropout.

The early cooling flow models were challenged by various multi-wavelength observations (see reviews by Donahue & Voit 2004; Peterson & Fabian 2006). First of all, radio and optical imaging have not shown the expected accumulations of cold gas, nor the expected bursts of star formation. Moreover, X-ray spectroscopic and imaging deprojections of cluster profiles indicates a temperature floor typically a factor of 3 or 4 below the peak temperature (Kaastra et al. 2001; Peterson et al. 2001; Tamura et al. 2001; Johnstone et al. 2002; Sakelliou et al. 2002; Peterson et al. 2003). In some systems the temperature even appears to increase at the smallest radii (e.g. O’Sullivan et al. 2007). Spectral analyses suggest that the intracluster medium (ICM) is likely to be single-phase (Böhringer et al. 2001; David et al. 2001; Molendi & Pizzolato 2001; Matsushita et al. 2002). These difficulties prompted the search of possible processes that could suppress the cooling flows, e.g. thermal conduction, or non-gravitational heating, such as the power injected by active galactic nuclei (AGN). (See review by Peterson & Fabian 2006, and references therein.) There are still open questions whether the heating processes can fine-tune to counteract the cooling stably, and whether the heating would distribute appropriately across the relevant regions in the cluster (Fabian et al. 1994; Johnstone et al. 2002; Brighenti & Mathews 2003; Conroy & Ostriker 2008).

Meanwhile, theories of halo structure have been overturned several times. Once, it was assumed that cluster dark matter follows the distribution of galaxies, in approximately isothermal, flat-cored assemblages (e.g. King 1966; Rood et al. 1972; Cavaliere & Fusco-Femiano 1976; Cowie & Binney 1977; Fabian et al. 1981). This view was naturally compatible with the classic signs (in the rotation profiles of disc galaxies) that galaxian dark matter is more shallowly and widely spread than the baryons. By the 1990s, cosmological  $N$ -body simulations were becoming fine enough to resolve cluster and galaxy haloes, under the simplifying assumption that dark matter acts like a collisionless stellar dynamical fluid (without any short- or long-range gauge fields of its own). Simulated haloes develop sharp power-law central density cusps, (see e.g. Dubinski & Carlberg 1991; Navarro, Frenk & White 1996; Moore et al. 1998; Diemand, Moore & Stadel 2004; Navarro et al. 2004; Diemand et al. 2005). The redistribution of cooling, contracting gas may steepen the dark cusp further (e.g. Blumenthal et al. 1986; Gnedin et al. 2004; Sellwood & McGaugh 2005).

In a circular way, cuspy profiles became an *ansatz* in the fitting cluster observations. Cuspy profiles have been assumed as templates in composite mass models fitted to gravitational lensing observations. It has been shown that a cuspy halo can hold a cored X-ray emitting gas distribution qualitatively similar to that of traditional cored halo models (Makino, Sasaki & Suto 1998). Gravitational lensing suggests flat cores in some clusters (Tyson, Kochanski & dell’Antonio 1998; Gavazzi et al. 2003; Sand et al. 2004, 2008). However, on galaxy scales, a considerable weight of evidence disfavours the existence dark cusps today (or implies that haloes are less centrally concentrated than baryons). These lines of evidence include velocity fields of dwarf and low surface brightness galaxies (Flores & Primack 1994; Moore 1994; Burkert 1995; de Blok & McGaugh 1997; Weldrake, de Blok & Walter 2003; de Blok 2005; Simon et al. 2005; Kuzio de Naray et al. 2006); and kinematics of dwarf spheroidal galaxies (Lokas 2002; Gilmore et al. 2007). Current observational data for dwarf spheroidal galaxies cannot rule out cuspy profiles from the kinematics alone (Walker et al. 2007), though tidal tracers hint circumstantially at gentle cores in specific

cases (Kleyna et al. 2003; Goerdt et al. 2006). Lensing analyses of isolated elliptical galaxies suggest cuspy profiles near the observed radii (Read et al. 2007), while the kinematics of other cases imply flat cores or low dark densities (Romanowsky et al. 2003; Douglas et al. 2007; Forestell & Gebhardt 2008). Possible explanations of the cusp problem may involve subtle numerical systematics of  $N$ -body methodology, extra dark physics, or some forms of gaseous, stellar or AGN feedback.

Feedback, if it is responsible for erasing cusps, must overturn a substantial fraction of a galaxy’s baryonic mass, from the deepest zone of its potential, without leaving abnormal metallicities and stellar populations. The implementation of feedback in numerical simulations suffers from severe challenges of resolution, and considerable arbitrariness or uncertainty in recipes for small-scale physics. Relevant fluid instabilities differ greatly between numerical schemes (e.g. Agertz et al. 2007). Energy budgets of popular Lagrangian hydrodynamics methods are broken by endemic (but rarely mentioned) ‘wall heating’ artefacts (e.g. Noh 1987), with unknowable consequences in simulated media where heating, cooling or thermal instability are important. A definitive answer to the ‘feedback’ question is far off; presently it is an almost unfalsifiable proposition.

This paper aims to present a new formalism for the structures of relaxed galaxy clusters, and to probe the scope of its initial implications for cooling flows and dark matter (reserving empirical detail and observational fits for future refinements). We re-examine the classic scenario of inflows in galaxy clusters with a more complete and consistent treatment of the gravitational interaction and energy exchanges in the gas and the dark matter components. Also a sensible polytropic equation of state is used for the dark matter that admits cusplike solutions for some systems and allows multiple degrees of freedom in the dark matter. Note that a polytropic halo may arise if dark matter has strong self-interactions (SIDM), or if the system is formulated properly in the framework of Tsallis’ statistical thermodynamics (cf. the Boltzmann statistical thermodynamics; Tsallis 1988; Plastino & Plastino 1993), or in collisionless systems with isotropic velocity distributions. We illustrate the properties and profiles of spherical, spatially continuous, stationary solutions relevant to cluster-sized systems. We quantify certain signature radii of these solutions, for the benefit of comparison with simpler models in the literature, and to inform future observational tests. Our solutions indicate that it is inevitable that point-like central masses would emerge in relaxed clusters, groups or pressure-supported galaxies. For some appropriate regimes of the halo microphysics, the predicted minimum central mass is consistent with those of supermassive black holes (SMBHs) in giant galaxies. We discuss implications for the rapid origin of SMBHs, monolithic condensation of early stellar populations in galaxies, and the problem of the central structures of dark haloes.

The paper is organized as follows. Section 2 gives the general formulation of the multicomponent self-gravitating systems, and the construction of the gas and dark matter dipolytropes. Next, Section 3 describes the valid solutions in the cluster parameter space, the properties of the solutions, their comparisons with current observations, and predictions to be tested by future observations. In Section 4 we discuss our results in the context of galaxy and cluster evolution. We conclude in Section 5. The appendices show the derivation of our model’s natural units, the normalization and the rescaling of the model, the interpretation of the effective degrees of freedom for the dark matter and comparisons between our model and other standard spherical models for clusters.

## 2 MULTICOMPONENT SELF-GRAVITATING SYSTEMS

### 2.1 Multifluid formulation

In our model the system has multiple components. It is self-gravitating, and the distinct components interact among each other through their shared gravitational potential. Each component,  $i$ , has its equation of state, which takes the form

$$p_i = \rho_i \sigma_i^2 = s_i \rho_i^{\gamma_i} \quad (1)$$

with partial pressure  $p_i$ , density  $\rho_i$ , isotropic velocity dispersion  $\sigma_i$  (which corresponds to an isothermal sound speed in the fluid description), specific entropy  $s_i$  and adiabatic index  $\gamma_i$ . The adiabatic index is related to an effective number of degrees of freedom  $F_i$  via

$$\gamma_i = 1 + \frac{2}{F_i}. \quad (2)$$

The mass, momentum and energy conservation equations read

$$\frac{\partial}{\partial t} \rho_i + \nabla \cdot \rho_i \mathbf{v}_i = 0, \quad (3)$$

$$\frac{\partial}{\partial t} \rho_i \mathbf{v}_i + \nabla \cdot \rho_i \mathbf{v}_i \mathbf{v}_i + \nabla \rho_i \sigma_i^2 = \rho_i \mathbf{f}_i, \quad (4)$$

$$\frac{\partial}{\partial t} \epsilon_i + \nabla \cdot (\epsilon_i + \rho_i \sigma_i^2) \mathbf{v}_i = \rho_i \mathbf{v}_i \cdot \mathbf{f}_i + \mathcal{L}_i, \quad (5)$$

where the energy density is

$$\epsilon_i \equiv \frac{\rho_i \sigma_i^2}{\gamma_i - 1} + \frac{1}{2} \rho_i v_i^2 = \frac{s_i \rho_i^{\gamma_i}}{\gamma_i - 1} + \frac{1}{2} \rho_i v_i^2. \quad (6)$$

Equivalently, the energy conservation equation (5) may be expressed in term of the entropy:

$$\frac{\partial}{\partial t} s_i + \mathbf{v}_i \cdot \nabla s_i = (\gamma_i - 1) \mathcal{L}_i \rho_i^{-\gamma_i}. \quad (7)$$

The variable  $\mathcal{L}_i$  is a volumetric power, which specifies the energy gains and losses. For a component net loss, say radiative cooling,  $\mathcal{L}_i < 0$ . We assume that  $\mathcal{L}_i$  is determined by the local thermodynamic and dynamic variables. This assumption is justified in cluster environments as the radiative processes are optically thin.

The gravitational potential,  $\Phi$ , satisfies the Poisson equation

$$\nabla^2 \Phi = 4\pi G \sum_i \rho_i. \quad (8)$$

The gravitational force is determined from the gravitational potential  $\mathbf{f} = -\nabla \Phi$  for all  $i$ , and the force field is the same for all the mass components.

### 2.2 Steady spherical solutions

In this paper we consider only stationary spherically symmetric systems. Time-dependent analysis will be discussed in Saxton, Wu & Ferreras (in preparation), and systems with more complicated geometries will be presented elsewhere. In a stationary spherically symmetric system, the density, velocity, temperature and gravitational field are functions of radial coordinate  $r$  only. The mass continuity equation (3) requires that density and velocity are related by

$$\dot{m}_i \equiv 4\pi r^2 \rho_i v_i. \quad (9)$$

For mass inflow  $\dot{m}_i < 0$ ; and for mass outflow  $\dot{m}_i > 0$ . A system in hydrostatic equilibrium has  $\dot{m}_i = 0$  and  $v_i = 0$  everywhere. The entropy equation (7) becomes

$$\frac{ds_i}{dr} = (\gamma_i - 1) \frac{\mathcal{L}_i}{v_i \rho_i^{\gamma_i}}, \quad (10)$$

and the conservation equations (3)–(5) now read

$$\begin{bmatrix} v_i & \rho_i & 0 \\ \sigma_i^2 & \rho_i v_i & \rho_i \\ 0 & \rho_i v_i^2 & \frac{\gamma_i}{\gamma_i - 1} \rho_i v_i \end{bmatrix} \frac{d}{dr} \begin{bmatrix} \rho_i \\ v_i \\ \sigma_i^2 \end{bmatrix} = \begin{bmatrix} \mathcal{Z}_{1i} \\ \mathcal{Z}_{2i} \\ \mathcal{Z}_{3i} \end{bmatrix}, \quad (11)$$

where the three source/sink terms are

$$\mathcal{Z}_{1i} = -\frac{2\rho_i v_i}{r}, \quad (12)$$

$$\mathcal{Z}_{2i} = \rho_i f, \quad (13)$$

$$\mathcal{Z}_{3i} = \rho_i v_i f + \mathcal{L}_i. \quad (14)$$

The component mass  $m_i$  interior to radius  $r$  is given by

$$\frac{dm_i}{dr} = 4\pi r^2 \rho_i, \quad (15)$$

and is related to the force by

$$f = -\frac{G}{r^2} \sum_i m_i. \quad (16)$$

It follows that

$$\frac{df}{dr} = -\frac{2f}{r} - 4\pi G \sum_i \rho_i. \quad (17)$$

For a system with a central point mass (e.g. a supermassive central black hole of a cD galaxy in a cluster)  $f$  rises asymptotically near the origin. For systems without a point mass (Section 2.7),  $f = 0$  at the origin.

Inversion of (11) gives

$$\frac{d\rho_i}{dr} = \frac{1}{\Delta_i} \left[ \frac{2\rho_i v_i^2}{r} + \rho_i f - \frac{(\gamma_i - 1)\mathcal{L}_i}{v_i} \right], \quad (18)$$

$$\frac{dv_i}{dr} = \frac{1}{\Delta_i} \left[ -\frac{2\gamma_i \sigma_i^2 v_i}{r} - v_i f + (\gamma_i - 1) \frac{\mathcal{L}_i}{\rho_i} \right], \quad (19)$$

$$\frac{d\sigma_i^2}{dr} = \frac{\gamma_i - 1}{\Delta_i} \left[ \frac{2v_i^2 \sigma_i^2}{r} + \sigma_i^2 f + \frac{\sigma_i^2 - v_i^2}{\rho_i v_i} \mathcal{L}_i \right], \quad (20)$$

with the sonic factor,  $\Delta_i \equiv \gamma_i \sigma_i^2 - v_i^2$ , where  $\Delta_i > 0$  corresponds to a subsonic flow. If the matrix in (11) is singular, one of the hydrodynamic variables must be eliminated algebraically to reduce the number of equations. For stationary, spherically symmetric systems, two of  $(\rho_i, v_i, \sigma_i^2, p_i, s_i)$  suffice to describe the stationary solution.

We will distinguish the mass components in the model for zero and nonzero  $\dot{m}_i$ , as the solution to above equations depends on whether or not the mass component is in a bulk inflow. In either case the mass conservation equation (9) will be used to eliminate one of the dynamical variables of each component.

### 2.3 Stagnant component, $\dot{m}_i = 0$

Usually, a static structure with zero inflow ( $\dot{m}_i = 0$ ) is forbidden (see equations 18 and 20), if there is a net energy loss ( $\mathcal{L}_i \neq 0$ ) or if the system is not isothermal ( $\gamma_i \neq 1$ ). An isothermal condition can be established if heat transport is more rapid than other radiative and dynamical processes in the system. This is not easily satisfied for the radiative gas components in a cluster. However, the situation is different for the dark matter component as dark matter neither radiates nor absorbs light. Self-interacting dark matter could behave like a fluid. Thus, such a dark halo may have a hydrostatic profile

satisfying  $\dot{m}_i = 0$ ,  $\mathcal{L}_i \equiv 0$ ,  $v_i = 0$  and  $dv_i/dr = 0$  everywhere. Moreover, its structure is completely specified by the density ( $\rho_i$ ) or temperature (velocity dispersion) ( $\sigma_i^2$ ) profiles.

The gradients of the density (18) and temperature (20) are given by

$$\frac{d\rho_i}{dr} = \frac{\rho_i f}{\gamma_i \sigma_i^2} \quad (21)$$

and

$$\frac{d\sigma_i^2}{dr} = \frac{\gamma_i - 1}{\gamma_i} f, \quad (22)$$

respectively. The latter implies that  $\sigma_i^2 = -(\gamma_i - 1)(\Phi - \Phi_R)/\gamma_i$ . In the cluster setting,  $\Phi_R$  corresponds to the dark halo surface potential.

The specific entropy is uniform in the cluster. The effectively polytropic equation of state is appropriate for dark matter if it is self-interacting, governed by Tsallis thermostatics, or has a power-law phase-space density (i.e. collisionless). In the latter case, the momentum equation is identifiable as the Jeans equation in the isotropic limit. (See Appendix C.) We note that if only one self-gravitating fluid component is present and if there is no central point mass, the object is essentially a Lane–Emden sphere (Lane 1870; Emden 1907; Chandrasekhar 1939).

#### 2.4 Flowing components, $\dot{m}_i \neq 0$

Fluids with  $\dot{m}_i \neq 0$  exhibit a central density cusp,  $\rho_i \rightarrow \infty$  as  $r \rightarrow 0$ . In order to keep the equations numerically tractable, we use (9) to eliminate  $\rho_i$ . The equation for the density gradient (18) is then redundant, leaving two relevant gradient equations:

$$\frac{dv_i}{dr} = \frac{-v_i}{\Delta_i} \left[ f + \frac{2\gamma_i \sigma_i^2}{r} - (\gamma_i - 1) \frac{4\pi r^2 \mathcal{L}_i}{\dot{m}_i} \right], \quad (23)$$

$$\frac{d\sigma_i^2}{dr} = \frac{(\gamma_i - 1)\sigma_i^2}{\Delta_i} \left[ f + \frac{2v_i^2}{r} + \left( \frac{\sigma_i^2 - v_i^2}{\sigma_i^2} \right) \frac{4\pi r^2 \mathcal{L}_i}{\dot{m}_i} \right], \quad (24)$$

and the mass profile equation:

$$\frac{dm_i}{dr} = \frac{\dot{m}}{v_i}. \quad (25)$$

Elimination of  $\rho_i$  in terms of  $v_i$  and  $r$ , particularly from the cooling function  $\mathcal{L}_i$ , clarifies the asymptotic behaviour of the differential equations, especially in the inner regions. The flow velocity  $v_i$  may take any value at the origin. Models in which  $v_i \neq 0$  at the origin describe accretion onto, or winds emerging from, a central object, presumably compact. Note that inflowing constituents have some cuspy behaviour near the origin (either  $\rho_i \rightarrow \infty$ ,  $v_i \rightarrow 0$  or  $v_i \rightarrow \infty$ ) regardless of the occurrence of radiative cooling. This causes some trouble in numerical integration. Changes of variables, including a switch of the independent variable, may, however, circumvent the problems.

#### 2.5 Composite system: radiative gas embedded in self-interacting dark matter

We consider a model cluster, which is a composite system consisting of a cooling gas component with  $\dot{m}_1 < 0$  and  $\mathcal{L}_1 < 0$  and a self-interacting dark matter component with  $\dot{m}_2 = 0$  and  $\mathcal{L}_2 = 0$ . We treat both of them as separate fluid components. We omit the stars in galaxies, as they are a minor fraction of the cluster baryons. The dominant radiative loss of the gas component is optically thin

thermal bremsstrahlung radiation. We omit line cooling, dust, conduction and Compton effects. Thus, the radiative loss is specified by a cooling function

$$\mathcal{L}_1 = -B\rho_1^2\sigma_1 = -B\rho_1^{(3+\gamma_1)/2}s_1^{1/2}, \quad (26)$$

where the normalization  $B$  depends on the gas composition (Rybicki & Lightman 1979). Cooling domination implies  $\mathcal{L}_1 < 0$  everywhere, and the specific entropy increases monotonically with  $r$ . This also ensures buoyant stability.

The inner boundary is a gas density cusp,  $\rho_1 \rightarrow \infty$ , regardless of whether radiative cooling or compressional heating dominates the gas inflow (accretion). There are two kinds of cusps: the cold cusp ( $\sigma_1 \rightarrow 0$ ) and the hot cusp ( $\sigma_1 \rightarrow \infty$ ). In cold cusps, the gas pressure  $p_1$  is finite everywhere. The specific entropy vanishes,  $s_1 \rightarrow 0$ , at the cusp. For the hot cusps, the entropy decreases smoothly towards the origin. The flow reaches the origin exactly,  $r_* = 0$ , where the speed and pressure reach infinity. For fluids with an adiabatic index of  $\gamma_i = 1 + 2/F_i$ , the asymptotes are  $\rho \propto r^{-F_i/2}$ ,  $\sigma^2 \propto r^{-1}$  and  $v \propto r^{(F_i-4)/2}$ . There may be a positive mass compact object at the origin,  $m_*$ . The flow at a hot cusp is a self-gravitating generalization of subsonic Bondi accretion (Bondi 1952).

A fully general model of multifluid self-gravitating objects permits supersonic inflows, existence of sonic points and formation of shocks. However, we focus on quiescent systems in this paper. We consider solutions in which any inflow, if present, is subsonic everywhere in the cluster.

#### 2.6 Central asymptotic behaviours

The asymptotic power-law behaviours of the variables in the central region allows us to introduce a new set of variables:

$$\beta_{\sigma_i} \equiv \sigma_i^2 r, \quad (27)$$

$$\beta_{\rho_i} \equiv \rho_i r^{F_i/2}, \quad (28)$$

$$\beta_{v_i} \equiv v_i r^{(4-F_i)/2}, \quad (29)$$

where  $i = 1$  for the gas and  $i = 2$  for the dark matter. These variables are finite at  $r = 0$ . The corresponding equation of state is given by

$$\beta_{\sigma_i} = s_i \beta_{\rho_i}^{2/F_i}. \quad (30)$$

We define a logarithmic radial coordinate  $l \equiv \ln r$ . In terms of the new variables, the gradient equations are now

$$\frac{d\beta_{v_i}}{dl} = \beta_{v_i} \left\{ \frac{4 - F_i}{2} - \frac{1}{\gamma_i \beta_{\sigma_i} (1 - \mathcal{M}^2)} \left[ 2\gamma_i \beta_{\sigma_i} - Gm + \frac{2}{F_i} \beta_L r^c \right] \right\}, \quad (31)$$

$$\frac{d\beta_{\sigma_i}}{dl} = \beta_{\sigma_i} + \frac{\gamma_i - 1}{\gamma_i (1 - \mathcal{M}^2)} \left[ 2\gamma_i \beta_{\sigma_i} \mathcal{M}^2 - Gm - (1 - \gamma_i \mathcal{M}^2) \beta_L r^c \right], \quad (32)$$

$$\frac{d\beta_{\rho_i}}{dl} = \beta_{\rho_i} \left\{ \frac{F_i}{2} + \frac{1}{\gamma_i \beta_{\sigma_i} (1 - \mathcal{M}^2)} \left[ 2\gamma_i \beta_{\sigma_i} \mathcal{M}^2 - Gm + \frac{2}{F_i} \beta_L r^c \right] \right\}, \quad (33)$$

where  $m = m_1 + m_2$ . The entropy equation is

$$\frac{ds_i}{dl} = -s_i \left\{ (\gamma_i - 1) \frac{B\beta_{\rho_i} r^c}{\beta_{v_i} \sqrt{\beta_{\sigma_i}}} \right\}. \quad (34)$$

The cooling function is

$$\beta_L = \frac{B\beta_{\rho_1} \sqrt{\beta_{\sigma_1}}}{\beta_{v_1}} \quad (35)$$

and the radial index of cooling term is

$$c \equiv \frac{7 - 2F_1}{2}. \quad (36)$$

The Mach number  $\mathcal{M}^2 = \beta_{v_1}^2 r^{F_1-3} / \gamma_1 \beta_{\sigma_1}$ , and its profile is given by the equation

$$\frac{d\mathcal{M}^2}{dl} = \frac{\mathcal{M}^2}{1 - \mathcal{M}^2} \left[ -4 \left( \frac{\mathcal{M}^2}{F_1} + 1 \right) + (\gamma_1 + 1) \frac{Gm}{\gamma_1 \beta_{\sigma_1}} - (1 + \gamma_1 \mathcal{M}^2) \frac{(\gamma_1 - 1) \beta_L r^c}{\gamma_1 \beta_{\sigma_1}} \right], \quad (37)$$

whose solution to the profile equation requires that

$$\lim_{r \rightarrow 0} \mathcal{M}^2 = \begin{cases} \infty & \text{if } F_1 < 3, \\ \mathcal{M}_*^2 > 0 & \text{if } F_1 = 3, \\ 0 & \text{if } F_1 > 3. \end{cases} \quad (38)$$

Note that the dark matter component does not have radiative cooling. This implies  $\beta_{v_2} = 0$ ,  $d\beta_{v_2}/dl = 0$  and  $ds_2/dl = 0$  throughout the system, and the dark matter structure is determined by

$$\frac{d\beta_{\sigma_2}}{dl} = \beta_{\sigma_2} - \frac{\gamma_2 - 1}{\gamma_2} Gm = \beta_{\sigma_2} - \frac{2Gm}{F_2 + 2}, \quad (39)$$

$$\frac{d\beta_{\rho_2}}{dl} = \left( \frac{F_2}{2} - \frac{Gm}{\gamma_2 \beta_{\sigma_2}} \right) \beta_{\rho_2} = \frac{F_2}{2s_2} \beta_{\rho_2}^{(F_2-2)/F_2} \frac{d\beta_{\sigma_2}}{dl}. \quad (40)$$

The mass and moment of inertia are given by

$$\frac{dm_i}{dl} = 4\pi\beta_{\rho_i} r^{(6-F_i)/2} \quad (41)$$

and

$$\frac{dI_i}{dl} = \frac{8\pi}{3} \beta_{\rho_i} r^{(10-F_i)/2}, \quad (42)$$

respectively. The mass profile would have a steep, cuspy gradient near the origin for  $F_i > 6$ . The moment of inertia shows a central cusp when  $F_i > 10$ , but this  $F_i$  corresponds to systems with infinite mass and radius, which are unphysical and are irrelevant to astrophysical galaxy clusters.

## 2.7 Numerical calculations

Some numerical difficulties could arise in solving the structure equations given in the above section when  $F_i > 6$ . To overcome these we consider another coordinate

$$a \equiv \frac{2}{6 - F_2} r^{(6-F_2)/2}, \quad (43)$$

instead of  $l$  and the transformation

$$\frac{dl}{da} = r^{(F_2-6)/2} = \frac{2}{(6 - F_2)a} \quad (44)$$

for the derivatives.

We set the boundary conditions at the surface of the dark matter component,  $R$ , and the integration proceeds inwards to the cluster centre. At the outer boundary ( $r = R$ ), we specify the total mass [ $m(R) = m_1(R) + m_2(R)$ ], the matter inflow rate ( $\dot{m}$ ), the specific entropy of dark matter (a constant  $s_2 > 0$ ), the gas temperature [ $T_R \equiv \sigma_1^2(R)$ ] and Mach number ( $\mathcal{M}_R \equiv \mathcal{M}(R)$ ). The density and temperature of the dark matter are zero at  $r = R$ . The entropy  $s_2$  is non-zero, and it defines the dark matter density and temperature gradients.

An adaptive-step Runge–Kutta scheme (Press et al. 1992) is used in the integration. We first integrate a small step radially inwards, using  $\sigma_2$  as the independent variable, to avoid numerical troubles that could be caused by the steep gradients at the cluster boundary surface. We then proceed with the main integration, using the variable  $l$  or  $a$ , approaching a reference radius chosen to be  $r = 10^{-15} U_x$ . (Here  $U_x \equiv B/G$  is the natural unit of distance; Appendix A.) We examine how the variables behave near this radius. If the gradients become too steep, we would consider alternative variables for the integration. There are two types of breakdown that may necessitate a switch. We name them as ‘cold catastrophe’ and ‘supersonic catastrophe’, and will discuss each of them in more detail.

The ‘cold catastrophe’ arises when the cooling is too efficient, causing the temperature to plummet steeply. We make use of the local monotonicity of  $s_1$  to define a new variable  $z \equiv s_1^{1/2}$  for the integration. Although there are a steep radial gradients for the variables  $\beta$ , i.e. the corresponding  $|d\beta/dl|$  diverge, the derivatives  $d\beta/dz$  are still well behaved and finite. Thus, it allows a smooth integration towards the centre, where  $z \rightarrow 0$  monotonically. Note that if the cooling catastrophe occurs at a non-zero radius – forming a zero-temperature shell – we may discard it, as it is not a viable steady solution. The cold shell lacks pressure support, and material at large radius would fall inwards until a more stable configuration emerges. Such a system would have a variety of interesting dynamic behaviours, and we will discuss it and related systems in a separate paper.

The ‘supersonic catastrophe’ arises when the gas Mach number increases towards unity at a certain radius. The  $(1 - \mathcal{M}^2)^{-1}$  factor will diverge and create numerical problems. As a resolution, we switch to  $\mathcal{M}^2$  as the independent variable when the integration proceeds and approaches the sonic horizon ( $\mathcal{M}^2 \rightarrow 1$ ). Two situations would occur. In the first one, the solution has a discontinuity, with causal disconnection between the inner and outer regions. This is the shock solution, which is interesting but does not correspond to steady galaxy clusters, the prime interest in this paper. The second one corresponds to a smooth transonic flow, in which the inflow would pass a sonic point (Bondi 1952), beyond which the accretion becomes supersonic. The steady transonic solutions are valid, but they tend to give lower gas densities than the solutions with subsonic inflows throughout the entire cluster. This also implies a greater residual central mass  $m_*$ . In this paper we seek to minimize  $m_*$  within the set of truly steady solutions, and we prefer the wholly subsonic solutions.

We consider various trial  $(\mathcal{M}_R, s_2)$  at  $R$  in the integration. In each trial we record the radius,  $r_*$  where integration stops, and the central, interior mass,  $m_*$ . For fixed  $(F_1, F_2, R, m(R), \dot{m}, T_R)$ , we map the  $(\mathcal{M}_R, s_2)$  plane and divide it into zones according to their physical and numerical characteristics (see Fig. 1). Qualitatively, we have four principal zones. Three of them are either unphysical or irrelevant to astrophysical galaxy clusters: (i) ‘too cold’ – afflicted by a cooling catastrophe at a certain radius; (ii) ‘too fast’ – containing a supersonic discontinuity; (iii) ‘levity’ – with insufficient pressure support, implying a negative central gravitating mass in

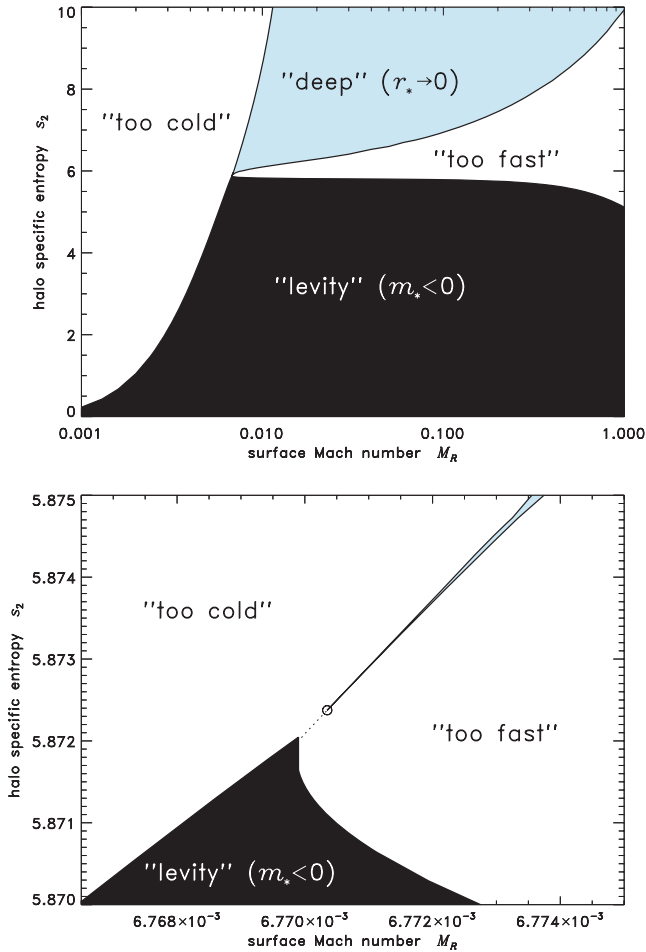


**Figure 1.** Broad and detailed maps of the key parameter domains of models with standard mass  $m(R) = 40U_m \approx 3.57 \times 10^{14} m_\odot$ , radius  $R = 4U_x \approx 0.983$  Mpc, inflow  $\dot{m} = 10 m_\odot \text{ yr}^{-1}$ , gas surface temperature 1 keV and degrees of freedom  $F_1 = F_2 = 3$ . The axes are the surface gas Mach number and the dark specific entropy. In a wedge-shaped domain (‘deep’, top panel) steady models reach from the dark surface to the origin. To the right-hand side (‘too fast’) the profile suffers a supersonic break at an intermediate radius. To the left-hand side (‘too cold’) a cooling catastrophe occurs. Models in the shaded region (‘levity’) require a negative central mass. The ‘fast’ and ‘cold’ borders intersect at a point (circled) above the  $m_* = 0$  contour. Thus  $m_*$  has a positive minimum for truly steady models.

compensation. The acceptable, physical solutions lie in the wedge-shaped region between the ‘too cold’ and ‘too fast’ zones. These solutions correspond to steady structure and subsonic flow throughout the cluster. The  $(\mathcal{M}_R, s_2)$  values where the ‘too cold’ and ‘too fast’ boundaries intersect depend on  $(F_1, F_2, R, m(R), \dot{m}, T_R)$ . The tip of this wedge region of acceptable solutions does not generally touch the contour where  $m_* = 0$ , i.e. the boundary of the ‘levity’ zone. The central mass  $m_*$  of a physical cluster must be positive and exceed some certain value. All steady, self-gravitating, spherical, cooling multicomponent clusters would require a central point mass. Strictly speaking, a spherical, cooling cluster with gas and dark matter composites without a central mass condensation is never steady. It will eventually evolve into another configuration on a dynamical time-scale. Readjustment may start with the growth of a central mass, with waves of disturbances propagating outwards like the ‘swallowing waves’ as described in Mathews & Baker (1971). In the later sections, we will present two of the mechanisms that lead

to the formation a central condensation in multicomponent galaxy clusters.

### 3 STEADY INFLOW SOLUTIONS

#### 3.1 Size, mass and compositional families

We now compare model clusters with different inflow rates ( $\dot{m}$ ), gas surface temperatures ( $T_R$ ) and dark matter degrees of freedom ( $F_2$ ) for a given total mass  $m(R)$ . We choose to fix  $m(R) = 40U_m \approx 3.56 \times 10^{14} m_\odot$ , unless otherwise specified, although the masses in the cluster solution are rescalable (see Appendix B). We fix  $F_1 = 3$  for the gas. The values of  $\dot{m}$  span the range  $1 \leq \dot{m} \leq 1000 m_\odot \text{ yr}^{-1}$ , inferred from X-ray imaging and spectral observations of cooling core clusters (e.g. Fabian et al. 1981; Nulsen et al. 1982; Stewart et al. 1984; Edge et al. 1994; White et al. 1994). For given  $(F_1, F_2, R, m, \dot{m}, T_R)$ , we minimize  $m_*$  over the  $(\mathcal{M}_R, s_2)$  plane. The contours of  $m_*$  and gas fraction ( $1/\Upsilon = m_1/m$ ) are plotted in the  $(F_2, R)$  plane (Fig. 2), with other parameters held constant.

The radius of a minimal- $m_*$  cluster increases with  $F_2$  along a  $\Upsilon$ -track. All else being equal, gas-richer tracks have larger cluster radii. Each family of solutions shows a similar variation of  $R$  with  $F_2$  when following a particular  $\Upsilon$ -track: for cosmic composition, we find that  $R(F_2 = 9) \approx 1.229 R(F_2 = 2)$ . Also,  $m_*$  decreases as  $F_2$  increases in a  $\Upsilon$ -track. However, for fixed  $F_2, m_*$  varies with  $R$ . As shown in the upper panel of Fig. 2, a peak  $m_*$  appears for  $R \approx 1.25$  Mpc, in the models with  $F_2 \approx 8$ ,  $\dot{m} = 1 m_\odot \text{ yr}^{-1}$  and  $T_R = 1$  keV.

The  $m_*$  contours behave qualitatively differently in several distinct regions of the  $(F_2, R)$  plane:

(i) For  $F_2 \gtrsim 7$ , the values of  $m_*$  drop steeply with increasing  $F_2$ . In the case of  $\dot{m} = 1 m_\odot \text{ yr}^{-1}$ ,  $m_*$  drops by a factor of  $\sim 0.1$  for each increment of 1 in  $F_2$ . The drop is steeper for larger  $\dot{m}$ . The cooling and sonic constraints permit a smaller central mass if the central density profile is steep. This occurs most easily for haloes with more degrees of freedom.

(ii) In another regime, with small radius  $R$ , both the gas fraction and the minimal  $m_*$  drop steeply with decreasing  $R$ , regardless of  $F_2$ . The poverty of gas loosens the ‘cold’ and ‘fast’ constraints, enabling smaller  $m_*$ . As  $R$  shrinks, the solution approaches that of the Lane–Emden ideal polytrope (which lacks a central mass) or else it becomes a point mass lacking both halo and gaseous envelope.

(iii) The rest of the  $(F_2, R)$  plane is a relatively featureless plateau (top left-hand region of Fig. 2):  $m_*$  increases only slightly even when there is a large increase in  $R$ . The  $\Upsilon$ -tracks, however, vary smoothly across the borders from plateau to the low- $m_*$  slopes. This insensitivity of  $\Upsilon$  occurs because the determination of bulk composition is global, whereas  $m_*$  is governed by local gas constraints acting in local bottlenecks of the inflow at small radii.

The attainable range of  $m_*$  values across the  $(F_2, R)$  map depends on the gas inflow rate,  $\dot{m}$ . Smaller  $\dot{m}$  reduces variation in  $m_*$ , with lower values on the plateau. The three panels of Fig. 2 compare families of solutions that differ only in  $\dot{m}$ . The  $m_*$  contours are completely different for different choices of  $\dot{m}$ . For  $\dot{m} = 1 m_\odot \text{ yr}^{-1}$ , the cosmic- $\Upsilon$ -track crosses  $\sim 4$  orders of magnitude in  $m_*$ . For  $\dot{m} = 10 m_\odot \text{ yr}^{-1}$ , the equivalent track crosses almost  $\sim 4.5$  orders of magnitude. For  $\dot{m} = 100 m_\odot \text{ yr}^{-1}$ , the track crosses  $\sim 5$  orders of magnitude. Note that increasing  $\dot{m}$  also shifts each  $\Upsilon$ -track to smaller radii, i.e. for a given composition, clusters with strong inflows tend to be more compact.

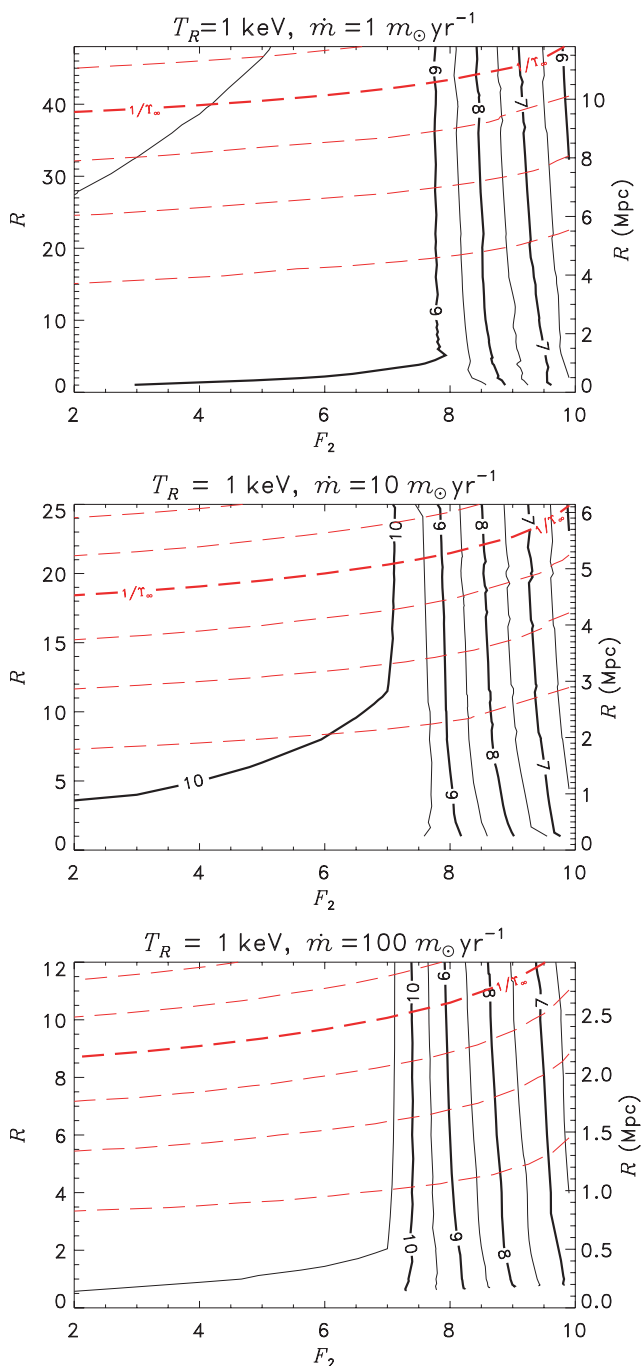


**Figure 2.** For a fixed cluster mass ( $m = 40$ ), surface temperature ( $T_R = 1$  keV) and inflow rate, we vary the outer radius  $R$  and dark degrees of freedom  $F_2$ . Black/solid contours map the minimal values of  $\log_{10}(m_*/m_\odot)$ , the central point mass. Red/dashed contours show the gas fraction,  $1/\Upsilon$  relative to the cosmic baryon fraction ( $1/4, 1/2, 3/4, 1, 5/4, \dots$ )/ $\Upsilon_\infty$ . This sequence of panels shows the effect of varying the inflow rate, with  $\dot{m} = 1, 10$  and  $100 m_\odot \text{ yr}^{-1}$  from top to bottom, respectively. For large  $\dot{m}$ , the  $\Upsilon$ -tracks occur at smaller radii, and  $m_*$  varies more widely along each track.

Increasing the gas surface temperature  $T_R$  (with everything else fixed) shifts the  $\Upsilon$ -tracks to smaller radii. However, varying  $T_R$  has negligible effect on the  $m_*$  contours. Thus the  $m_* = m_*(F_2)$  profile of a given track shifts to slightly lower masses, but this is only due to migration of the track across fixed  $m_*$ -contours. Compare the

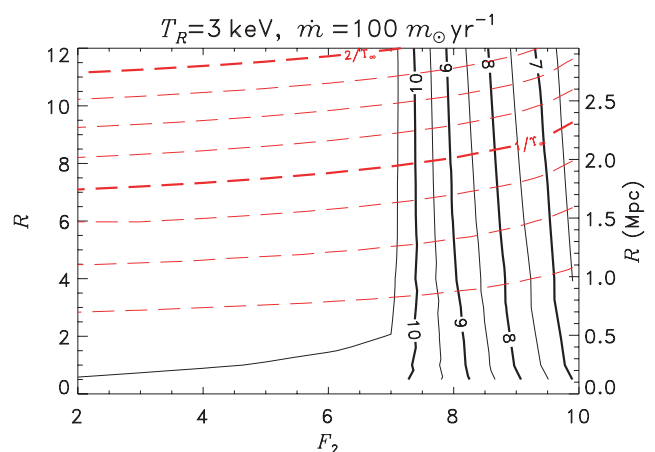


**Figure 3.** Minimal- $m_*$  and  $1/\Upsilon$  map corresponding to the bottom panel ( $100 m_\odot \text{ yr}^{-1}$ ) of Fig. 2, but for a warmer (3-keV) cluster surface. The  $m_*$  contours are almost unchanged. The tracks for given  $1/\Upsilon$  occur at smaller radii.

lower panel of Fig. 2 with Fig. 3. Thus, all else being equal, a hotter cluster is a smaller cluster but with a similar central mass.

### 3.2 External atmosphere

As  $\dot{m}$  is a constant at all radii, all stationary solutions have some tenuous gas extending indefinitely far beyond the dark halo. This atmosphere must lose its identity in the Hubble flow at some point. In this paper we take this cosmic atmosphere or accretion flow for granted. We will not consider its distribution in detail, but briefly discuss the qualitative implications of two scenarios.

We may suppose that infinite atmosphere is a continuation of the cooling, polytropic gas inflow but without a dark component. The density attenuates with distance, and bremsstrahlung cooling becomes negligible. The effects of local self-gravity dwindle. If no sonic horizon appears, then the asymptotic atmospheric structure follows some power-law decline.

Alternatively, we may choose to interpret the halo surface gas as a cosmic accretion shock (e.g. Bagchi et al. 2006). Its temperature depends on the cluster mass and radius. In practice we select  $m(R)$  and  $T_R$ . Then shock conditions constrain the plausible range of radii,

$$\frac{F_1}{(F_1 + 1)^2} \frac{Gm}{T_R} \leq R \leq \frac{F_1}{F_1 + 2} \frac{Gm}{T_R}, \quad (45)$$

with the lower and upper limits corresponding to strong and weak shock extremes, respectively. More exact constraints emerge if we consider the post-shock Mach number and pre-shock cooling. Not all families of models enable the cosmic  $\Upsilon$ -track to satisfy (45). For  $\dot{m} = 1 m_\odot \text{ yr}^{-1}$  and  $T_R = 1$  keV, the radii of  $(m_*, \Upsilon)$ -optimal solutions are too large; however, a cooler family of models with  $T_R = 0.4$  keV is satisfactory. By adjusting  $\dot{m}$  and  $T_R$  in the opposite direction, we obtain hotter and more compact cluster models that also suit a shock interpretation (e.g. Figs 3 and 4).

For very high  $T_R$  the atmosphere would extend infinitely, with pressure dropping to some asymptotic value, and temperature rising as a power law. This restricts the upper limit of  $T_R$  for physical solutions. Such phenomena also occur in the adiabatic, hydrostatic clusters (Gull & Northover 1975), where below some threshold (effectively a minimum  $T_R$ ), a gas inflow truncates at finite radius (Mathews & Bregman 1978).

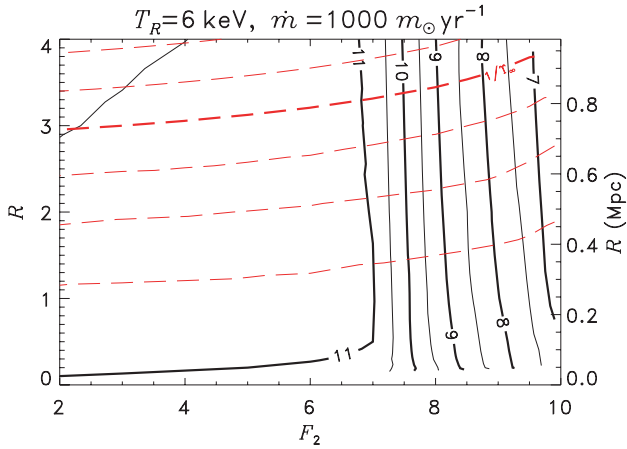


**Figure 4.** Minimal- $m_*$  and  $\Upsilon$ -track map as in Fig. 2, but with hotter gas and more inflow ( $T_R = 6$  keV,  $\dot{m} = 1000 m_\odot \text{yr}^{-1}$ ). This map includes our most compact solutions of a given  $\Upsilon$ .

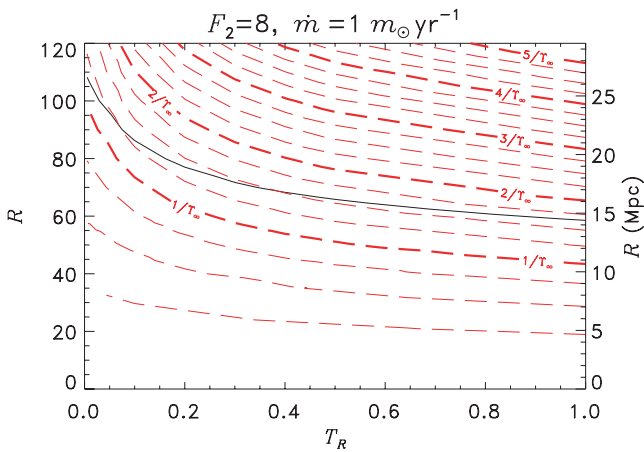


**Figure 5.** Minimal- $m_*$  and  $1/\Upsilon$  map for  $F_2 = 8$ ,  $\dot{m} = 10 m_\odot \text{yr}^{-1}$  and variable surface temperature  $T_R$ . The  $\Upsilon$ -tracks shift, but the minimal  $m_*$  hardly changes.

In our solutions, flow continuity (constant  $\dot{m}$ ) means that the subcritical gas atmospheres can break at an external sonic point ( $\mathcal{M}^2 = 1$ ) with non-zero density. It is unclear what external conditions should match on to such a supersonic break. Reducing  $T_R$  further causes the gas profile to break somewhere inside the halo,  $r < R$ . These are not numerically feasible, searchable solutions, and we avoid them. We have coarsely scanned the parameters ( $T_R$ ,  $R$ ) for fixed ( $F_2$ ,  $\dot{m}$ ) and found little qualitative variation in the inner profiles or minimal- $m_*$  values, aside from the  $\Upsilon$ -tracks shifting (see Fig. 5).

### 3.3 Radial structure of particular clusters

#### 3.3.1 General properties and density profiles

We now examine the internal structures of specific clusters in detail. Here we discuss only the minimal- $m_*$  models where the overall composition is cosmic,  $1/\Upsilon \approx 0.163$ . Table 1 lists the parameters and some global properties of these cluster solutions. In each model we chose  $F_2$  for the halo and ( $\dot{m}$ ,  $T_R$ ) for the gas, then tuned the cluster radius  $R$  to obtain cosmic composition. We tabulate signature

radii of the models defined in Section D1:  $R_{I_1}$ ,  $R_{I_2}$ ,  $R_I$  are effective core or lever radii, weighted by inertial moments of gas, the halo and both combined;  $R_w$  characterizes the concentration of gravitational potential energy;  $R_1, R_2, R_3, R_4$  are radii where the total density has a radial logarithmic slope of  $-1$ ,  $-2$ ,  $-3$  and  $-4$ ;  $R_0$  is the outermost peak of the rotation curve. Sections D2–D11 compare these signature radii to other spherical models in the literature (see Table D1 for data).

The gas + halo models differ from gasless models (Section D2) in several key respects. For  $F_2 \gtrsim 7$  the gassy clusters are gravitationally more compact:  $R_w/R$  is smaller than for corresponding gasless, non-singular polytropes. The central mass and dense cusp deepen the potential well significantly (especially when  $F_2$  is large).

The concentration of gas mass ( $R_{I_1}/R$ ) is rather insensitive to  $F_2$ . In all of our minimal- $m_*$  models, the gas is less centrally concentrated ( $0.74 \lesssim R_{I_1}/R \lesssim 0.81$ ) than in a simple  $F = 3$  polytrope ( $R_I/R \approx 0.715$ ). The presence of gas affects the halo concentration ( $R_{I_2}/R$ ), depending on  $F_2$ . For  $F_2 = 2, 3$ , the dark mass is slightly more concentrated (smaller  $R_{I_2}/R$  than for gasless spheres). For larger  $F_2$ , gas makes the halo less concentrated (larger  $R_{I_2}/R$  than for polytropes). The combined mass distribution has an effectively intermediate concentration: either  $R_{I_1} < R_I < R_{I_2}$  or  $R_{I_2} < R_I < R_{I_1}$ .

The rotation curve peaks farther out than in gasless haloes (Lane–Emden spheres) of the same  $F_2$ , and more so for large  $F_2$ . Specifically,  $R_0$  enlarges by  $\sim 1$  per cent for  $F_2 = 2$  but by  $\sim 20$  per cent for  $F_2 = 9$  cases. In all cases we find that  $R_0 > R_3$ . Importantly, this means that the rotation curve does not peak until outside a radius where the combined density slope is steeper than  $-3$ . For optimized gassy models with  $F_2 = 2, 3$  we find  $R_0 > R_4$ ; however, we find  $R_3 < R_0 < R_4$  for  $F_2 \geq 5$  generally (and for  $F_2 \geq 4$  for the compact models). In contrast, the gasless haloes have  $R_2 < R_0 < R_4$  for  $F_2 = 2, 3, 4, 5$ . For real, relaxed galaxy clusters, the comparison of measured  $R_3$  and  $R_4$  (e.g. from gravitational lensing at the outskirts) and of  $R_0$  (e.g. via member galaxy kinematics) could constrain the actual effective value of  $F_2$ , and enable extrapolation of the halo radius  $R$ .

Fig. 6 illustrates the radial structure of our baseline minimal- $m_*$  solutions with  $\dot{m} = 10 m_\odot \text{yr}^{-1}$  and  $T_R = 1$  keV, but differing in  $F_2$ . Fig. 7 depicts comparable models with a stronger gas inflow, hotter surface and smaller radius. Fig. 8 shows solutions with weak inflow, and a cool surface at large radius. The gas density profile is monotonic in radius, approximating a broken power law with the break appearing at kpc scales, and a slightly shallower slope on the outside. In the outer parts, the index of  $\approx -1$  is consistent with the simplest early models of cooling flows (e.g. Cowie & Binney 1977; Fabian & Nulsen 1977; Mathews & Bregman 1978). As expected from analysis, in the innermost regions both the gas and halo have singular density profiles approximating a Bondi accretion flow,  $\rho_i \propto r^{-F_i/2}$  for both gas and dark matter. The dark cusp is radially smaller than the gas cusp. Note that the dark cusp emerges for different reasons than the cusps of hypothetical collisionless haloes in  $N$ -body simulations. The dark cusp emerges as a self-consistent, time-independent, hydrostatic response to the central mass  $m_*$  and the gaseous mass inflow. In the latter sense it is related to an ‘adiabatic contraction’ effect (Blumenthal et al. 1986). It is not a time-dependent relic of cosmic structure formation or merger history.

The dark halo density slope varies more than that of gas. A core of approximately constant dark matter density surrounds the cusp, spanning from ten to hundreds of kpc radius. The halo outskirts are a rapid decline to zero density at the surface. As in gasless models

**Table 1.** Parameters and global properties of the minimal- $m_*$  cluster models. We fix a fiducial total mass,  $m = 40U_m \approx 3.57 \times 10^{14} m_\odot$ , and seek cosmic composition,  $1/\Upsilon \approx 0.163$ , inside  $R$ . From left- to right-hand side, the columns are: dark degrees of freedom, inflow rate ( $m_\odot \text{ yr}^{-1}$ ); surface gas temperature (keV); outer radius ( $U_s \approx 0.246$  Mpc units); gas, dark and total concentrations; gravitational radius ratio; four of the density slope radii; the peak of the rotation curve; and the minimal central mass (given in solar units and as a fraction of the cluster mass). The signature radii ( $R_{I_1}, R_{I_2}, R_I, R_w, R_1, R_2, R_3, R_4, R_o$ ) are defined in Section D1.

$F_2$	$\dot{m}$	$T_R$	$R$	$R_{I_1}/R$	$R_{I_2}/R$	$R_I/R$	$R_w/R$	$R_1/R$	$R_2/R$	$R_3/R$	$R_4/R$	$R_o/R$	$m_*/m_\odot$	$m_*/m$
2	1	0.4	46.2	0.829	0.806	0.810	0.798	0.470	0.646	0.739	0.797	0.882	6.45(9)	1.81(-5)
3	1	0.4	47.0	0.820	0.714	0.733	0.744	0.355	0.522	0.628	0.704	0.761	3.45(9)	9.68(-6)
4	1	0.4	47.8	0.812	0.625	0.659	0.686	0.272	0.417	0.525	0.612	0.637	3.35(9)	9.39(-6)
5	1	0.4	48.9	0.806	0.536	0.588	0.621	0.207	0.326	0.427	0.519	0.515	3.22(9)	9.03(-6)
6	1	0.4	50.2	0.802	0.446	0.521	0.548	0.154	0.246	0.334	0.426	0.400	3.06(9)	8.59(-6)
7	1	0.4	51.8	0.801	0.355	0.458	0.005 34	0.108	0.176	0.245	0.329	0.291	2.85(9)	8.00(-6)
8	1	0.4	53.9	0.803	0.260	0.402	1.07(-5)	0.0691	0.113	0.162	0.229	0.190	3.70(8)	1.04(-6)
9	1	0.4	56.8	0.813	0.155	0.358	0.002 33	0.0340	0.0555	0.0816	0.123	0.0950	1.27(7)	3.57(-8)
9.5	1	0.4	59.1	0.824	0.0927	0.343	0.0115	0.0174	0.0284	0.0422	0.0662	0.0490	2.66(6)	7.45(-9)
9.9	1	0.4	62.5	0.842	0.0274	0.341	0.009 80	0.003 86	0.006 31	0.009 44	0.0153	0.0109	5.71(5)	1.60(-9)
2	10	1.0	18.4	0.829	0.806	0.809	0.798	0.470	0.647	0.739	0.797	0.882	1.60(10)	4.47(-5)
3	10	1.0	18.7	0.820	0.714	0.733	0.744	0.355	0.522	0.628	0.704	0.761	1.55(10)	4.34(-5)
4	10	1.0	19.1	0.812	0.625	0.659	0.686	0.272	0.417	0.525	0.612	0.637	1.49(10)	4.19(-5)
5	10	1.0	19.5	0.806	0.536	0.588	0.621	0.207	0.326	0.427	0.519	0.515	1.43(10)	4.00(-5)
6	10	1.0	20.0	0.802	0.446	0.521	0.499	0.154	0.246	0.334	0.426	0.400	1.35(10)	3.78(-5)
7	10	1.0	20.6	0.800	0.355	0.458	2.84(-5)	0.108	0.176	0.245	0.329	0.291	1.24(10)	3.48(-5)
8	10	1.0	21.5	0.803	0.260	0.402	1.53(-5)	0.0690	0.112	0.161	0.229	0.190	5.82(8)	1.63(-6)
9	10	1.0	22.7	0.813	0.155	0.357	0.002 93	0.0340	0.0555	0.0815	0.123	0.0950	2.18(7)	6.13(-8)
9.5	10	1.0	23.6	0.824	0.0919	0.343	0.0102	0.0172	0.0281	0.0417	0.0656	0.001 86	5.22(6)	1.46(-8)
9.9	10	1.0	24.9	0.841	0.0273	0.341	0.009 86	0.003 85	0.006 29	0.009 41	0.0152	0.0109	9.02(5)	2.53(-9)
2	10 <sup>2</sup>	3.0	7.10	0.835	0.806	0.811	0.799	0.472	0.648	0.740	0.798	0.883	7.06(10)	1.98(-4)
3	10 <sup>2</sup>	3.0	7.20	0.827	0.715	0.734	0.745	0.357	0.523	0.629	0.705	0.763	6.82(10)	1.91(-4)
4	10 <sup>2</sup>	3.0	7.33	0.820	0.625	0.661	0.687	0.273	0.418	0.525	0.613	0.638	6.54(10)	1.83(-4)
5	10 <sup>2</sup>	3.0	7.48	0.814	0.536	0.590	0.623	0.208	0.326	0.427	0.520	0.516	6.22(10)	1.74(-4)
6	10 <sup>2</sup>	3.0	7.67	0.811	0.447	0.524	0.0376	0.154	0.246	0.334	0.426	0.400	5.83(10)	1.64(-4)
7	10 <sup>2</sup>	3.0	7.90	0.810	0.355	0.461	2.12(-7)	0.109	0.176	0.245	0.329	0.291	4.87(10)	1.37(-4)
8	10 <sup>2</sup>	3.0	8.19	0.813	0.260	0.405	2.12(-5)	0.0690	0.112	0.161	0.229	0.190	8.00(8)	2.24(-6)
9	10 <sup>2</sup>	3.0	8.62	0.823	0.153	0.361	0.002 87	0.0335	0.0548	0.0806	0.122	0.0937	3.35(7)	9.40(-8)
9.5	10 <sup>2</sup>	3.0	8.95	0.833	0.0908	0.346	0.0107	0.0168	0.0276	0.0410	0.0645	0.0475	8.25(6)	2.31(-8)
9.9	10 <sup>2</sup>	3.0	9.43	0.850	0.0267	0.344	0.009 70	0.003 75	0.006 12	0.009 16	0.0148	0.0106	1.48(6)	4.15(-9)
2	10 <sup>3</sup>	6.0	2.95	0.828	0.805	0.809	0.798	0.469	0.646	0.739	0.797	0.881	3.19(11)	8.96(-4)
3	10 <sup>3</sup>	6.0	2.99	0.818	0.714	0.732	0.744	0.354	0.522	0.628	0.703	0.761	3.07(11)	8.60(-4)
4	10 <sup>3</sup>	6.0	3.05	0.810	0.624	0.658	0.685	0.271	0.416	0.524	0.611	0.636	2.93(11)	8.21(-4)
5	10 <sup>3</sup>	6.0	3.12	0.804	0.535	0.587	0.616	0.206	0.325	0.426	0.519	0.514	2.77(11)	7.76(-4)
6	10 <sup>3</sup>	6.0	3.20	0.799	0.446	0.520	2.55(-4)	0.152	0.246	0.333	0.425	0.399	2.58(11)	7.25(-4)
7	10 <sup>3</sup>	6.0	3.31	0.798	0.354	0.456	1.65(-8)	0.107	0.174	0.244	0.329	0.289	8.06(10)	2.26(-4)
8	10 <sup>3</sup>	6.0	3.43	0.800	0.259	0.400	3.02(-5)	0.0685	0.112	0.161	0.229	0.189	1.12(9)	3.14(-6)
9	10 <sup>3</sup>	6.0	3.64	0.810	0.154	0.356	0.003 23	0.0334	0.0548	0.0807	0.123	0.0938	4.86(7)	1.36(-7)
9.5	10 <sup>3</sup>	6.0	3.79	0.821	0.0910	0.342	0.0112	0.0168	0.0276	0.0411	0.0648	0.0475	1.24(7)	3.47(-8)

(Section D2), haloes with fewer dark degrees of freedom exhibit a larger core. The density gradients of the dark matter in the core are flattest in the cool, puffy solutions (e.g. Fig. 8) than in the more compact cases, where the slope is appreciably nonzero (e.g. Fig. 7).

Locally, the dark matter density outweighs the gas in some but not all layers of each cluster. Constancy of  $\dot{m}$  at the dark matter surface means that  $\rho_1 > \rho_2$  in a thin surface layer. However, the halo density dominates gas throughout most of the volume, as far inwards as the core radius and deeper. This halo-dominated layer is thicker when  $F_2$  is larger: e.g. reaching in to  $r \sim 2$  kpc in the  $F_2 = 9$  model shown in Fig. 6. For modest  $F_2$  ( $\lesssim 8$ ), gas dominates the Bondi-like accretion region of the deep interior. For larger  $F_2$ , the steep dark matter density cusp dominates over gas in the innermost regions. In the  $F_2 = 9$  case shown, we have  $\rho_2 > \rho_1$  at subparsec radii near the origin, beneath a gas-rich layer several kpc thick. The layers dominated by dark matter density are smaller for the hot, compact solutions (top row, Fig. 7) than for cool, extended clusters

(Fig. 8). In principle, this might become observationally apparent in cD galaxy kinematics if the gaseous, stellar and dark components could be distinguished perfectly.

The gravitating mass at the outskirts is predominantly dark,  $m_2(r) > m_1(r)$ , which follows naturally from the assumption of cosmic baryon fraction. For models with small  $F_2$  (e.g.  $F_2 = 3$  in Fig. 6), the gas mass dominates within  $r \lesssim 100$  kpc, and the central mass  $m_*$  is the dominant component farther in (e.g.  $r \lesssim 10$  kpc in this example). Since haloes with larger  $F_2$  are more concentrated (smaller  $R_{I_2}/R$ ) the dark matter dominated part of the mass profile is thicker for greater  $F_2$  (middle and right-hand upper panels of Fig. 6). Increasing  $F_2$  shrinks the minimal  $m_*$ , so the central object becomes less dynamically significant too.

Fig. 9 shows radial variations of the logarithmic index of the total density ( $\rho_1 + \rho_2$ ) for some of the  $(m_*, \Upsilon)$ -optimal solutions. Cases with lower  $F_2$  are flatter out to larger radii, as the dark core is larger. The gas inflow tends as  $\rho_1 \propto r^{-1}$  (or steeper) near the centre,

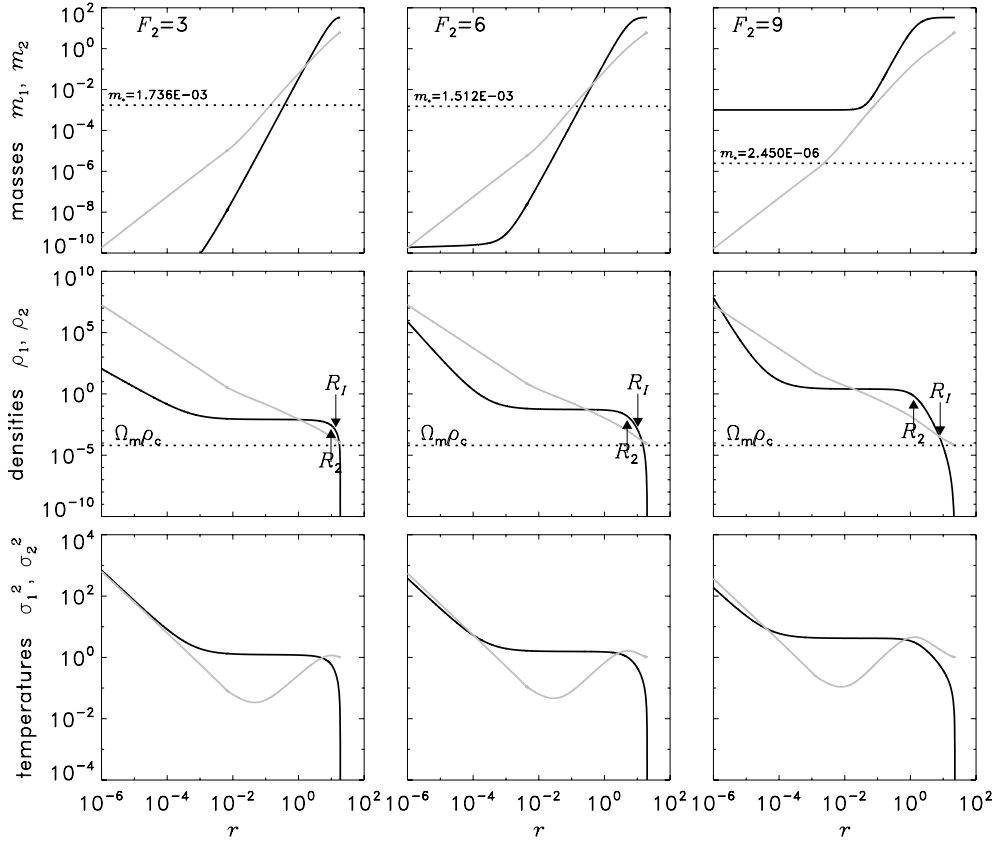


**Figure 6.** Steady inflow structure solutions for models with the same mass,  $\dot{m} = 10 m_{\odot} \text{ yr}^{-1}$ ,  $T_R = 1 \text{ keV}$  but  $F_2 = 3, 6, 9$ , in columns from left-to-right-hand side, respectively. Gas and dark matter properties are marked in grey and black, respectively. Top panels show the masses interior to radius  $r$ , with the central mass  $m_*$  marked by a dotted line. Middle panels show densities, compared to the cosmic mean density (dotted line). The inertial ‘core’ radius  $R_I$  and the slope 2 radius  $R_2$  of the total density are marked with arrows. The bottom panels are temperature profiles. The natural radial unit depends on gravity and bremsstrahlung constants,  $1U_x \equiv B/G \approx 0.246 \text{ Mpc}$ .

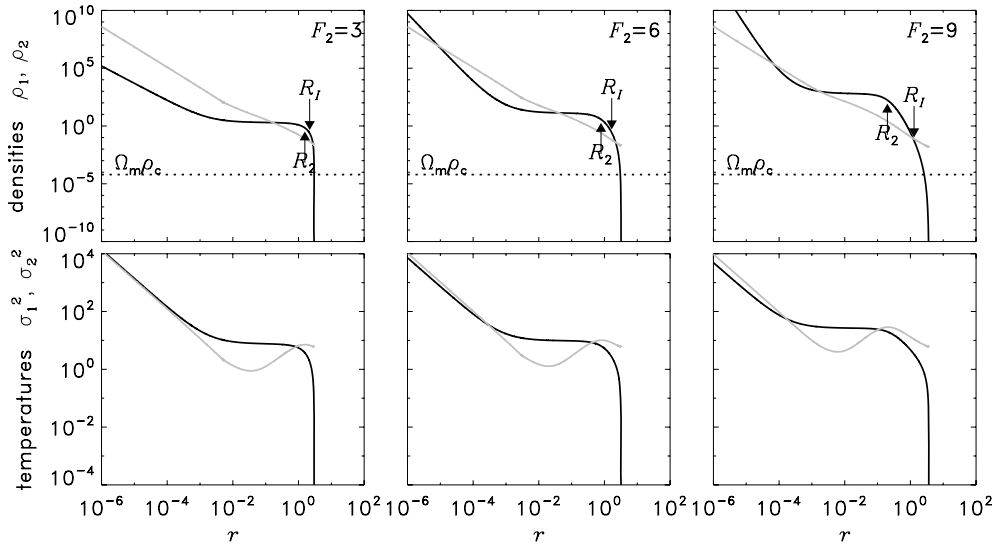


**Figure 7.** Density (top) and temperature (bottom) profiles as in Fig. 6 but with  $\dot{m} = 1000 m_{\odot} \text{ yr}^{-1}$  and  $T_R = 6 \text{ keV}$ . These are the hottest and most compact models. They have the smallest temperature ratio  $T_{\text{max}}/T_{\text{min}}$  of the  $(m_*, \Upsilon)$ -optimized models.

and this contribution prevents the overall index from reaching zero exactly, even deep within the dark core. The steepest index is  $-4$  or lower, occurring where the dark fringe drops. Gas dominates increasingly at larger radii, bringing the index up to  $\approx -1.3$  near

the halo surface. From panel to panel in Fig. 9, curves of a given  $F_2$  but different  $(\dot{m}, T_R)$  look alike except for a radial dilation. With  $\Upsilon$  implicitly fixed, the halo parameter  $F_2$  controls the proportions of the core relative to the outer surface  $R$  (see radii ratios in Table 1

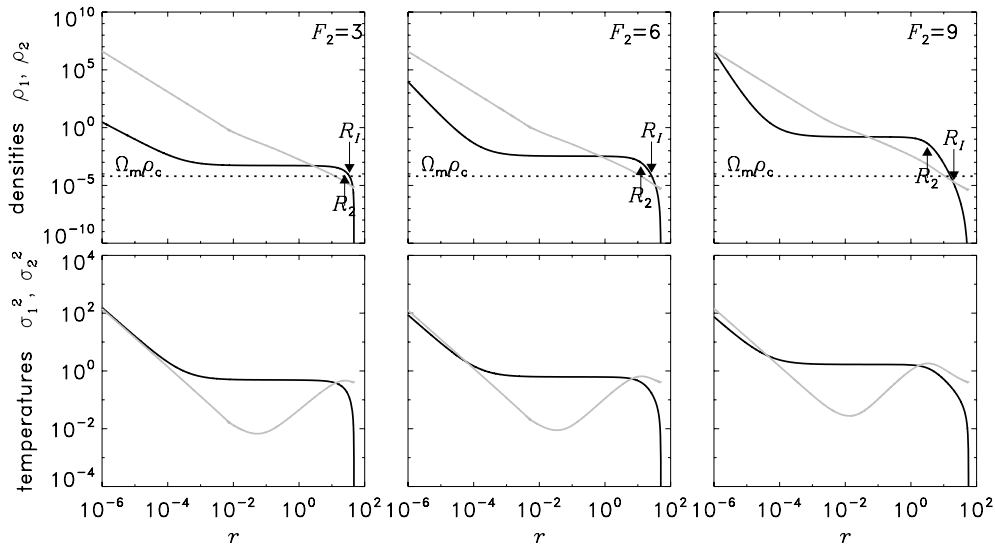


**Figure 8.** Cluster profiles as in Fig. 7 but with  $\dot{m} = 1 m_{\odot} \text{ yr}^{-1}$  and  $T_R = 0.4 \text{ keV}$ . These clusters are very radially extended, and have a large temperature variation ( $T_{\text{max}}/T_{\text{min}}$ ) in the ICM.

and Sections D1 and D2). Thus, observing a few signature radii of a real cluster could constrain its  $F_2$  and  $R$ . As a consistency check, satellites orbiting beyond  $R$  ought to exhibit Keplerian motion. We may disfavour some solutions based on their radii: the family of (1000, 6) models are smaller than 1 Mpc; while the bloated family (1, 0.4) exceed 10 Mpc (too cosmologically large).

Many X-ray, kinematic and gravitational lensing observations of clusters find total density indices dropping with  $r$  from tens of kpc outwards. X-ray analyses typically assume hydrostasis, and probe out to radii of a few hundred kpc (or  $\sim$ Mpc in rare cases). Strong gravitational lensing also constrains mass profiles out to  $10^2$  kpc radii, while weak lensing gives statistical evidence at Mpc scales. In many instances where measured indices happen to range from  $-1$  to  $-3$ , this is presented as support for NFW-like profiles (Navarro et al. 1996, see Section D7). Our reference models show similar indices at comparable radii, but with crucial differences in the core (flatter) and fringe (steeper, then the halo truncates). The present paper does not attempt to fit specific clusters, but will compare model properties to results in observational literature. Such comparisons are tentative: the commonly assumed  $\beta$ -model density law (Section D5) may overflatten the central gas, overestimating the halo density. Likewise, gravitational lens models involve subtle degeneracies (e.g. Saha, Read & Williams 2006; Liesenborgs et al. 2008, and their references) that might confuse cores with cusps.

Dipolytrope models can naturally describe those clusters observed to have soft cores. Some X-ray deprojection studies have fitted parametric halo models assuming a density cusp, and a few appear softer than cold dark matter (CDM) predictions. Katayama & Hayashida (2004) find an index  $0.47 \pm 0.31$  in the central 100 kpc of A1835. Ettori et al. (2002a) indicate  $\sim 0.6$  in A1795. Ettori, De Grandi & Molendi (2002b) prefer a modified Hubble model (Section D5) over NFW fits for 10/20 clusters, giving  $r_s$  of a few hundred kpc. Voigt & Fabian (2006) found indices  $< 1$  in 4/12 of their clusters. Zhang et al. (2006) fit a wide scatter of flattish cusp indices among 13 clusters. Combining gravitational lensing with stellar kinematics of the cD galaxy, Sand, Treu & Ellis (2002); Sand et al. (2004, 2008) find indices  $\sim 0.6$ , and  $< 1$  confidently. Rzepecki et al. (2007) finds an index  $\approx 0.7$ . These results at radii  $< 100$  kpc are consistent with the shallow regions ( $r < R_1$ ) of many

curves in Fig. 9. However, the most bloated family (upper panel,  $\dot{m} = 1 m_{\odot} \text{ yr}^{-1}$ ,  $T_R = 0.4 \text{ keV}$ ) flattens through  $R_1$  at Mpc scales (implausibly large) disavouring cases with  $F_2 \leq 9.5$ . Among the compact family (lower panel) the  $F_2 = 9.5$  and  $9.9$  curves are too steep in relevant ranges. The medium cases (middle panel) or their homologous relatives (Appendix B) are more likely representations of normal cored clusters.

Many gravitational lensing studies treat cluster cores as pseudo-isothermal spheres (PIS, Section D4), which bear comparison to dipolytrope cores. Given any empirical PIS core size  $r_s$ , we can infer  $R_2 > R_1 \approx r_s$ . Then one can extrapolate  $R$  from Table 1 ratios, and this should enclose the observable cluster. Dahle, Hannestad & Sommer-Larsen (2003) found  $r_s \approx 66$  kpc for an ensemble of clusters. Appraising that this core is too small, they rejected fluid-SIDM models of the day. However, in our calculations this core size predicts a plausible halo surface radius of  $R \gtrsim 1.9, 3.8$  or  $17$  Mpc (for  $F_2 = 9.0, 9.5$  and  $9.9$ , respectively). PIS and NFW fits by Ettori et al. (2002a) imply  $R_1 \sim 0.10$  Mpc and  $R_2 \sim 0.49$  Mpc in A1795. Diego et al. (2005) fit  $r_s \approx 15$  kpc for A1689. This is awkwardly small, favouring higher  $F_2 \approx 10$ . However, Broadhurst et al. (2005) found a core  $\sim 200$  kpc in the same cluster, and a fringe truncating around 2 Mpc (favouring  $F_2 \approx 7$ ). Halkola, Seitz & Pannella (2006) found a similar profile, but with  $r_s \approx 66$  kpc, which constrains ( $F_2, R$ ) like Dahle et al. (2003). Limousin et al. (2007) fit two halo core elements with  $r_s \approx 99$  kpc and  $66$  kpc. For RX J1347–1145, a very massive cluster, Halkola et al. (2008) find a core  $r_s \approx 117$  kpc while Bradač et al. (2008) fit  $160$  kpc. A core larger than A1689’s befits a heavier system, assuming universal values of  $F_2$  and  $R_1/R$ . Rzepecki et al. (2007) find flat cores in RCS0224–002, with  $r_s \approx 112$  kpc and  $12$  kpc. We interpret the larger measurement as the true halo core, and the smaller feature as baryon-induced contraction. Saha & Read (2008) find cuspy profiles for  $r > 25$  kpc in ACO 1703, but possibly a density shelf at  $\approx 100$  kpc. They suggest the shelf is mesostructure; we suggest an innate core with a partly contracted interior.

Simple collisionless dark matter models predict  $\rho_2 \propto r^{-3}$  asymptotically forever, whereas we predict ever steeper indices until finite truncation at Mpc scales. In future, cluster outskirts will become key observational tests of halo models. Deeper exposures from newer

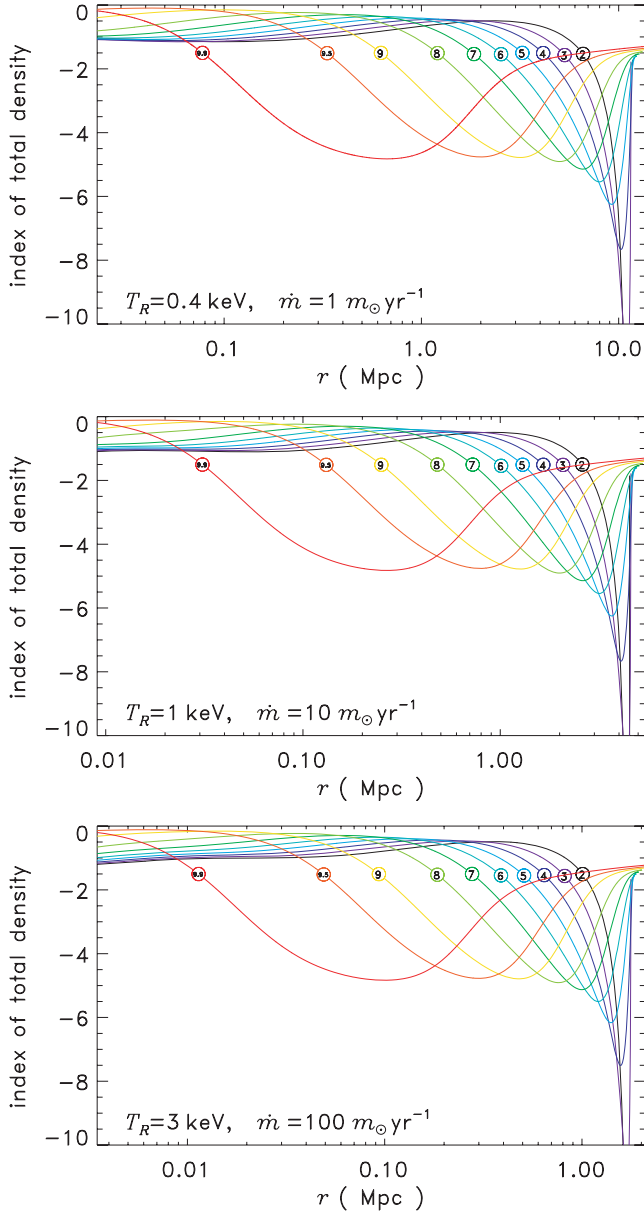


**Figure 9.** Profiles of the radial log index of the total density  $\rho_1 + \rho_2$ , for  $(m_*, \Upsilon)$ -optimal solutions with  $F_2$  values annotated. Panels from top to bottom show families  $(\dot{m}/m_\odot \text{yr}^{-1}, T_R/\text{keV}) = (1, 0.4)$ ,  $(10, 1)$  and  $(100, 3)$ , respectively.

generation X-ray observatories are needed, and more conclusive gravitational lens models would help. Already there are lensing hints of outskirts steeper than NFW (Broadhurst et al. 2005; Diego et al. 2005; Umetsu & Broadhurst 2008). An X-ray deprojection by Nevalainen et al. (1999) implies a periphery with  $\rho_2 \propto r^{-4}$ . A much wider cluster X-ray deprojection out to  $r \approx 1.7$  Mpc (George et al. 2008) shows that a hydrostatic NFW-based model cannot fit observations, because of an excess of mass or a deficit of gas pressure in the fringe. We interpret this as evidence for a finite polytropic halo.

### 3.3.2 Thermal structure

For dark matter,  $\sigma_2^2$  decreases monotonically with  $r$  (e.g. dark curves in lower panels of Figs 6–8). The temperature peaks (like  $\sigma_2^2 \propto r^{-1}$ )

in the inner density spike, then stays flat over several decades in radius, but plummets between the core and the dark surface. The upturn from core to spike occurs at what is effectively a central gravitational sphere of influence,  $r \sim Gm/\sigma_2^2$ . Note that the central point mass  $m_*$  does not yet dominate at this radius: the intervening gas and halo masses also contribute. Thus the border of the spike is essentially a sphere of *self*-influence, where the self-gravity terms become important.

The gas temperature gradient is negative in the cusp. Accretion power dominates over cooling, and the temperature profile evolves a Bondi-like slope,  $\sigma_1^2 \propto r^{-1}$ . Near the central object, the ratio of dark to gaseous temperatures approaches a constant. Taking the limit  $r \rightarrow 0$  in equations (32) and (39) gives

$$\beta_{\sigma_2^*} = \frac{2Gm_*}{F_2 + 2} \quad (46)$$

and

$$\frac{\sigma_{2*}^2}{\sigma_{1*}^2} = \frac{F_1 + 2}{F_2 + 2} \left( 1 + \frac{4 - F_1}{F_1} \mathcal{M}_*^2 \right), \quad (47)$$

explicitly involving the central mass and gas Mach number.

Outside this hot, parsec-scale accretion zone, the gas thermal structure depends upon the local balance of radiative cooling, compression and accretion power. Gas temperature gradients may be either positive or negative, depending on which terms dominate equation (20). Our optimal solutions show a local maximum temperature ( $T_{\max}$ ) at a radius typical of the dark core, and a global temperature minimum ( $T_{\min}$ ) somewhere in the kpc-scale interior. The region between these extrema, where  $dT/dr > 0$ , is one reasonable definition of the ‘cooling core’. The peak typically appears of the order of a few  $\times 0.1$  Mpc, as in X-ray observations since the earliest studies of clusters. This characteristic radial scale  $\sim U_x = B/G$  may be natural to bodies governed by gravity and bremsstrahlung radiation (see Appendix A). The temperature peak occurs at smaller radii in the compact solutions than in wide clusters (compare Figs 7 and 8). The temperature dip appears at around  $r \sim 1\text{--}10^1$  kpc, with little sensitivity to  $\dot{m}$ . The dip radius is outside both the halo density cusp and the break radius in the gas density profile.

Most of the cooling core overlaps a deep layer where dark matter is hotter than gas ( $\sigma_2^2 > \sigma_1^2$ ). This layer comprises the dark core (except the central spike). Here, any disturbance from the cluster equilibrium is likely to cause waves of adjustment that propagate faster via the halo than gas acoustic modes.

In all our solutions, the gas temperature drops off at large radii, as expected in any well bound polytrope. Cooling is ineffective at the low densities on the fringe, and at large  $r$  the velocity terms may also vanish from (24). This leaves the gravity term dominant, which guarantees  $dT/dr < 0$ . The chosen boundary values of  $T_R$  correspond roughly to bound or accretion-warmed configurations (Section 3.2). We predict that all isolated clusters have a temperature decline at sufficiently large radii. Many observations agree (e.g. Markevitch 1998; Finoguenov, Arnaud & David 2001; De Grandi & Molendi 2002; Piffaretti et al. 2005; Vikhlinin et al. 2005; Zhang et al. 2006; Pratt et al. 2007). In cases where outer temperature profile seems flat (e.g. Allen, Schmidt & Fabian 2001; Kaastra et al. 2004; Arnaud, Pointecouteau & Pratt 2005) we predict that a decline will eventually appear farther out.

The finding of  $T_{\min} \neq 0$  is a highlight of the model. There exists a non-zero floor temperature for every steady cluster. Gas does not cool indefinitely, and we have no need to invoke distributed mass dropout. It is no surprise that observed cooling cluster cores lack massive condensations of cold gas and extragalactic stars. More significantly, the existence of a temperature floor does not require

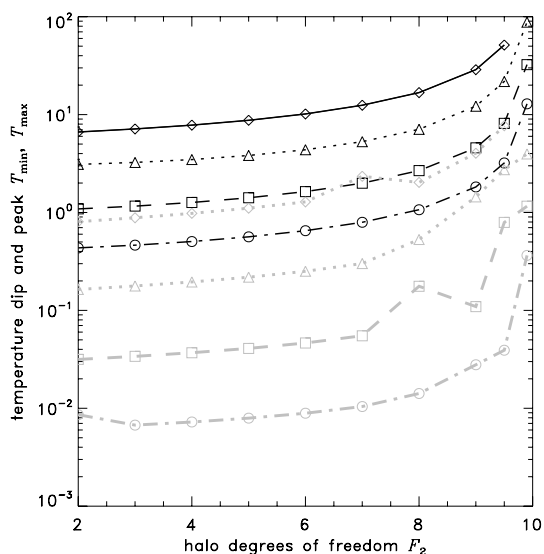


**Figure 10.**  $F_2$ -dependency of the peak and dip temperatures of the  $(m_*, \Upsilon)$ -optimal models. Black lines show the ICM fringe peak temperature. Grey/cyan lines show the inner dip temperature. The families of solutions are symbolized by:  $(T_R/\text{keV}, \dot{m}/m_\odot \text{yr}^{-1}) = (6, 1000)$  ( $\diamond$  solid);  $(3100)$  ( $\triangle$  dotted);  $(1, 10)$  ( $\square$  dashed) and  $(0.4, 1)$  ( $\circ$  dot-dashed).

non-gravitational heating. It emerges simply from the co-adaptation of gas and halo profiles in their shared gravitational potential (whether an active galaxy operates or not).

When constrained to cosmic composition and minimal  $m_*$ , both  $T_{\text{max}}$  and  $T_{\text{min}}$  increase with increasing  $F_2$  (Fig. 10). However, the ratio  $T_{\text{max}}/T_{\text{min}}$  appears less sensitive to  $F_2$  than to the other global parameters, such as  $R$ . In the moderate models (with  $\dot{m} = 10 m_\odot \text{yr}^{-1}$  and  $T_R = 1$ ) the ratio is  $10 \lesssim T_{\text{max}}/T_{\text{min}} \lesssim 41$ , and usually  $\approx 35$ . For the smaller, strong-inflow models (with  $\dot{m} = 100 m_\odot \text{yr}^{-1}$ ,  $T_R = 3$ ) we find  $8 \lesssim T_{\text{max}}/T_{\text{min}} \lesssim 22$ . For the most compact and heavily accreting model (with  $\dot{m} = 1000 m_\odot \text{yr}^{-1}$  and  $T_R = 6$ ) we find  $5.3 \lesssim T_{\text{max}}/T_{\text{min}} \lesssim 8$ . At the opposite extreme, for the radially largest, coldest series of solutions with lowest gas influx ( $1 m_\odot \text{yr}^{-1}$ ,  $T_R = 0.4$ ), we find a deep temperature contrast:  $35 \lesssim T_{\text{max}}/T_{\text{min}} \lesssim 81$ . The widest clusters provide the greatest cooling length before the inflow reaches the accretion-warmed interior. Relatively high temperature, compactness and heavy inflow yields the smallest temperature variation in the model ICM.

X-ray cluster observations reveal  $T_{\text{max}}/T_{\text{min}} \sim 3\text{--}4$ , which is softer than the temperature range of our optimal models. However, this difference is reconcilable, since  $T_{\text{max}}/T_{\text{min}}$  ratios vary across the solution space. The minimal- $m_*$  model typically has a temperature ratio near the upper extreme. Neighbouring solutions with greater  $\mathcal{M}_R$  or  $m_*$  can have a warmer thermal dip, and the soft limit of  $T_{\text{max}}/T_{\text{min}} \approx 1$  is attainable for  $m_*$  several times heavier than the minimum.

One may also ask how far the observed  $T_{\text{max}}/T_{\text{min}}$  could underestimate actual ratios due to finite radial binning and imperfect deprojection. The thermal minimum is a thin layer at small  $r$ ; and an observational annulus superimposes hotter gas from outer shells. If a shell of density  $\rho_1$  and temperature  $\sigma_1$  overlaps the annulus by area  $\delta A$  then its emission weight is  $\propto \rho_1^2 \sigma_1 (\delta A)$ . Fig. 11 shows the contributions of shells to two annuli centered on the temperature dip and peak of a cluster. For annuli of relative radial thickness  $\pm 10$  per cent, the integrated, weighted temperature ratio  $\langle T_{\text{max}} \rangle / \langle T_{\text{min}} \rangle$  shrinks

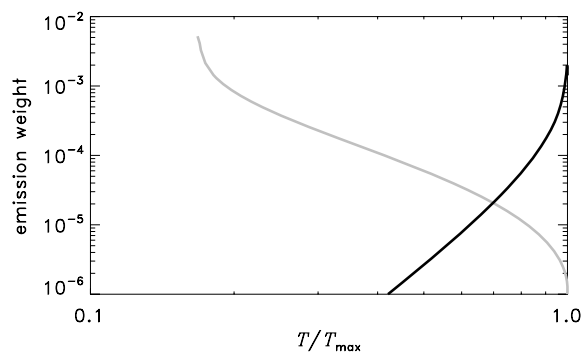


**Figure 11.** Any observational projected annulus includes gas of temperatures ( $T$ ) superimposed from a range of three-dimensional shells. We plot emission weights of gas shells crossing two mock-observational annuli: the grey curve depicts matter in an annulus around the thermal dip  $r \in [0.9, 1.1]R_{\text{min}}$ ; the black curve shows an annulus around the thermal peak  $r \in [0.9, 1.1]R_{\text{max}}$ . The model has  $m_* = 2.85 \times 10^7 m_\odot$ ,  $F_2 = 9$ ,  $T_R = 1 \text{ keV}$  and  $\dot{m} = 10 m_\odot \text{yr}^{-1}$ . Projection reduces the *apparent* peak/dip temperature ratio from  $T_{\text{max}}/T_{\text{min}} \approx 5.96\text{--}3.96$ .

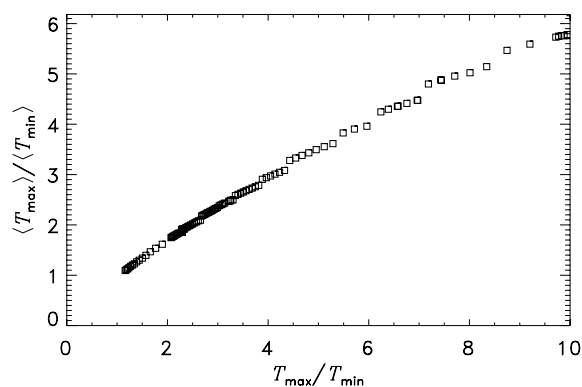


**Figure 12.** Comparison of actual ICM temperature range  $T_{\text{max}}/T_{\text{min}}$  and the projected ratios  $\langle T_{\text{max}} \rangle / \langle T_{\text{min}} \rangle$  calculated with weights as in Fig. 11, with the same  $(F_2, \dot{m}, T_R)$ . Each point is a model with non-minimal  $m_*$  near the ‘cold’ border.

by  $\lesssim 60$  per cent (see Fig. 12 for examples). Thickening the annuli makes little more difference. Projection effects cannot wholly hide the strongest thermal contrasts.

Ratios of  $T_{\text{max}}/T_{\text{min}} \sim 3$  may occur naturally if clusters have non-minimal  $m_*$  and the gas physics varies from our ideal. Raising the ICM effective heat capacity,  $F_1 > 3$  (describing microscale turbulence or a cosmic ray component) may help. Conduction and non-gravitational heating may play a role, though less influentially than popularly thought.

Bremsstrahlung radiative cooling becomes locally dynamically significant on time-scales of

$$t_c = \frac{p_1 / (\gamma_1 - 1)}{\mathcal{L}} = \frac{F_1 \sigma_1}{2B \rho_1}. \quad (48)$$

In our optimal models, the radial profile of the cooling time is approximately a power law,  $t_c \approx t_{c*} (r/r_*)^\alpha$  (see Fig. 13). The constant  $t_{c*}$  is approximately the same within families of clusters with the same  $(\Upsilon, m, \dot{m}, T_R)$  but different  $F_2$ . For minimal- $m_*$  solutions, the index is fairly consistent from kpc to Mpc scales,  $\alpha \approx 1.6\text{--}1.7$ . This is mildly steeper than X-ray evidence. For example, Voigt & Fabian (2004) and Bauer et al. (2005) deproject tens of

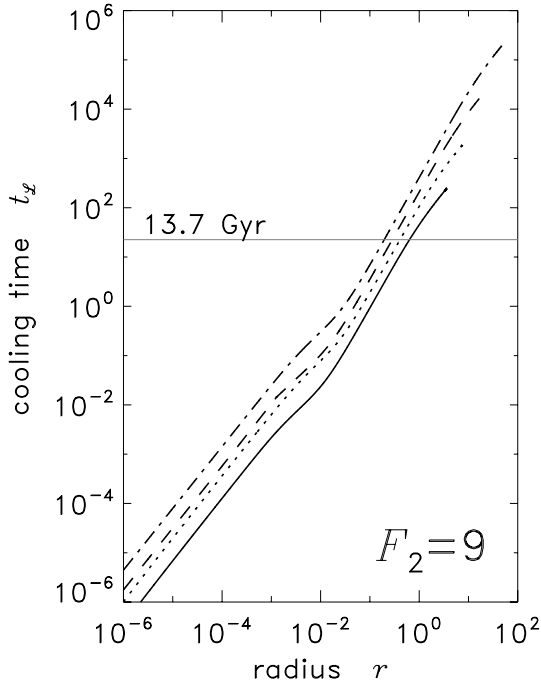


**Figure 13.** Cooling time-scale profiles of  $(m_*, \Upsilon)$ -optimal cluster solutions, for  $F_2 = 9$  haloes. Curve patterns correspond to the  $(\dot{m}, T_R)$  cases in Fig. 10. The grey horizontal line marks a time of 13.7 Gyr, assuming an ion composition factor  $\zeta = 1$ , as in Appendix A. We assume the default cluster mass scale  $m = 40U_m$ .

clusters observed out to moderate redshifts, showing  $1.3 \lesssim \alpha \lesssim 1.5$  in strata from 10 kpc to 0.5 Mpc. Their normalization also seems comparable to our standard scaling, since their curves also cross the Hubble time around  $\sim 0.1$  Mpc. This is a fair agreement, especially considering the constancy of the fiducial mass that we imposed, and the difference between their assumption of hydrostasis and the use of the full Euler equation. Improvement might be possible if we were to vary the state of the gas  $F_1 > 3$ .

Cooling is cosmologically relevant wherever  $t_c$  is shorter than the Hubble time. This occurs in some sufficiently dense inner zone of each cluster. If we define this region’s cooling radius,  $R_c$  where  $t_c < t_H$ , then we typically find that  $0.2 \lesssim R_c \lesssim 1$  (about 50–250 kpc, Fig. 14). The ‘cool core’ can reasonably be defined as the layer  $r < R_c$  rather than in terms of thermal gradients. The cool core is usually smaller than the halo core ( $R_c \lesssim R_{t_2}$ ). Along the  $(m_*, \Upsilon)$ -optimized tracks, we find that  $R_c(\Upsilon, F_2)$  shrinks with increasing  $F_2$ , despite the increase of  $R(\Upsilon, F_2)$  with  $F_2$  and the near constancy of the gas concentration ( $R_{t_1}/R$ ).

Although formally the cool core is a minor part of the cluster volume, cooling controls or affects the exterior gas structure indirectly. Contraction and subsidence of cooling gas reduces pressure support and draws in the effectively adiabatic gas farther out. (Thus the flow does not need breaking around  $R_c$ , as in Binney & Cowie 1981). In steady solutions, the core inflow matches the global rate  $\dot{m}$  of cosmic accretion from outside the halo. If the central inflow caused by cooling does not match the global inflow at the outer boundary, then a corrective acoustic wave, rarefaction wave or shock must propagate outwards into the external cosmic medium. Pedantically, it would be misleading to describe a cooling flow as driven by external pressure; the core slumps because cooling undermines local hydrostasis, and the outskirts merely follow in sinkage.

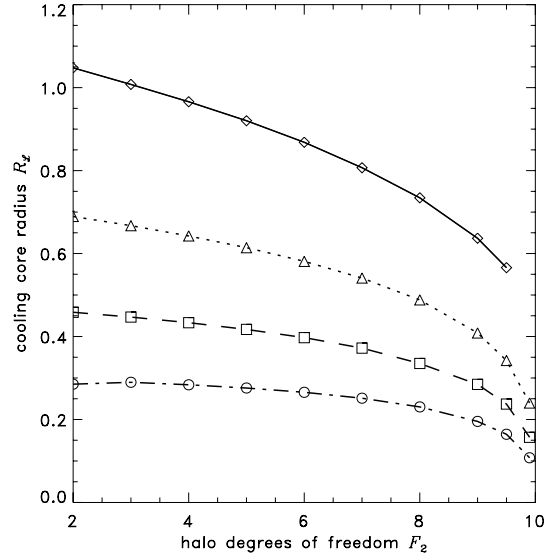


**Figure 14.** Variation with  $F_2$  of the radius  $R_c$ , within which cooling is cosmologically relevant, i.e. the cooling time matches the Hubble time. We have assumed the cluster mass  $m = 40U_m$ . The symbols represent the same families of solutions as in Fig. 10. The hot/compact, large- $\dot{m}$  clusters have the largest  $R_c$ .

### 3.3.3 Entropy profiles

The gas entropy profile is potentially an important diagnostic of the structure and history of a cluster. For a settled, convectively stable system,  $ds_1/dr > 0$  everywhere. Hot bubbles float (and cool clumps sink) whilst changing volume adiabatically, until settling at a level with comparable  $s_1$ . Spherical adiabatic accretion is expected to yield a power-law slope,  $s_1 \propto r^\alpha$ . Central non-gravitational heating may create a radially constant ‘entropy floor’ comprising an ‘isentropic core’. For gas that shocks as it accretes into a cuspy halo, theory and hydrodynamic simulations predict  $\alpha \approx 1.1$  and no flat core (Tozzi & Norman 2001; Kay 2004; Voit et al. 2005).

Our solutions show different indices in distinct layers. In the cooling core ( $10 \text{ kpc} \lesssim r \lesssim R_c$ ) we find  $\alpha \approx 1.7$ , but  $\alpha \lesssim 1$  in the effectively adiabatic outskirts. Our model lacks non-gravitational heating, so our solutions never develop a constant entropy floor. Instead, the entropy profiles soften to  $\alpha \approx 0.2$  in the hot accreting interior around/within the outermost (quasi-)sonic point ( $r \sim 10 \text{ kpc}$ ; see e.g. the bottom panel of Fig. 15). This slope persists inwards for several orders of magnitude in radius. The flatness means that cooling is less significant in the warm kpc-scale interior than in the cool-core, but there still remains a shallow stratification of  $s_1$ .

The entropy slopes in the ICM are not very different from observation, though less agreeably than the indices of the cooling time. Flat isentropic cores are not observed (Ettori et al. 2002a; Ponman, Sanderson & Finoguenov 2003; Pratt & Arnaud 2003; Piffaretti et al. 2005), though there is debate about whether the entropy normalization of smaller systems is affected by feedback heating or pre-heating. The entropy ramp appears at  $s_1 \sim 20\text{--}140 \text{ keV cm}^2$  in observed profiles (e.g. Lloyd-Davies, Ponman & Cannon 2000; David et al. 2001). It begins at  $\sim 1 \text{ keV cm}^2$  in minimal- $m_*$  models, but higher for non-minimal cases (e.g.  $10 \text{ keV cm}^2$  for that in Fig. 11). Crudely, we expect the stellar matter potential to have a raising effect similar to large  $m_*$  (work in preparation). Most authors find slopes  $\alpha \approx 1$  in the cooling core. Ettori et al. (2002a); Piffaretti et al. (2005); Pratt, Arnaud & Pointecouteau (2006); Zhang

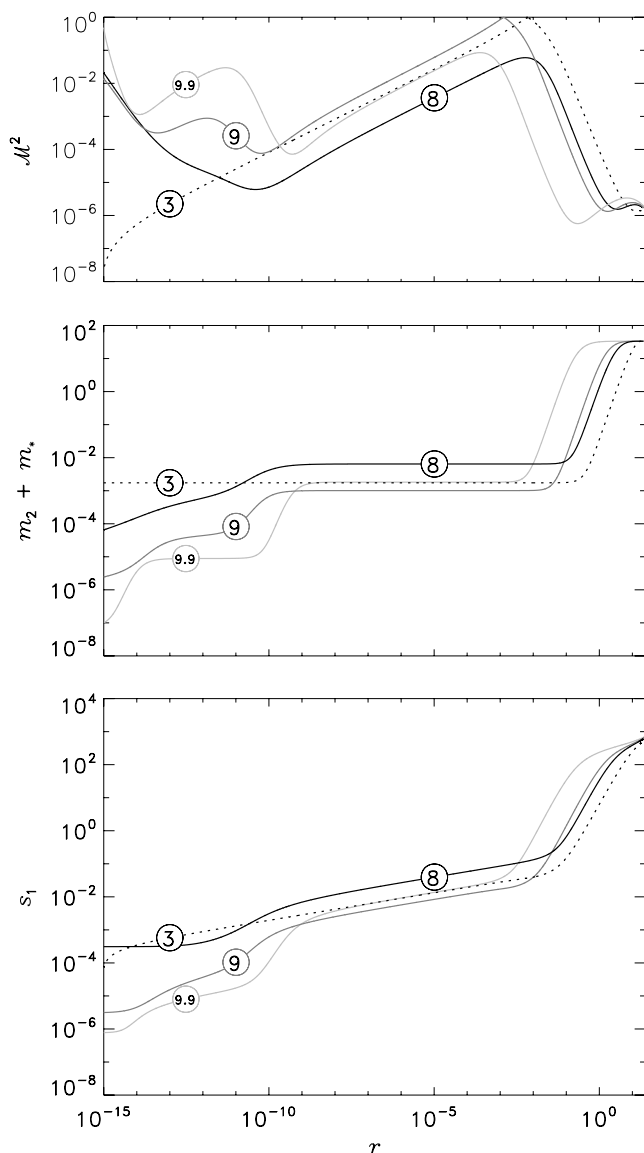


**Figure 15.** Radial profiles reaching the deep interior, for  $(m_*, \Upsilon)$ -optimal solutions where  $\dot{m} = 10 m_\odot \text{ yr}^{-1}$ ,  $T_R = 1 \text{ keV}$  and  $F_2 = 3, 8, 9, 9.9$  (annotated). Panels from top to bottom show Mach number squared, enclosed non-gaseous mass, and gas entropy.

et al. (2006) found  $\alpha \approx 0.97, \alpha \approx 0.95, \alpha \approx 1.1$  and  $\alpha = 0.99 \pm 0.06$ , respectively. Lemze et al. (2008) combined X-ray and lensing maps to model the mass of A1689, assuming spherical hydrostatics and outskirts declining as  $\rho_1, \rho_2 \propto r^{-3}$ . In the range  $10 \text{ kpc} \lesssim r \lesssim 1 \text{ Mpc}$ , they exclude any entropy floor, and found indices  $\alpha = 0.82 \pm 0.02$  when the halo was freely fitted (or  $1 \pm 0.2$  when forcing a cuspy halo model). Thus observed slopes are slightly flatter than either simulations or our solutions. This may be an artefact of the NFW-like profiles assumed in the analysis of data and construction of simulations. Alternatively, gas physics with  $F_1 > 3$  or thermal conduction might improve the match.

Several X-ray observations have seen a softer entropy slope in regions inside  $r \lesssim 20 \text{ kpc}$ , and the plots show an index  $0.1 < \alpha \lesssim 0.5$ , in agreement with the results here. Such observations are uncommon as they require fine resolution of thin annuli at small radii. Ponman et al. (2003) plot entropy profiles of 66 varied objects, and the curves

seem softer at smaller radii. Though unclear, this might be the start of an  $\alpha \lesssim 0.5$  ramp. Pratt et al. (2006) observed mild flattening at  $r < 10 \text{ kpc}$ . David et al. (2001) deproject the Hydra A cluster finely in over 30 annuli, showing  $\alpha \lesssim 0.5$  clearly across the innermost four of them. Russell, Ponman & Sanderson (2007) observed a cool-core group with no active AGN, and an entropy slope of 0.5 appears within  $r < 15 \text{ kpc}$ . When this kind of entropy break appears and attracts comment, AGN heating is conventionally invoked. The observed shallow region has been regarded as merely the outer edge of an (unseen) slope-zero isentropic interior. We argue that this slope is actually a signature of subsonic inflow inside the (quasi-)sonic point (Section 3.3.5), and not necessarily due to heating. We predict that the  $\alpha \approx 0.2$  zone persists inwards to the nucleus.

Nevertheless we caution that the inner entropy slopes may prove hard to test. Fitting a flat-cored  $\beta$ -model could potentially underestimate the central gas density, since a classic cooling flow has  $\rho_1 \propto r^{-1}$  at relevant radii. Temperature variations can hide this slope, giving an apparently flat X-ray brightness core. Underestimating gas density could lead to overestimates of the entropy, exaggerating the flatness of an observed inner  $s_1(r)$  profile.

### 3.3.4 Illusory mass deposition

Early X-ray imaging studies used approximate formulae to estimate  $\dot{m}$  from their deprojected temperature and luminosity profiles. In the notation adopted in this paper, the gradient equation for gas temperature (20) was commonly reduced to

$$\dot{m}(r) = \frac{L(< r)}{(5/2)\sigma_1^2 + \Phi(r) - \Phi(\text{inner})}, \quad (49)$$

where  $L$  is the luminosity emitted by annuli interior to  $r$ . Kinetic terms are dropped. For example, Stewart et al. (1984) plotted  $\dot{m}(r)$  dropping towards the centre. This was taken as evidence for mass dropout throughout the cooling core, and was justified in terms of runaway local thermal instability in a multiphase medium, depending on some initial spectrum of clumpiness (Nulsen 1986). Radially varying  $\dot{m}$  and multiphase gas became standard ingredients of cooling flow fits (e.g. Thomas et al. 1987; Johnstone et al. 1992) and theories (e.g. White & Sarazin 1987). However, the implied deposition products (cold gas and stars) are not observed in sufficient amounts, leading to the ‘cooling flow problem’.

When we apply formula (49) to the gas density and temperature solutions, it reproduces the true  $\dot{m}$  somewhere near  $r \lesssim R_{\mathcal{L}}$ , but at smaller radii the formula underestimates  $\dot{m}$  (Fig. 16). The fictitious radial variation of ‘ $\dot{m}$ ’ resembles observationally derived curves. Such profiles are caused by omission of velocity terms. It is a signature of proximity to the kpc-scale (quasi-)sonic point. Thus we propose to reconcile centrally depressed ‘ $\dot{m}$ ’ profiles with the dearth of massive cold condensates on cluster scales. Mass dropout from the keV-temperature cluster medium may be unnecessary, and a single-phase ICM may be plausible after all. We conclude that that gas inflows reach the central object when the system is settled, or perhaps stall at small, intragalactic radii during any episodes when the structure is driven briefly off stationarity. We discuss this further in Section 4.1.

We have also tested the effect of the hydrostatic approximation on mass profiles estimated from gas density and temperature observables. We find that the errors are negligible outside  $\gtrsim 10 \text{ kpc}$ , and the mass underestimate is only a few per cent at kpc radii.

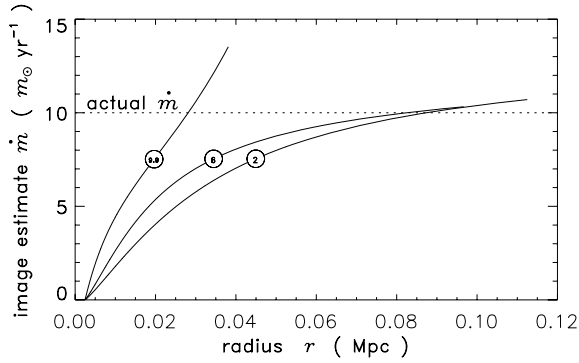


**Figure 16.** Hydrostatic imaging estimates of  $\dot{m}$  give a misleading appearance of radial variation. The true inflow rate (dotted) is constant,  $\dot{m} = 10 m_{\odot} \text{ yr}^{-1}$ . We plot cases with  $T_R = 1 \text{ keV}$ , and varied halo types:  $F_2 = 2, 6, 9.9$  (annotated). Curves are plotted up to the cooling radius  $R_{\mathcal{L}}$ .

### 3.3.5 Mach number profile and bottlenecks

The Mach number profiles of  $(m_*, \Upsilon)$ -optimal solutions show a variety of features almost anywhere from the cluster surface to the smallest calculable radii (e.g. top panel of Fig. 15). There is at least one local maximum in  $\mathcal{M}^2$ , and they are more numerous (per decade in  $r$ ) if  $F_2 \gtrsim 8$ . In many cases, the flow becomes transonic ( $\mathcal{M}^2 \rightarrow 1$ ) sharply around one of the maxima. This corresponds to the ‘sonic point’ of a maximal subsonic solution in simpler models of adiabatic, non-gravitating accretion (Bondi 1952). A slight variation of the outer boundary conditions can change a sonic point into a supersonic break. Thus these points define bottlenecks that incur the ‘too fast’ border (as in Fig. 1) thereby constraining the set of steady solutions. The radially outermost  $\mathcal{M}^2$  maximum is often (but not always) the tightest bottleneck. Throughout our survey of  $\dot{m}$  and  $T_R$  parameters, the outer bottleneck usually occurs somewhere in the radial range  $10^{-4} \lesssim r \lesssim 10^{-2}$  ( $\sim 0.25\text{--}25 \text{ kpc}$ ).

Bottlenecks in the gas entropy  $s_1$  can also occur, where small variations in outer boundary conditions can trigger a cooling catastrophe in a specific radial band. The most susceptible radial layers define the ‘too cold’ border.

The cause of bottlenecks appears in the structure of the Mach number equation (37). The cooling term  $\beta_{\mathcal{L}} r^c$  vanishes at small radii, so that the geometric and gravitational terms compete to determine the sign of  $d\mathcal{M}^2/dl$ . Approaching the origin, there is less interior mass, and in some solutions the ratio  $m/\beta_{\sigma_1}$  shrinks enough to guarantee that  $d\mathcal{M}^2/dl < 0$ . As  $\mathcal{M}^2$  increases nearer the origin, the denominators  $(1 - \mathcal{M}^2)$  shrink, which steepens the gradients of gas-related quantities. Often this leads to a runaway descent into a supersonic or cold catastrophe. In other conditions there is a narrow

escape and return to low- $\mathcal{M}$  conditions at deeper radii. Even in these ‘narrow escapes’, the behaviour in the deep interior can be dominated by ‘see-sawing’ between positive and negative terms in the ODEs. In the set of surviving solutions, the multiple ‘narrow escapes’ appear as ripples or steps on the density profile.

For larger  $F_2$ , the central mass gradients are steeper, and prone to yield low  $m/\beta_{\sigma_1}$  values, which triggers more bottlenecks and see-sawing in layers near the origin. These tend to become more numerous and restrictive as  $F_2$  increases. As the middle panel of Fig. 15 shows, when  $F_2$  is big the halo structure in the nuclear region is a concentric set of uniform cores with steep fringes. Undulations appear in the gas entropy profile as departures from the typical  $s_1$  slope, coinciding with the deep-core mass shells (bottom panel of Fig. 15).

### 3.4 Jeans stability

The outer surface of a finite single-fluid polytrope occurs at a radius comparable to the local Jeans radius,

$$r_j = \sqrt{\frac{\pi \gamma \sigma^2}{4G\rho}}. \quad (50)$$

As equilibrium structures governed by the balance of self-gravity and pressure, they are necessarily stable against gravitational collapse. Thus these bodies are Jeans masses, albeit with non-uniform interiors.

The gravitational stability of a two-component system is not as immediately obvious, with or without complications of inflow and cooling. The effective sound speeds and densities of the constituents differ at every location, and so their Jeans radii differ as well,  $r_{j1} \neq r_{j2}$ . It is possible for the dark matter to be locally Jeans-unstable while the gas is Jeans-stable, or vice versa. Fig. 17 shows the ratio of the radial coordinate to the local Jeans scale, throughout a set of reference models with cosmic composition. As expected,  $r$  approaches  $r_j$  in the fringe, for both gas and dark matter. Descending from Mpc- to pc-scale radii, each becomes more Jeans-stable. Indefinitely nearer to the origin, the gas becomes ever more stable.

However, the central, subparsec gravitational stability of the halo is more complex and contingent. For low  $F_2$ , the dark halo is Jeans-stable at all radii. In the  $F_2 = 6$  case, the halo sits at a nearly constant degree of Jeans-stability in the subparsec interior. For  $F_2 > 6$  halo stability lessens nearer the origin. For  $F_2 > 8$  the halo hovers near marginal Jeans stability for several decades in radius near the central mass. The upturn towards this condition begins at radii as large as  $10 \text{ pc}$ , and is sharper for larger  $F_2$ . In steady solutions, the ratio  $r/r_j$  within the cusp never exceeds its maximum

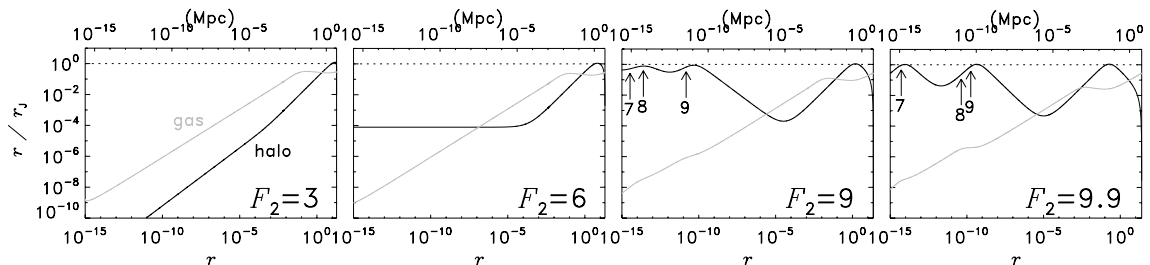


**Figure 17.** The ratio of the radius to the local Jeans radius, for  $(m_*, \Upsilon)$ -optimal solutions with  $\dot{m} = 10 m_{\odot} \text{ yr}^{-1}$ ,  $T_R = 1 \text{ keV}$  and  $F_2$  dark degrees of freedom. Halo and gas profiles are marked in black and grey, respectively. A dotted line marks the instability threshold,  $r = r_j$ . In the  $F_2 > 6$  cases the arrows mark where the marginally stable inner halo encloses a dark mass of  $10^7, 10^8, 10^9 m_{\odot}$ . A sufficiently large perturbation might make this mass collapsible.

value near the dark surface. Thus the dipolytropic cluster models are formally gravitationally stable, and we cannot infer a spontaneous collapse of the dark cusp, without the onset of other instabilities. In Section 4.1 we will discuss the possibility of externally stimulated collapse.

### 3.5 Virial scaling

Our formulation deals with the stationary, relaxed conditions to which spherical clusters tend ultimately. By construction, we omit time-dependent, externally driven evolution and our results are indifferent to cosmological history. Collisionless self-gravitating systems are expected collapse to a typical mean density that is some multiple of the cosmic critical density, implying a ‘virial mass’ within a ‘virial radius’. The model clusters in this paper are not collisionless idealizations, but their constituents may have been out of acoustic contact before assembly, which is effectively similar. Thus virial scaling may have some back-of-the-envelope relevance in observational comparisons.

Mass-wise, our solutions rescale freely, and the virial radius is not an emergent scale. In order to mimic cosmological virial scaling relations, we can rescale the mass, temperature and other profiles such that  $R_v$  matches one of the signature scales. In Table 2 we show how three choices of virial radius ( $R_v = R_3, R_v = R_l, R_v = R$ ) affect the normalization of the  $(m_*, \Upsilon)$ -optimal models. We show the mass within the virial radius, and the rescaled inflow rate. Our radially extended solutions become giant clusters. For them, the choice of  $R_v = R$  is clearly excessive. The most compact solutions rescale to the mass of a group or giant elliptical galaxy. For the compact cases with high  $F_2$ , the density profile is steep almost everywhere,  $R_3$  is small and thus the choice  $R_v = R_3$  implies a puny galaxy mass and negligible inflow. If any simple prescription for  $R_v$  applies to all the model cluster families here, then  $R_v \approx R_l$  seems like the most realistic choice.

Virial scale selection is not necessarily the best choice for linking our solutions to a cosmological scenario. We could alternatively scale each cluster so that the acoustic crossing time is some fraction of the Hubble time. However, this range of choices is too wide to explore in the present work. For the purposes of calculating X-ray spectra (in Section 3.6 below) we shall adopt the simple choice of  $R_v = R_l$ .

### 3.6 X-ray brightness profiles and continuum spectra

For photons of energy  $h\nu$ , the emission power per unit volume due to thermal bremsstrahlung is

$$j_\nu = \frac{B\rho_1^2}{\sigma_1} e^{-h\nu/\sigma_1^2}. \quad (51)$$

We project the spherical structure of each cluster solution by integrating this emissivity along sightlines to produce simulated X-ray surface brightness maps. Fig. 18 shows the brightness profiles of our baseline models in 0.1–2.4 and 2–10 keV bands. The dense central spike appears as a bright, steep spot at radial scales  $r \lesssim 10^{-2} U_x \approx 3$  kpc. This is comparable to the size of a cD galaxy, a tiny fraction of the cluster volume. The soft X-ray profile declines at all radii, but is shallower between the bright spot and  $R_2$ . The hard X-ray profile is more clearly structured: steep in the central spot; flat in some core ranging from  $1 \text{ kpc} \lesssim r \lesssim 0.1R_2$ ; and steep again in the outskirts. It is noteworthy that the apparent X-ray core is smaller than the halo core and smaller than the radius where gas temperature peaks. The X-ray core contains the radius of the temperature dip. The core is

**Table 2.** Virial masses and inflow rates for some of our  $(m_*, \Upsilon)$ -optimal solutions, under mass rescaling with three choices of virial radius:  $R_v = R_3, R_v = R_l$  and  $R_v = R$ . Masses are expressed in terms of  $\log_{10}(M_\odot)$  and inflows in terms of  $\log_{10}(M_\odot \text{ yr}^{-1})$ .

$F_2$	Standard		$R_v = R_3$		$R_v = R_l$		$R_v = R$	
	$\dot{m}$	$T_R$	$m_v$	$\dot{m}$	$m_v$	$\dot{m}$	$m_v$	$\dot{m}$
2.0	0	0.40	16.5	3.17	16.6	3.26	16.9	3.55
3.0	0	0.40	16.3	2.94	16.5	3.10	16.9	3.58
4.0	0	0.40	16.1	2.67	16.4	2.94	17.0	3.62
5.0	0	0.40	15.9	2.35	16.3	2.76	17.0	3.66
6.0	0	0.40	15.6	1.96	16.2	2.56	17.0	3.71
7.0	0	0.40	15.2	1.47	16.1	2.36	17.1	3.77
8.0	0	0.40	14.7	0.777	15.9	2.17	17.1	3.85
9.0	0	0.40	13.9	-0.400	15.8	2.03	17.2	3.96
9.5	0	0.40	13.1	-1.58	15.8	2.03	17.2	4.03
9.9	0	0.40	11.2	-4.36	15.9	2.13	17.3	4.14
2.0	1	1.0	15.3	2.37	15.4	2.46	15.7	2.76
3.0	1	1.0	15.1	2.14	15.3	2.31	15.7	2.79
4.0	1	1.0	14.9	1.87	15.2	2.14	15.8	2.82
5.0	1	1.0	14.7	1.55	15.1	1.96	15.8	2.86
6.0	1	1.0	14.4	1.16	15.0	1.76	15.8	2.92
7.0	1	1.0	14.0	0.670	14.9	1.56	15.9	2.98
8.0	1	1.0	13.5	-0.0227	14.7	1.37	15.9	3.05
9.0	1	1.0	12.7	-1.20	14.7	1.24	16.0	3.16
9.5	1	1.0	11.9	-2.40	14.6	1.23	16.0	3.24
9.9	1	1.0	10.0	-5.17	14.7	1.33	16.1	3.35
2.0	2	3.0	14.1	1.51	14.2	1.60	14.5	1.89
3.0	2	3.0	13.9	1.27	14.1	1.44	14.5	1.92
4.0	2	3.0	13.7	1.00	14.0	1.27	14.5	1.95
5.0	2	3.0	13.4	0.682	13.9	1.09	14.5	1.99
6.0	2	3.0	13.2	0.293	13.7	0.899	14.6	2.04
7.0	2	3.0	12.8	-0.206	13.6	0.698	14.6	2.10
8.0	2	3.0	12.3	-0.906	13.5	0.504	14.7	2.17
9.0	2	3.0	11.5	-2.11	13.4	0.366	14.7	2.27
9.5	2	3.0	10.6	-3.32	13.4	0.360	14.8	2.34
9.9	2	3.0	8.74	-6.12	13.5	0.449	14.8	2.45
2.0	3	6.0	12.9	0.790	13.1	0.878	13.3	1.17
3.0	3	6.0	12.7	0.553	12.9	0.720	13.4	1.20
4.0	3	6.0	12.5	0.285	12.8	0.554	13.4	1.24
5.0	3	6.0	12.3	-0.0312	12.7	0.375	13.4	1.29
6.0	3	6.0	12.0	-0.419	12.6	0.181	13.4	1.34
7.0	3	6.0	11.6	-0.918	12.5	-0.0231	13.5	1.40
8.0	3	6.0	11.2	-1.61	12.3	-0.221	13.5	1.47
9.0	3	6.0	10.3	-2.79	12.3	-0.346	13.6	1.58
9.5	3	6.0	9.50	-4.00	12.3	-0.348	13.7	1.66

smaller when  $F_2$  is larger (and seems almost to vanish in the  $F_2 = 9.9$  solutions).

Observed X-ray brightness profiles of galaxy clusters are empirically fitted with a ‘ $\beta$ -model’ atmosphere within a presumed isothermal distribution of dark matter or galaxies (Cavaliere & Fusco-Femiano 1976, see Section D5). In such fits, the surface brightness varies with projected radius  $b$  according to

$$S(b) = S_0 [1 + (b/b_c)^2]^{-3\beta+1/2}. \quad (52)$$

The index  $\beta$  fits the outer slope, while the parameter  $b_c$  measures the core radius. The observed range is  $0.4 \lesssim \beta \lesssim 1.4$  and typically  $0.1 \text{ Mpc} \lesssim b_c \lesssim 0.5 \text{ Mpc}$  (e.g. Jones & Forman 1984; Ettori & Fabian 1999; Mohr, Mathiesen & Evvard 1999; Neumann & Arnaud 1999). Variant models exist to fit more centrally peaked clusters, by combining cusps and/or  $\beta$  components of different sizes (Xu et al. 1998; Pratt & Arnaud 2002). The  $\beta$ -model was originally derived

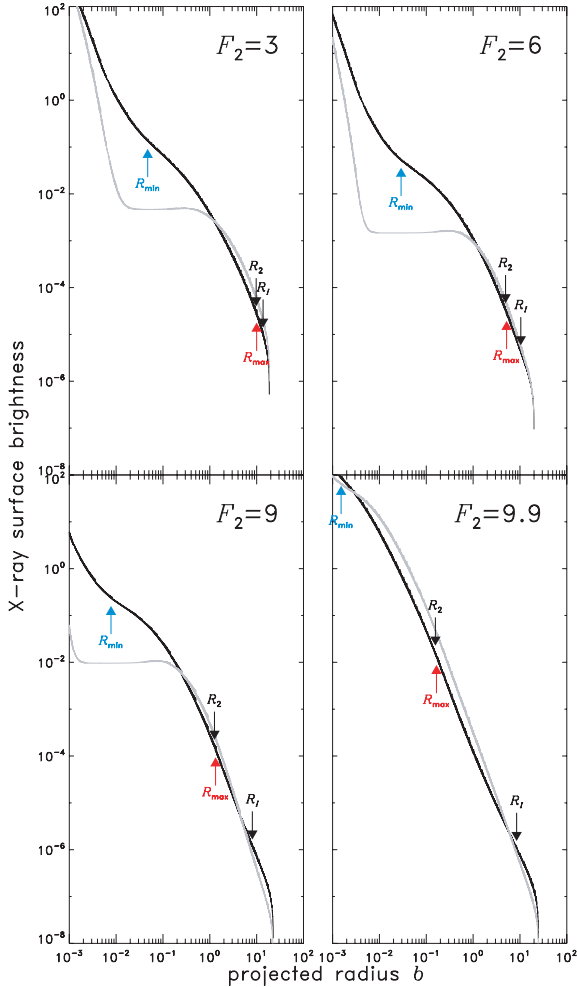


**Figure 18.** Brightness profiles of X-ray continuum projected from  $(m_*, \Upsilon)$ -optimal solutions with  $\dot{m} = 10 m_\odot \text{ yr}^{-1}$  and  $T_R = 1 \text{ keV}$ , but various  $F_2$ . Black lines show 0.1–2.4 keV emission; grey shows the 2–10 keV band. We have rescaled the mass and temperature to a virial selection of  $R_v = R_I$ . The X-ray core is smaller than the halo core, and both shrink as  $F_2$  rises.

for isothermal atmospheres, but it is still applied to clusters that are now known to have radial temperature variations.

Excepting the central spike, the  $\beta$ -model resembles the synthetic X-ray profiles presented here. In the  $\dot{m} = 10 m_\odot \text{ yr}^{-1}$  series, we find core sizes  $b_c \lesssim 0.3 \text{ Mpc}$ , shrinking slightly with rising  $F_2$ . However, the  $(m_*, \Upsilon)$ -optimal model for  $F_2 = 9.9$  forms no X-ray core at all, which is empirically unfavourable. The fringe brightness declines with similar slopes in all bands:  $\beta \approx 1.0 \pm 0.2$  around  $R_2 \lesssim r \lesssim R_I$ . These results sit within the observed range.

We note that  $\beta$ -like profiles are not a distinguishing feature of our formulation, nor cored haloes as a class. Even in the entirely cuspy profiles predicted for collisionless dark matter, the gas settles as a cored atmosphere, with shallow central gradients, fitting some kind of  $\beta$ -model (Navarro, Frenk & White 1996; Eke, Navarro & Frenk 1998). Makino et al. (1998) have shown that  $\beta$ -like profiles are broadly natural to isothermal hydrostatic clusters, though cuspy haloes yield smaller  $b_c$ .

Like the projected light distributions, the three-dimensional luminosity profile  $L = L(r)$  has a flat core, a declining fringe and a bright nuclear spot. The central X-ray spike fits inside radii  $r \lesssim 10^{-2}$ , so we choose this as a cut-off defining the luminosity of the ICM. At stan-

dard scaling,  $m(R) = 40U_m$ , the ICM luminosity increases with  $\dot{m}$  and with  $F_2$ . We find  $L_{\text{icm}} \gtrsim 2 \times 10^{41} \text{ erg s}^{-1}$  in the wide/cool family of clusters ( $\dot{m} = 1 m_\odot \text{ yr}^{-1}$ ,  $T_R = 0.4 \text{ keV}$ ). For the medium-sized solutions ( $\dot{m} = 10 m_\odot \text{ yr}^{-1}$ ,  $T_R = 1 \text{ keV}$ ), we find  $L_{\text{icm}} \gtrsim 5 \times 10^{42} \text{ erg s}^{-1}$ . In the more compact solutions we have  $L_{\text{icm}} \gtrsim 1.4 \times 10^{44} \text{ erg s}^{-1}$  (for  $\dot{m} = 100 m_\odot \text{ yr}^{-1}$ ,  $T_R = 3 \text{ keV}$ ); and  $L_{\text{icm}} \gtrsim 2 \times 10^{45} \text{ erg s}^{-1}$  for the most compact set ( $\dot{m} = 1000 m_\odot \text{ yr}^{-1}$ ,  $T_R = 6 \text{ keV}$ ).

The nuclear spot is more luminous, but this depends on where we truncate the model. If we had undertaken a relativistic formulation (Section 4.2.6), then structures at the classical inner radius  $r_* = 0$  would shift out to an event horizon at  $r_* = 2Gm_*/c^2$ . If we truncate  $L(r)$  at  $r \sim 5r_*$  (suiting accretion on to a black hole) then we find typical nuclear luminosities around  $L_* \approx 5 \times 10^{44} (\dot{m}/1 m_\odot \text{ yr}^{-1}) \text{ erg s}^{-1}$ , which is plausible as the total accretion power of an AGN. Realistically, we would expect a large share of this power to emerge in forms other than observable bremsstrahlung radiation. Extra physics and subparsec AGN anatomy may reduce the emergent luminosity to a small fraction of the accretion power (see Sections 4.1–4.2.7). In particular, Compton scattering and dense obscuring interstellar media must alter or reprocess the escaping radiation. Thus, the central density and accretion power in the present, undetailed model may be consistent with radiatively inefficient black hole feeding or with AGN, which is not such a dire outcome as early reviews assumed. (Indeed the bright spot is *hot* and therefore qualitatively different from the *cold catastrophe* accumulations that early works predicted.)

All of the ICM and nuclear luminosities given above have assumed the standard normalization, with total cluster mass  $m(R) = 40U_m \approx 3.57 \times 10^{14} m_\odot$ . If we rescale the masses by a factor  $X$  then the luminosity changes by a factor  $X^{5/2}$  (see Appendix B). For instance, if we lighten the compact, Mpc-scale,  $\dot{m} = 1000 m_\odot \text{ yr}^{-1}$  solutions by a factor  $X = 0.01$  to represent an isolated giant elliptical protogalaxy, then the inflow shrinks to  $\dot{m} = 1 m_\odot \text{ yr}^{-1}$ , with nuclear luminosity  $L_* \approx 5 \times 10^{42} \text{ erg s}^{-1}$  and ICM luminosity  $L_{\text{icm}} \approx 2 \times 10^{40} - 2 \times 10^{41} \text{ erg s}^{-1}$ . The central mass limit rescales as well: the central black hole must weigh at least  $1.2 \times 10^5 m_\odot \lesssim m_* \lesssim 3 \times 10^9 m_\odot$  (depending on  $F_2$ ).

Luminosity and mean ICM temperature correlate in our basic models,  $L_{\text{icm}} \propto T_x^\alpha$  (see Fig. 19). For raw models set via inflow condition (45), the slope is  $\alpha = 3.46$ , which is steeper than observed ( $\sim 2.6$ – $3.0$ , e.g. Markevitch 1998; Arnaud & Evrard 1999; Novicki, Sornig & Henry 2002; Ikebe et al. 2002; Lumb et al. 2004). Clusters rescaled to virial density (Section 3.5) show  $\alpha = 2.22, 2.02$  and  $2.05$  (for  $R_v = R_3, R_I, R$ , respectively) resembling the  $\alpha = 2$  prediction from gravitational collapse theory (Kaiser 1986). Nature’s way of breaking the mass homology seems intermediate: the cause may involve the boundary condition, heating (Ponman, Cannon & Navarro 1999; Loewenstein 2000) or other aspects of gas physics (Section 4.2).

We have calculated synthetic X-ray spectra at several projected radii in the bloated, medium and small cluster solutions (see Fig. 20). As with the projected brightness profiles, each of these plots assumes the virial mass scaling  $R_v = R_I$ . This makes the large clusters hotter and more massive than under the original normalization [ $m(R) = 40U_m$ ] becoming a massive supercluster with temperatures of tens of keV around the virial radius, which is several Mpc. This rescaling does not resemble any known realistic object; the choice of  $R_v = R_I$  appears unsuited to this family of solutions. Clusters of medium radius (middle row) show temperatures of several keV near the virial radius, which is near or outside the temperature peak. At

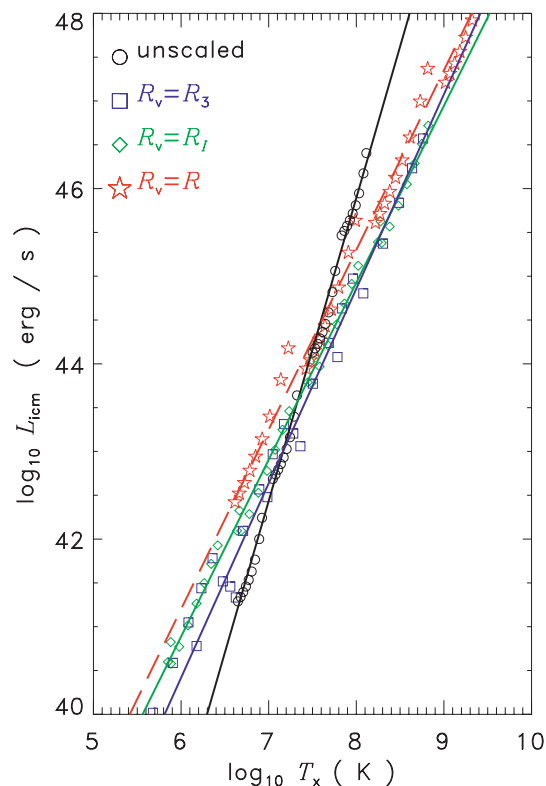


**Figure 19.** Luminosity/temperature relation of model clusters. The mean temperature derives from the total mass and internal energy of gas [ $kT_x = (2/3) U_1/m_1$ ] in the ICM ( $r > 0.01U_x$ ). Circle data are the models from Table 1. Squares, diamonds and stars are rescaled to ‘virial’ density according to the rules in Table 2.

the projected radius of the temperature dip, the continuum curves in a clearly multitemperated way.

The results are similar for the smaller clusters (bottom row) but the peak temperature is  $\approx 1$  keV and the continua are more obviously curved in the 0.1–10 keV band that we display. However, line cooling is significant compared to bremsstrahlung in low-mass systems such as these, which may alter the profiles appreciably (Section 4.2.1). Further calculations are needed, with a more detailed cooling function, to model galaxy/group spectra including line and edge features. However, line cooling would break the homology of the present solutions (Appendix B), requiring a more expensive exploration of parameter space. We defer this topic for future investigation.

### 3.7 Projected mass and gravitational lensing profiles

To help predict and assess the gravitational lensing signatures of our cluster models, we calculate mass maps by integrating  $\rho_1 + \rho_2$  along lines of sight at various projected radii  $b$ . Fig. 21 presents the projected profiles of total mass column density,  $\Sigma = \Sigma(b)$ , for several representative ( $m_*$ ,  $\Upsilon$ )-optimized models. The radial gradients are steep on scales from several hundreds of kpc to several Mpc (beyond the effective core radius  $R_f$ ). The distribution flattens on scales between tens to hundreds of kpc. (This is the mass core.) In the deepest inner regions, within tens of parsecs of the origin, the central spike dominates and the flat core steepens again. The border between core and spike typically occurs around  $10^{-4}$  to  $10^{-3} U_x$ , regardless of whether the cluster is cool/bloated, moderate or

hot/compact. The radius of the projected mass spike is comparable to, or smaller than, the radius where the X-ray brightness spike begins. The spike in  $\Sigma$  exists in theory but may be unobservable in practice: dominated by the stellar mass of a cD galaxy.

As was apparent in three-dimensional density profiles, the projected  $\Sigma$  core is smaller and denser when  $F_2$  is greater. The outer radius  $R$  varies more slowly with  $F_2$ , so the mean slope of the outskirts is shallower if  $F_2$  is high. The spike profile depends on  $F_2$  also: for  $F_2 < 6$  the gas density dominates at  $\sim 10$  pc scales, and the profile has a logarithmic slope of  $\sim -1$ . For  $F_2 \geq 6$  the spike is more often dominated by dark mass, and  $\Sigma$  shows a slope steeper than  $-1$ . These predominantly dark spikes are more prevalent and more radially extended in the compact/hot cluster models. In the coolest, most diffuse models (top left-hand panel of Fig. 21) all the spikes are gas-dominated down to  $10^{-6} U_x$ .

We predict that gravitational lensing measurements that probe images on Mpc scales will see steep mass slopes of the halo fringe. Medium-separation lensing systems (probing just within the core radius) may reveal shallower gradients of the dark core. However,  $\Sigma$  indices are unlikely to reach zero in the core, due to the  $\rho_1 \propto r^{-1}$  gas contribution, and the projection of outer layers. If the innermost regions can ever be discerned through the light of the cD galaxy then they may appear spiky.

## 4 DISCUSSION

### 4.1 Implications in galaxy evolution

As we report in Section 3.3.5, the bottlenecks that select the valid stationary solutions occur on two different radial scales. The outer critical region occurs at kpc radii. It may not be a coincidence that this is the characteristic extent of the stellar matter in an elliptical galaxy. If a primitive, initially starless protocluster or protogroup were perturbed from a stationary state, then the cooling catastrophe will tend to emerge within  $\lesssim 3$  kpc from the centre. Nulsen et al. (1984) and Fabian, Nulsen & Canizares (1984a) anticipated this size from back-of-the-envelope arguments; our radially complete calculations substantiate it. During a strong enough disturbance, excess cold gas may drop out as star formation, until a new stationary configuration settles. In short, bumping or shaking a protogalactic globule may spawn a spheroidal galaxy monolithically. However, the bottleneck radii limit the extent of stellar condensation, influencing the high-mass cut-off of galaxies (perhaps alongside AGN or conduction effects, e.g. Silk & Rees 1998; Begelman & Nath 2005; Silk 2005; Best et al. 2006; Fabian, Voigt & Morris 2002).

The inner critical regions occur on subparsec scales, comparable to the sizes of galactic nuclei. Here again, transient disturbances towards overcooling might form a local concentrations of stars. However, in high- $F_2$  cases, the inner halo sits on the brink of Jeans instability (Section 3.4), and the upturn towards this threshold begins as far out as  $\sim 10$  pc. In these conditions, a non-linear perturbation may trigger collective gravitational collapse by the dark matter (until a new stationary solution emerges). SMBHs may be the natural product. The spikes of high- $F_2$  haloes may collapse themselves into holes whenever anything rattles the central galaxy appreciably. The collapsible spike mass is comparable to real SMBH masses.

Earlier works have proposed mechanisms for black holes to feed and grow from self-interacting dark matter, evading Eddington limits and emitting little directly luminous evidence (Soltan 1982). Ostriker (2000) and Hennawi & Ostriker (2002) considered dark Bondi accretion on to stellar black hole seeds, followed by slower,

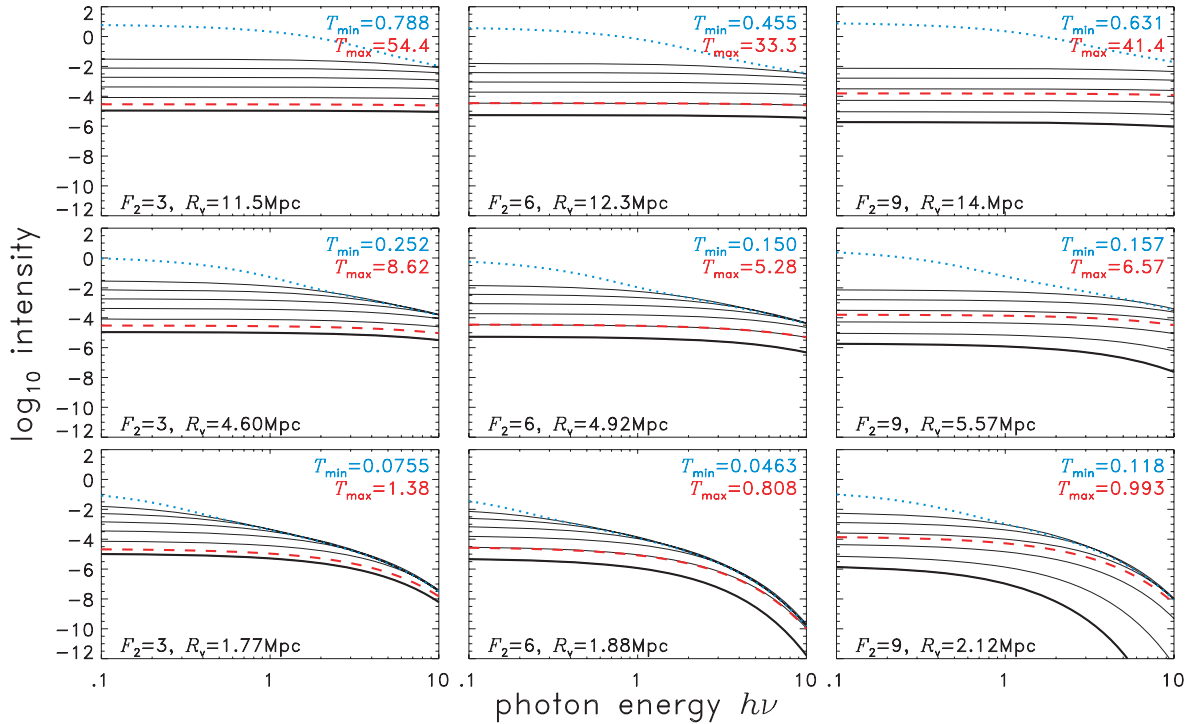


**Figure 20.** Projected X-ray spectra (continuum only) from the models with fiducial parameters  $(\dot{m}/m_{\odot} \text{ yr}^{-1}, T_R/\text{keV}) = (1, 0.4), (10, 1)$  and  $(100, 3)$  (from top to bottom rows, respectively). Here, however, the masses and temperatures are rescaled to virial conditions, choosing  $R_v = R_l$ , as in Table 2. The halo freedom is  $F_2 = 3, 6, 9$  in the left-hand, middle and right-hand columns. In each panel, the blue (dotted) spectrum reaches the temperature dip radius; red (dashed) reaches the temperature peak; and the black spectra are projected at fractions of the virial radius,  $b = \{1/32, 1/16, 1/8, 1/4, 1/2, 1\} R_v$ . The bold curve is at  $b = R_v$ . Rescaled values of the peak and dip temperatures (keV) are noted in the top right-hand corner of each panel.

diffusive loss-cone refilling. Their feeding scenario requires SIDM interactions to be weak enough to provide an initial NFW-like cusp. Munyaneza & Biermann (2005) show that an SMBH can grow at an asymptotic (exceeding exponential) rate if the dark halo has a degenerate fermion core. Balberg & Shapiro (2002) found that gravothermal collapse in conductive, weakly SIDM can spawn  $10^6 m_{\odot}$  black holes directly (and these require gas accretion to reach  $10^9 m_{\odot}$ ). Like the latter mechanism, our scenario requires no seed, and its preconditions are self-organized by the gas/halo interplay. Like the fermion-feeding model, we are free to consider interactivity at a strength that precludes NFW cuspieness in any epoch. The mechanism is a differentiated Jeans collapse: when stimulated, the hole feeds from a single dark gulp, and this intake is only limited by the mass of the dark spike.

Stationarity of the whole cluster demands the development of a central mass. Note however that the  $m_*$  limits express only the *minimal* object. This lower limit does not predict the correlation between SMBHs and stellar bulge properties. Such relations probably involve extra regulatory processes operating on galaxy scales. The depth of the galaxy potential and the kick velocities of black hole mergers may influence the upper limits (e.g. Haiman 2004; Madau & Quataert 2004; Bogdanović, Reynolds & Miller 2007; Campanelli et al. 2007a,b; González et al. 2007; Schnittman & Buonanno 2007; Volonteri 2007). In our scenario, massive black holes can form rapidly and darkly. If a merging galaxy is apt to expel its SMBH then we would expect a replacement to condense when the scene settles to a resurgent gas inflow and dark spike.

During the tranquil periods between mergers, there are two plausible fates for the gas inflow after it penetrates below kpc radii.

It may suffer cold catastrophe (if the configuration is near the critical border) depositing cold gas and new stars centrally. This essentially shrinks the ‘cooling flow problem’ down to parsec scales, which is arguably an improvement over the old 0.1-Mpc sized problem. More likely, the inflow feeds the central black hole directly.

The existence of powerful quasars in the era  $z > 6$  (Barth et al. 2003; Walter et al. 2003; Willott, McLure & Jarvis 2003) requires that black holes grew rapidly. Our model not only allows this, but *requires* it to happen before a galaxy or cluster achieves stationarity. Whether large  $\dot{m}$  inflows are sustainable into the modern era is another matter. The accumulated stellar mass distribution may eventually alter the central potential enough to change the allowed domain of steady feeding solutions (Section 4.2.4). If high  $\dot{m}$  inflows can persist, the implied AGN activity needs explaining. Much of the time, an AGN may accrete in a radiatively inefficient mode: many complicating factors could reduce the settled AGN luminosities to a small fraction of the actual accretion power. Opacity (Section 4.2.6) and thermal conduction (Section 4.2.2) may smudge or dim the nuclear bright spot. An opaque, super-Eddington inflow entrains and swallows much of its own luminosity (Begelman 1978, 1979). The non-luminous power of jets and bulk outflows from subparsec regions may hide much of the accretion power (e.g. Di Matteo et al. 2003; Allen et al. 2006).

If cD galaxies form from massive cooling inflows, then they may differ qualitatively from elliptical galaxies in the field. We expect an association between cooling cores and the presence of a cD galaxy. A cluster merger might displace an old cD galaxy, and temporarily disrupt the cooling core. A new cD galaxy would eventually sprout in the middle of the resuming cooling flow.

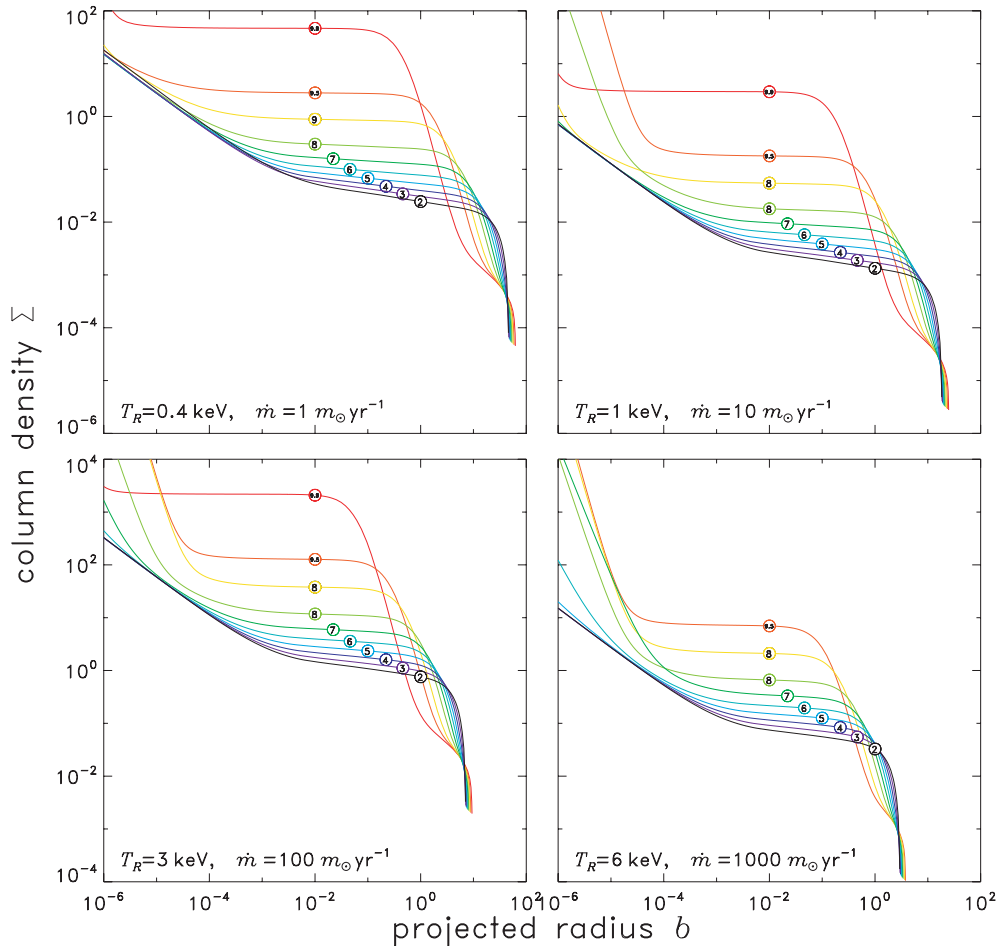


**Figure 21.** Projected profiles of the total projected density,  $\Sigma(b)$ , of  $(m_*, \Upsilon)$ -optimal cluster solutions with different  $F_2$  values (annotated circles). We scale each model to the default total mass,  $m(R) = 40U_m$ .

## 4.2 Extra baryonic and radiative physics

Here we briefly discuss several baryonic phenomena that could potentially modify our quantitative results.

### 4.2.1 Line cooling

The presence of line cooling would break the mass/temperature homology of the solutions assuming bremsstrahlung cooling alone. Additional parameters are therefore needed in the hydrodynamic formulation, thus increasing the dimensionality of the problem and the complexity and computational cost in searching for the structure solutions.

Line emission must affect cooler systems (galaxies and groups) more than rich clusters. The extra cooling may tighten the constraints of the ‘cold’ border, perhaps raising the lower limits on  $m_*/m$  for lighter objects. This may also alter the compactness of clusters of given mass, composition and  $\dot{m}$ : i.e. the  $\Upsilon$ -tracks may shift in the  $(F_2, R)$  plane.

Hydrogen and helium cooling must have been significant for primordial ‘minihaloes’ – hypothetical, metal-free bodies of gas and dark matter that were lighter than modern groups or galaxies. If their radii are smaller than the most compact models in this paper, then minihaloes develop proportionally larger central masses. The contribution of line cooling above bremsstrahlung may raise the

minimal level of  $m_*/m$  further. This supports the notion that massive black holes condensed directly from primordial envelopes, and that condensation may have been as fast as free-fall or the onset of cooling catastrophe.

### 4.2.2 Thermal conduction

The role of thermal conduction in the ICM has been contentious for decades (e.g. Mathews & Bregman 1978; Binney & Cowie 1981; Nulsen et al. 1982; Tucker & Rosner 1983; Stewart et al. 1984; Friaca 1986; Bertschinger & Meiksin 1986; Boehringer & Fabian 1989; Tribble 1989; Suginoara & Ostriker 1998; Narayan & Medvedev 2001; Loeb 2002; Voigt et al. 2002; Kim & Narayan 2003; Zakamska & Narayan 2003; Voigt & Fabian 2004; Conroy & Ostriker 2008). Locally tangled magnetic fields may hinder conduction by inhibiting diffusion transverse to field lines. However, fields that have been aligned radially by a bulk inflow might rather promote radial heat conduction (Bregman & David 1988; Soker & Sarazin 1990). Unsuppressed conduction could warm the coldest layers and lessen radial temperature variations: raising the dip temperature and reducing the  $T_{\max}/T_{\min}$  ratio.

In the conventional models, cluster outskirts have been seen as a plausible reservoir for conductively heating the cool core. This was a natural proposition when solutions were sought in the ‘too cold’ domain, and the whole core was thought to suffer a multiphase,

distributed cooling catastrophe. We emphasize that heat conduction *outwards* from the hot nucleus may also be relevant. These regions are ideal for conduction, since the densities, temperatures and temperature gradients are all high. Conductive cooling of the nucleus must flatten the central temperature and density profiles, dimming the central luminous spot. Some of the central accretion power conducts outwards, ultimately to emerge as ICM luminosity elsewhere. Conductive heating may loosen the constraint of the ‘too cold’ border, enabling smaller  $m_*$  values. We expect this quantitatively, but it requires proof from extended analyses.

#### 4.2.3 Thermal instability

The relevance of thermal instability to the phase structure of cool cores has also been debated since the early theories of cooling flows (Fabian & Nulsen 1977; Mathews & Bregman 1978). In uniform, isobaric conditions, overdense clumps may overcool radiatively in a runaway manner, and condense as a cold phase in thin, hot surroundings (Field 1965). However, dense blobs may rain towards the gravitational centre, resulting in ablation and warming that counteracts instability. Blobs that fall deep and fast enough may reheat via shocks (Cowie, Fabian & Nulsen 1980; Nulsen, Stewart & Fabian 1984). Buoyancy may inhibit instability from the start, by shifting cool or warm blobs to strata of matching entropy. Thermal conduction hinders thermal instability by warming nascent blobs. Local magnetic fields that enwrap blobs might help isolate them, aiding thermal instability and mass dropout. Fields that thread blobs and their surroundings might bind the phases to comove (Nulsen 1986; Thomas et al. 1987).

Studies of thermal instability in interstellar shocks and stellar accretion suggest that local, homogeneous, isobaric analyses are incomplete or too simple for many applications. The shape of the cooling function affects instability; if line-cooling complicates the cooling law then gas is stable at some temperature. Macroscopic flow geometry can be influential: in general the Eulerian operator ( $\partial_t + \mathbf{v} \cdot \nabla$ ) couples temporal evolution with motion and gradients. (See e.g. Chevalier & Imamura 1982; Bertschinger 1986; Saxton & Wu 1999, and references therein.) A better treatment of thermal instability in clusters requires analysis of global structure as well as local physics (e.g. Malagoli, Rosner & Bodo 1987; Balbus & Soker 1989). By retaining temporal terms in the governing equations, our model is ready for stability analyses that relate regional thermal (in)stability to deformations in the halo and gas profiles (in preparation).

However, the strongest original argument for thermal instability fades in our present results. A full treatment of the conservation laws and flow velocity seems to dispel an old illusion of radially varying  $\dot{m}$ . Constant- $\dot{m}$  models resemble observations as well, and so we need not invoke multiphase effects, nor mass dropout across the core. If mass drops out anywhere (for reasons beyond our model) then it happens deep inside the cD galaxy, and we have at least reduced the ‘cooling flow problem’ to a sub-kpc AGN problem (e.g. Tabor & Binney 1993). Without dropout, the cooling flow leads into hot spherical accretion feeding the nucleus.

Having a warm  $T_{\min}$ , our solutions are consistent with the paucity of cold gas and star formation measured at long wavelengths (see review by Donahue & Voit 2004), and also with the X-ray spectroscopic evidence that disfavors widespread mass dropout to very low temperatures (Kaastra et al. 2001; Peterson et al. 2001; Tamura et al. 2001; Peterson et al. 2003). Observations both inside and outside the cooling radius are consistent with single-phase flows but spatially varying temperature (e.g. Böhringer et al. 2001;

David et al. 2001; Molendi & Pizzolato 2001; Etori et al. 2002a; Matsushita et al. 2002). Thus we justify omitting microscale thermal instability and retain a smooth, single-phased flow model.

#### 4.2.4 Stellar material

Our present analyses omit the effects of collisionless, stellar mass. This is justifiable on cluster scales, where stars are effectively passive tracers, and gas comprises most of the baryons. Our formulation also applies directly to primordial structures, if protogalaxies detached from the background before stars became abundant.

Stellar mass dominates within the effective radii of modern elliptical galaxies, such as the brightest central galaxies grown in cluster cores. A stellar mass distribution (see Section D10) may alter our solutions within the central kpc, by deepening the potential there. The extra accretion warming may loosen the ‘cold’ constraints on  $m_*$ . It may also soften the ICM temperature dip. We defer the evaluation of gas/dark dipolytropes in elliptical galaxy potentials for future study.

If the central galaxy is quiescent then direct stellar interactions with the inflow are negligible. It was recognized early that stellar mass-loss in modern elliptical galaxies is weak compared to a cooling cluster’s inflow (e.g. Nulsen et al. 1984), and likely to be smothered in terms of mass, momentum and energy. In our solutions, the central gas is near local virial temperature, already similar to the stellar velocity dispersion. Drag from stellar motions may stir gas locally, but the cross-section and covering factor of stars is too small for much global effect. Thus the main effect of stars is gravitational and limited to the centre (unless a starburst erupts). Starbursts may affect the early life of a cD galaxy, heating nearby gas as an AGN might.

#### 4.2.5 Heating by active galaxies

We omit AGN interactions from our model, in order to focus on the undriven, natural tendency of clusters. Feedback effects require extra semi-empirical terms, with a diabolically tempting number of adjustable parameters. If jet activity or other phenomena drive the cluster medium to convection or turbulence, with eddy kinetic energies comparable to the gaseous internal energy, then the gas gains extra effective degrees of freedom,  $F_1 > 3$ . This may steepen gas density profiles, and shift the ‘cold’ and ‘fast’ constraints on  $m_*$ .

Some authors propose that AGN output (such as the mechanical power of radio lobes) can suppress or even regulate cooling flows (e.g. Tabor & Binney 1993; Binney & Tabor 1995; Brüggen & Kaiser 2001; Churazov et al. 2001; Quilis, Bower & Balogh 2001; Ruszkowski & Begelman 2002; Kaiser & Binney 2003; Ruszkowski, Brüggen & Begelman 2004). There seems enough raw available power for low and medium-mass clusters (Birzan et al. 2004; Allen et al. 2006), but the sufficiency of AGN warming in massive cooling flows is debatable. For AGN to be effective heaters, radio lobes must mix with the ICM, or the gas must be viscous enough to dissipate disturbances. The distribution of AGN power is questionable in some systems: strong jets may cut themselves channels out of the core, dumping their power ineffectually in the outskirts (e.g. Best et al. 2006; Vernaleo & Reynolds 2006). In some clusters, ICM metallicity gradients imply that mixing has not been thorough. Some cool cored clusters lack nuclear activity altogether.

Because of their low entropy, cooling flows may simply sink and slip around the sides least disturbed by AGN channels. If so then

active cooling clusters may still resemble our solutions overall. However, if the AGN blocks the inflow near the centre then the model needs modification there: an additional distributed heating function in  $\mathcal{L}$ , and a local drop in  $\dot{m}$ . Starvation on sub-kpc scales may dim the luminous nucleus. The outskirts (beyond the reach of radio bubbling) should match the standard profiles obtained here.

However, our adaptive model improves or solves key aspects of the ‘cooling flow problem’ without resort to extrinsic heating. Considering a responsive halo, and all relevant momentum and self-gravity terms, we find that steady clusters always develop a floor temperature due to purely gravitational self-warming. This level is high enough to explain the rarity of cold condensates. Consequently, we do not need non-gravitational heating to dominate on Mpc scales. We dispel the need for finely tuned, two-way *feedback* between the cooling flow and the heating processes. Stellar and AGN heating are demoted to an incidental, intermittent role. Heating need not be persistent nor stable.

#### 4.2.6 Relativity, opacity and cosmic rays

In a relativistic formulation, the inner boundary would shift from  $r_* = 0$  to the Schwarzschild radius of the central mass. The bremsstrahlung cooling function acquires relativistic corrections. Gravitational redshift dims the inner boundary. Inflow velocities will be naturally subluminal. As the gas becomes relativistic in the nuclear regions, it gains more effective degrees of freedom,  $F_1 \rightarrow 6$ . This implies a higher combined heat capacity than a normal  $F_1 = 3$  medium. The region where the dark spike verges on Jeans-instability may enlarge. Otherwise the issues of pressure support, the subsonic constraint and the avoidance of cooling catastrophes remain qualitatively unchanged in a relativistic framework.

If gas in the central regions becomes Compton-thick or otherwise dominated by radiation pressure then this will also result in  $F_1 \rightarrow 6$ . This will steepen the gas density spike and may promote collapse of the dark spike. The opaque inner inflow must be radiatively inefficient, enlarging the domain of effectively adiabatic Bondi-like behaviour. We cannot presently say in which direction the  $m_*$  limits change. Subparsec AGN anatomy may complicate the issue.

If cosmic rays contribute significant pressure to the intercluster medium, then they would deserve incorporation as a third fluid in our model. Extra source terms enter the momentum and energy equations to express cosmic ray diffusion and heat exchanges with the coterminous thermal gas. As a relativistic plasma, cosmic rays have  $F_3 \approx 6$  degrees of freedom. The consequences for the innermost structures and  $m_*$  limits may follow cases of a halo with  $F_2 \geq 6$ .

#### 4.2.7 Angular momentum

If some of the cluster gas possesses significant angular momentum then the inflow could deviate from radial streaming at small radii. Some fraction would accrete on to a small disc, of a size determined by rotational support (e.g. Nulsen et al. 1984). This may alter the minimal- $m_*$  limits slightly, and the steady solutions might require some minimal disc surface density profile. If the disc is viscous then it is only a temporary residence for inflowing gas; it ultimately feeds the central mass. A disc that accretes enough mass could self-gravitate and develop density waves, or fragment. This is a recipe for forming spiral galaxies.

However, discs (and filaments) are only viable as long as they avoid contact with similar bodies. Collisions and stirring by asymmetric substructures can restore the spherical approximation in the

long run, and on the scales relevant to our model. Turbulence or convection in the inner regions could easily destroy or preempt a disc, easing angular momentum efflux and quasi-spherical mass influx. Empirically, our spherical approximation is valid as far as relaxed clusters and central galaxies are actually roundish.

A spherical model cannot address the topic of halo substructure directly. Collisionless dark matter cosmogonies overpredict the abundance of satellites at galaxy and group scales by at least an order of magnitude (Klypin et al. 1999; Moore et al. 1999a, 2000; D’Onghia & Lake 2004). Several authors have debated whether a (weakly) SIDM halo can be lumpy and aspherical enough as a gravitational lens and host of satellite galaxies (e.g. Moore et al. 2000; Gnedin & Ostriker 2001; Meneghetti et al. 2001; Furlanetto & Loeb 2002; Natarajan et al. 2002). Dwarf haloes might ablate at dark bow-shocks, or (we suggest) might persist as self-bound, dark eddies that roll as they orbit in a turbulent background. Within a cluster, each galaxy perturbs the cluster profile locally, and each sub-halo centre probably develops a miniature analogue of the spherical inflow solutions.

### 4.3 Nature of dark matter

In detail, our solutions depend on the assumption of a polytropic equation of state for the dark matter. This condition is the emergent equilibrium if Tsallis’ thermostatics govern the halo, even if dark matter lacks non-gravitational interactions entirely. If dark matter is a Bose–Einstein condensate, then it is effectively polytropic in the classical limit (Sin 1994; Goodman 2000). If it is a degenerate fermion gas then it has a more complex equation of state, obtainable by integrating a local distribution function (Munyanza & Biermann 2005, 2006), or else a polynomial approximation (Nakajima & Morikawa 2007). If dark matter is collisionless but ruled by long-range dark forces then a more complicated treatment becomes necessary, analogous to collisionless plasma physics. If dark matter feels strong enough local self-interactions, then it is analogous to an adiabatic ideal gas, and a polytropic equation is expected.

The possibility of local dark self-interactivity (Goodman 2000; Peebles 2000; Spergel & Steinhardt 2000) is theoretically and observationally attractive, but not yet exhaustively tested. This scenario explains the cored halo profiles evident in many galaxies, and may yield more realistic substructure than collisionless cosmogonies. Early numerical studies of weakly self-interacting haloes mimicked SIDM using particle codes with Monte Carlo scattering, which bred realistic cores but found a gravothermal catastrophe that could eventually degrade the cores into isothermal cusps (Berkert 2000; Kochanek & White 2000; Moore et al. 2000; Yoshida et al. 2000a,b; Davé et al. 2001). However, later analyses (Balberg, Shapiro & Inagaki 2002; Ahn & Shapiro 2005) considered more general initial conditions, delaying collapse beyond the Hubble time. Polytropic haloes (as in this paper) can describe a more strongly interacting fluid regime, where the mean free path is short enough that conduction and gravothermal effects vanish.

Despite the indications from galaxy scales, the fashionable preference is to defer and displace the faults of CDM substructure on to ‘baryon feedback’, which is beset with long-term challenges in numerical methods and in theory. The evidence on cluster scales is still ambiguous enough to allow this. Many observers *assume* cuspy profiles in their data fits. (Fully non-parametric modelling remains rare.) For relaxed clusters, some X-ray deprojections show soft-cored halo profiles (e.g. Nevalainen et al. 1999; Etori et al. 2002b; Katayama & Hayashida 2004; Zhang et al. 2005; Voigt &

Fabian 2006; Zhang et al. 2006) while others seem compatible with cusps (e.g. Pointecouteau, Arnaud & Pratt 2005; Vikhlinin et al. 2006). In some cases the total mass profile appears cuspy, but not to the extent expected of a collisionless halo affected by gas (e.g. Zappacosta et al. 2006). Gravitational lensing analyses also give mixed signs: some prefer or allow soft cores (Tyson et al. 1998; Sand et al. 2002; Dahle et al. 2003; Gavazzi et al. 2003; Sand et al. 2004; Diego et al. 2005; Halkola et al. 2006; Rzepecki et al. 2007; Halkola et al. 2008; Sand et al. 2008) while others prefer cusps (Broadhurst et al. 2005; Sharon et al. 2005; Saha et al. 2006; Limousin et al. 2007).

In more violent circumstances, cluster mergers have been treated as probes of dark interactivity. One gravitational lens ‘bullet cluster’ was claimed as a merger of collisionlessly interpenetrating haloes, separating from shocked gas (Clowe et al. 2006). The mass, speed, timing and rarity of the hypothetical merger have been questioned, and well-tuned simulations devised in reply (Hayashi & White 2006; Farrar & Rosen 2007; Springel & Farrar 2007; Milosavljević et al. 2007; Zhao 2007; Angus & McGaugh 2008; Nusser 2008). Subsequently, an antibullet cluster has appeared, where the dark matter is the more dissipative constituent (settled in the middle) while galaxies fly on the periphery (Mahdavi et al. 2007). Another lensing cluster is reported with an encircling ring or shell of dark matter (Jee et al. 2007). Taken together, these special cases tell an inconsistent story about dark physics. However, particular projected morphologies admit multiple interpretations: for instance the ‘bullet’ subcluster velocity vector can be reversed, and the line-of-sight shapes and displacements are unknown. This paper cannot aim to disentangle all the latent assumptions in the dark matter merger problem, but clearly some alternative gestalts are needed. Varieties of SIDM remain among the promising candidates.

In the absence of a central mass or gas inflow, a polytropic halo can have a constant-density core (Section D2), compatible with galaxian evidence. However, for galaxy clusters with inflowing gas, we do not obtain simple cored profiles like those assumed commonly. The presence of inflow requires a central mass for stationarity, and a polytropic cluster halo grows a density spike *within* its core. The spiky haloes are effectively a ‘contraction’ induced by the central mass and gas inflow. For large  $F_2$  or large  $\dot{m}$ , the core radius may be small enough to give a misleading appearance of a NFW-like cusp. Smallness of some observed cluster cores (e.g. Dahle et al. 2003; Katgert et al. 2004; Limousin et al. 2007) is not evidence against SIDM. Rather, it will help to constrain the dark freedom  $F_2$  and the inflow history of baryons. Cluster cores as small as a few tens of kpc are possible if  $F_2$  is large. This fits the concordance favouring  $8 \lesssim F_2 \lesssim 10$ , which minimizes the central mass  $m_*$  (this paper) and agrees with Nunez et al. (2006), who effectively find  $F_2 \approx 9.6$  by fitting galaxy rotation curves.

Given any alternative closed set of equations for the dark dynamics and statics, one can repeat the formulation of this paper, to find another set of differential equations coupling the gas and halo. The interplay of these constituents in their shared potential must always lead to the exclusion of some domains due to cooling catastrophe or acoustic breaks in the gas. However, it must be proven, for each scenario, whether nonzero  $m_*$  is required (as in the model dipolytropes here) and whether structures with cosmic baryon fraction can exist.

## 5 CONCLUSIONS

We have presented a self-consistent two-component model for galaxy clusters, bound by a non-static gravitational potential that

emerges naturally from the solutions along with the co-adapted halo and gas profiles. Applying this formulation to clusters of plausible total mass and composition, we reconcile some of the observational difficulties involving gas inflows due to cooling. Furthermore, we find that stationary solutions of the cluster structure invariably require (or develop) a non-zero central mass.

We have analysed the distribution of cooling gas in a responsive spherical halo of Mpc scale. Mass, momentum and energy continuity are imposed. Bremsstrahlung radiative cooling is allowed to become dynamically significant. All constituents participate gravitationally. Realistic models emerge when dark matter has a polytropic equation of state, which is justified in terms of the equilibria of Tsallis thermostatics, adiabatic dark self-interactions or Bose–Einstein condensation.

We find that there exist steady, continuous solutions spanning all radii inside the halo. The joint constraints of cooling and acoustic continuity set the minimal central mass. The minimal  $m_*$  varies with  $\dot{m}$  and  $F_2$  but only weakly with the gas surface temperature  $T_R$ . The cluster’s total gas fraction is linked with  $\dot{m}$ ,  $R$  and  $T_R$ . The masses,  $\dot{m}$ , densities, temperatures, velocities of any particular solution can rescale to yield another valid solution with the same radial dimensions.

A cosmic baryon fraction and observed SMBH masses are consistent with the halo’s effective microscopic degrees of freedom being in the interval  $7 \lesssim F_2 < 10$ . The lower limits on  $m_*$  are laxer if  $\dot{m}^2/m^3$  is smaller. For cosmic composition, the fiducial total cluster mass and  $\dot{m} \geq 1 \text{ m}_\odot \text{ yr}^{-1}$ , we always find  $m_* \gtrsim 5 \times 10^5 \text{ m}_\odot$  (or  $m_*/m \gtrsim 2 \times 10^{-9}$ ). Smaller central masses are impossible in steady clusters, unless extra physics dominate. To enable  $m_*$  as small as  $10^6\text{--}10^7 \text{ m}_\odot$  in a cluster, we need  $9 \lesssim F_2 < 10$ . This agrees with galaxy rotation models of Nunez et al. (2006) which imply  $F_2 \approx 9.6$ .

The halo density develops a spike around the central mass, surrounded by a flat core attenuating to a fringe on Mpc scales. These layers are less distinct when  $F_2$  is larger. This varied structure remains apparent in projections of the total column density. For  $F_2$  high enough to enable plausible  $m_*$ , we find halo cores with  $10 \lesssim R_1 \lesssim 300 \text{ kpc}$ . Observationally, there are reported core fits with  $15 \lesssim R_1 \lesssim 200 \text{ kpc}$  (e.g. Dahle et al. 2003; Diego et al. 2005; Rzepecki et al. 2007; Halkola et al. 2008) which is similar to what we obtain. We predict that mass profiles steepen beyond NFW in the dim fringe. Given observable scale radii such as  $R_2$ , one could predict the outer radius where a halo naturally truncates.

Our solutions belong outside the inevitably overcooling regime where classic cooling flows were constructed. They naturally provide a non-zero floor temperature, obviating the need for (unobserved) mass dropout and cold condensation. The entropy, density and temperature profiles broadly resemble observed clusters, suggesting that varying the gas parameters may enable detailed fits in future. We find a shallow gas entropy ramp at radii inside the sonic point, rather than a flat isentropic core. In projection, the ICM resembles the classic  $\beta$ -model X-ray profile in the outskirts, plus a peaked cooling/warming core. The central luminous spot is comparable to AGN power, though opacity, conduction and detailed AGN anatomy could probably soften and spread the emission, and lower the radiative efficiency considerably. In the optimal- $m_*$  solutions, the ratio of peak/dip temperatures is a factor of 5–40. This reduces the need for AGN self-regulation (as distinct from incidental heating). The inclusion of thermal conduction and  $F_1 > 3$  might improve the profiles and lessen the AGN role further.

By construction, the classes of solutions that we obtained comprise the steady configurations of bremsstrahlung-cooling

Mpc-scale spheres. If our broad physical assumptions hold, and if structural asymmetries are subdominant, then these solutions represent end points of cluster relaxation. In the configuration space of spherical clusters, the solutions are fixed points. If feedback or non-gravitational heating processes become globally, persistently important, then they drive the evolving cluster state in a forced orbit around those natural points.

A temporary disturbance of the system may cause a local cooling catastrophe or acoustic disconnection, and the structure must somehow adjust until reaching another steady state in neighbouring configuration space. Our analysis does not outline a particular evolutionary path, but the profiles offer clues. The critical bottlenecks for gas continuity occur at radial scales typical of elliptical galaxies. This may be a preferred layer for cold gas dropout and star formation, during any transient, externally driven detour into cooling catastrophe. Stability analyses are needed to determine whether our scenario implies regulation or runaway monolithic collapse. For  $F_2 > 6$ , the innermost halo is only marginally Jeans-stable, implying that large-amplitude disturbances could trigger a local gravitational collapse of dark matter (without involving the gas directly). This mechanism for dark growth of SMBH may turn out to be an important process (besides baryonic feeding and gravitational ejection) influencing SMBH demographics.

## ACKNOWLEDGMENTS

We thank Ignacio Ferreras for comprehensive, stimulating and helpful discussions. We thank the referee, Michael Loewenstein, for abundantly constructive criticism. We acknowledge the use of numerical routines provided by the Gnu Scientific Library project.

## REFERENCES

- Adami C., Mazure A., Ulmer M. P., Savine C., 2001, *A&A*, 371, 11  
 Agertz O. et al., 2007, *MNRAS*, 380, 963  
 Ahn K., Shapiro P. R., 2005, *MNRAS*, 363, 1092  
 Allen S. W., Schmidt R. W., Fabian A. C., 2001, *MNRAS*, 328, L37  
 Allen S. W., Dunn R. J. H., Fabian A. C., Taylor G. B., Reynolds C. S., 2006, *MNRAS*, 372, 21  
 Anders E., Grevesse N., 1989, *Geochim. Cosmochim. Acta*, 53, 197  
 Angus G. W., McGaugh S. S., 2008, *MNRAS*, 383, 417  
 Arbey A., Lesgourgues J., Salati P., 2003, *Phys. Rev. D*, 68, 023511  
 Arnaud M., Evrard A. E., 1999, *MNRAS*, 305, 631  
 Arnaud M., Pointecouteau E., Pratt G. W., 2005, *A&A*, 441, 893  
 Bagchi J., Durret F., Neto G. B. L., Paul S., 2006, *Sci*, 314, 791  
 Bahcall J. N., Sarazin C. L., 1977, *ApJ*, 213, L99  
 Balberg S., Shapiro S. L., 2002, *Phys. Rev. Lett.*, 88, 101301  
 Balberg S., Shapiro S. L., Inagaki S., 2002, *ApJ*, 568, 475  
 Balbus S. A., Soker N., 1989, *ApJ*, 341, 611  
 Barth A. J., Martini P., Nelson C. H., Ho L. C., 2003, *ApJ*, 594, L95  
 Bauer F. E., Fabian A. C., Sanders J. S., Allen S. W., Johnstone R. M., 2005, *MNRAS*, 359, 1481  
 Begelman M. C., 1978, *MNRAS*, 184, 53  
 Begelman M. C., 1979, *MNRAS*, 187, 237  
 Begelman M. C., Nath B. B., 2005, *MNRAS*, 361, 1387  
 Bertschinger E., 1986, *ApJ*, 304, 154  
 Bertschinger E., Meiksin A., 1986, *ApJ*, 306, L1  
 Best P. N., Kaiser C. R., Heckman T. M., Kauffmann G., 2006, *MNRAS*, 368, L67  
 Binney J., Cowie L. L., 1981, *ApJ*, 247, 464  
 Binney J., Tabor G., 1995, *MNRAS*, 276, 663  
 Binney J., Tremaine S., 1987, *Galactic Dynamics*. Princeton Univ. Press, Princeton, NJ, p. 747  
 Birzan L., Rafferty D. A., McNamara B. R., Wise M. W., Nulsen P. E. J., 2004, *ApJ*, 607, 800  
 Blumenthal G. R., Faber S. M., Flores R., Primack J. R., 1986, *ApJ*, 301, 27  
 Boehringer H., Fabian A. C., 1989, *MNRAS*, 237, 1147  
 Bogdanović T., Reynolds C. S., Miller M. C., 2007, *ApJ*, 661, L147  
 Böhmer C. G., Harko T., 2007, *J. Cosmology Astropart. Phys.*, 6, 25  
 Böhringer H. et al., 2001, *A&A*, 365, L181  
 Bondi H., 1952, *MNRAS*, 112, 195  
 Bradač M. et al., 2008, *ApJ*, 681, 187  
 Branduardi-Raymont G., Fabricant D., Feigelson E., Gorenstein P., Grindlay J., Soltan A., Zamorani G., 1981, *ApJ*, 248, 55  
 Bregman J. N., David L. P., 1988, *ApJ*, 326, 639  
 Brighenti F., Mathews W. G., 2003, *ApJ*, 587, 580  
 Broadhurst T., Takada M., Umetsu K., Kong X., Arimoto N., Chiba M., Futamase T., 2005, *ApJ*, 619, L143  
 Brüggén M., Kaiser C. R., 2001, *MNRAS*, 325, 676  
 Bryan G. L., Norman M. L., 1998, *ApJ*, 495, 80  
 Bullock J. S., Dekel A., Kolatt T. S., Kravtsov A. V., Klypin A. A., Porciani C., Primack J. R., 2001, *ApJ*, 555, 240  
 Burkert A., 1995, *ApJ*, 447, L25  
 Burkert A., 2000, *ApJ*, 534, L143  
 Campanelli M., Lousto C., Zlochower Y., Merritt D., 2007a, *ApJ*, 659, L5  
 Campanelli M., Lousto C. O., Zlochower Y., Merritt D., 2007b, *Phys. Rev. Lett.*, 98, 231102  
 Carlberg R. G. et al., 1997, *ApJ*, 485, L13  
 Cavaliere A., Fusco-Femiano R., 1976, *A&A*, 49, 137  
 Chandrasekhar S., 1939, *An Introduction to the Study of Stellar Structure*. The University of Chicago Press, Chicago, IL  
 Chevalier R. A., Imamura J. N., 1982, *ApJ*, 261, 543  
 Churazov E., Brüggén M., Kaiser C. R., Böhringer H., Forman W., 2001, *ApJ*, 554, 261  
 Ciotti L., Bertin G., 1999, *A&A*, 352, 447  
 Clowe D., Bradač M., Gonzalez A. H., Markevitch M., Randall S. W., Jones C., Zaritsky D., 2006, *ApJ*, 648, L109  
 Conroy C., Ostriker J. P., 2008, *ApJ*, 681, 151  
 Cowie L. L., Binney J., 1977, *ApJ*, 215, 723  
 Cowie L. L., Fabian A. C., Nulsen P. E. J., 1980, *MNRAS*, 191, 399  
 Dahle H., Hannestad S., Sommer-Larsen J., 2003, *ApJ*, 588, L73  
 Davé R., Spergel D. N., Steinhardt P. J., Wandelt B. D., 2001, *ApJ*, 547, 574  
 David L. P., Nulsen P. E. J., McNamara B. R., Forman W., Jones C., Ponman T., Robertson B., Wise M., 2001, *ApJ*, 557, 546  
 de Blok W. J. G., 2005, *ApJ*, 634, 227  
 de Blok W. J. G., McGaugh S. S., 1997, *MNRAS*, 290, 533  
 De Grandi S., Molendi S., 2002, *ApJ*, 567, 163  
 de Vaucouleurs G., 1948, *Ann. Astrophys.*, 11, 247  
 Di Matteo T., Allen S. W., Fabian A. C., Wilson A. S., Young A. J., 2003, *ApJ*, 582, 133  
 Diego J. M., Sandvik H. B., Protopapas P., Tegmark M., Benítez N., Broadhurst T., 2005, *MNRAS*, 362, 1247  
 Diemand J., Moore B., Stadel J., 2004, *MNRAS*, 353, 624  
 Diemand J., Zemp M., Moore B., Stadel J., Carollo C. M., 2005, *MNRAS*, 364, 665  
 Dolag K., Bartelmann M., Perrotta F., Baccigalupi C., Moscardini L., Meneghetti M., Tormen G., 2004, *A&A*, 416, 853  
 Donahue M., Voit G. M., 2004, in Mulchaey J. S., Dressler A., Oemler A., eds, *Clusters of Galaxies: Probes of Cosmological Structure and Galaxy Evolution, Cool Gas in Clusters of Galaxies*. Cambridge University Press, Cambridge, UK, p. 143  
 D’Onghia E., Lake G., 2004, *ApJ*, 612, 628  
 Douglas N. G. et al., 2007, *ApJ*, 664, 257  
 Dubinski J., Carlberg R. G., 1991, *ApJ*, 378, 496  
 Edge A. C., Fabian A. C., Allen S. W., Crawford C. S., White D. A., Böhringer H., Voges W., 1994, *MNRAS*, 270, L1  
 Eke V. R., Navarro J. F., Frenk C. S., 1998, *ApJ*, 503, 569  
 Emden R., 1907, *Gaskugeln*. Verlag B. G. Teubner, Leipzig, Berlin  
 Ettori S., Fabian A. C., Allen S. W., Johnstone R. M., 2002a, *MNRAS*, 331, 635  
 Ettori S., De Grandi S., Molendi S., 2002b, *A&A*, 391, 841  
 Ettori S., Fabian A. C., 1999, *MNRAS*, 305, 834

- Fabian A. C., Nulsen P. E. J., 1977, *MNRAS*, 180, 479
- Fabian A. C., Hu E. M., Cowie L. L., Grindlay J., 1981, *ApJ*, 248, 47
- Fabian A. C., Nulsen P. E. J., Canizares C. R., 1984a, *Nat*, 310, 733
- Fabian A. C., Stewart G. C., Nulsen P. E. J., Itoh H., Canizares C. R., 1984b, *Nat*, 307, 343
- Fabian A. C., Canizares C. R., Boehringer H., 1994, *ApJ*, 425, 40
- Fabian A. C., Voigt L. M., Morris R. G., 2002, *MNRAS*, 335, L71
- Farrar G. R., Rosen R. A., 2007, *Phys. Rev. Lett.*, 98, 171302
- Field G. B., 1965, *ApJ*, 142, 531
- Finoguenov A., Arnaud M., David L. P., 2001, *ApJ*, 555, 191
- Firmani C., D'Onghia E., Chincarini G., Hernández X., Avila-Reese V., 2001, *MNRAS*, 321, 713
- Flores R. A., Primack J. R., 1994, *ApJ*, 427, L1
- Forestell A., Gebhardt K., 2008, *ApJ*, submitted
- Friaca A. C. S., 1986, *A&A*, 164, 6
- Furlanetto S. R., Loeb A., 2002, *ApJ*, 565, 854
- Gavazzi R., Fort B., Mellier Y., Pelló R., Dantel-Fort M., 2003, *A&A*, 403, 11
- George M. R., Fabian A. C., Sanders J. S., Young A. J., Russell H. R., 2008, *MNRAS*, submitted (arXiv:0807.1130)
- Gilmore G., Wilkinson M. I., Wyse R. F. G., Kleyna J. T., Koch A., Evans N. W., Grebel E. K., 2007, *ApJ*, 663, 948
- Gnedin O. Y., Ostriker J. P., 2001, *ApJ*, 561, 61
- Gnedin O. Y., Kravtsov A. V., Klypin A. A., Nagai D., 2004, *ApJ*, 616, 16
- Goerdt T., Moore B., Read J. I., Stadel J., Zemp M., 2006, *MNRAS*, 368, 1073
- Gonzalez A. H., Zaritsky D., Zabludoff A. I., 2007, *ApJ*, 666, 147
- González J. A., Spherhake U., Brüggemann B., Hannam M., Husa S., 2007, *Phys. Rev. Lett.*, 98, 091101
- Goodman J., 2000, *New Astron.*, 5, 103
- Gorenstein P., Fabricant D., Topka K., Harnden F. R., Jr, Tucker W. H., 1978, *ApJ*, 224, 718
- Graham A. W., Merritt D., Moore B., Diemand J., Terzić B., 2006, *AJ*, 132, 2701
- Gull S. F., Northover K. J. E., 1975, *MNRAS*, 173, 585
- Haiman Z., 2004, *ApJ*, 613, 36
- Halkola A., Seitz S., Pannella M., 2006, *MNRAS*, 372, 1425
- Halkola A., Hildebrandt H., Schrabbach T., Lombardi M., Bradač M., Erben T., Schneider P., Wuttke D., 2008, *A&A*, 481, 65
- Hansen S. H., 2005, *New Astron.*, 10, 371
- Hayashi E., White S. D. M., 2006, *MNRAS*, 370, L38
- Hennawi J. F., Ostriker J. P., 2002, *ApJ*, 572, 41
- Hernquist L., 1990, *ApJ*, 356, 359
- Horedt G. P., 1986, *Ap&SS*, 126, 357
- Hubble E. P., 1930, *ApJ*, 71, 231
- Ikebe Y., Reiprich T. H., Böhringer H., Tanaka Y., Kitayama T., 2002, *A&A*, 383, 773
- Jee M. J. et al., 2007, *ApJ*, 661, 728
- Johnstone R. M., Fabian A. C., Edge A. C., Thomas P. A., 1992, *MNRAS*, 255, 431
- Johnstone R. M., Allen S. W., Fabian A. C., Sanders J. S., 2002, *MNRAS*, 336, 299
- Jones C., Forman W., 1984, *ApJ*, 276, 38
- Kaastra J. S., Ferrigno C., Tamura T., Paerels F. B. S., Peterson J. R., Mittaz J. P. D., 2001, *A&A*, 365, L99
- Kaastra J. S. et al., 2004, *A&A*, 413, 415
- Kaiser C. R., Binney J., 2003, *MNRAS*, 338, 837
- Kaiser N., 1986, *MNRAS*, 222, 323
- Katayama H., Hayashida K., 2004, *Adv. Space Res.*, 34, 2519
- Katger P., Biviano A., Mazure A., 2004, *ApJ*, 600, 657
- Kay S. T., 2004, *MNRAS*, 347, L13
- Kim W.-T., Narayan R., 2003, *ApJ*, 596, 889
- King I. R., 1966, *AJ*, 71, 64
- King I. R., 1972, *ApJ*, 174, L123
- Kleyna J. T., Wilkinson M. I., Gilmore G., Evans N. W., 2003, *ApJ*, 588, L21
- Klypin A., Kravtsov A. V., Valenzuela O., Prada F., 1999, *ApJ*, 522, 82
- Kochanek C. S., White M., 2000, *ApJ*, 543, 514
- Kuzio de Naray R., McGaugh S. S., de Blok W. J. G., Bosma A., 2006, *ApJS*, 165, 461
- Lane J. H., 1870, *Am. J. Sci. Arts*, 50, 57
- Lee J.-W., 2008, (arXiv:0801.1442)
- Lea S. M., Silk J., Kellogg E., Murray S., 1973, *ApJ*, 184, L105
- Lemze D., Barkana R., Broadhurst T. J., Rephaeli Y., 2008, *MNRAS*, 386, 1092
- Liesenborgs J., de Rijcke S., Dejonghe H., Bekaert P., 2008, *MNRAS*, 389, 415
- Lima Neto G. B., Gerbal D., Márquez I., 1999, *MNRAS*, 309, 481
- Limousin M. et al., 2007, *ApJ*, 668, 643
- Lin Y.-T., Mohr J. J., Stanford S. A., 2003, *ApJ*, 591, 749
- Lloyd-Davies E. J., Ponman T. J., Cannon D. B., 2000, *MNRAS*, 315, 689
- Loeb A., 2002, *New Astron.*, 7, 279
- Loewenstein M., 2000, *ApJ*, 532, 17
- Łokas E. L., 2002, *MNRAS*, 333, 697
- Lumb D. H. et al., 2004, *A&A*, 420, 853
- Lynden-Bell D., 1967, *MNRAS*, 136, 101
- Macciò A. V., Dutton A. A., van den Bosch F. C., Moore B., Potter D., Stadel J., 2007, *MNRAS*, 378, 55
- Madau P., Quataert E., 2004, *ApJ*, 606, L17
- Mahdavi A., Hoekstra H., Babul A., Balam D. D., Capak P. L., 2007, *ApJ*, 668, 806
- Makino N., Sasaki S., Suto Y., 1998, *ApJ*, 497, 555
- Malagoli A., Rosner R., Bodo G., 1987, *ApJ*, 319, 632
- Markevitch M., 1998, *ApJ*, 504, 27
- Márquez I., Lima Neto G. B., Capelato H., Durret F., Gerbal D., 2000, *A&A*, 353, 873
- Mathews W. G., Baker J. C., 1971, *ApJ*, 170, 241
- Mathews W. G., Bregman J. N., 1978, *ApJ*, 224, 308
- Matsushita K., Belsole E., Finoguenov A., Böhringer H., 2002, *A&A*, 386, 77
- Meneghetti M., Yoshida N., Bartelmann M., Moscardini L., Springel V., Tormen G., White S. D. M., 2001, *MNRAS*, 325, 435
- Merritt D., Navarro J. F., Ludlow A., Jenkins A., 2005, *ApJ*, 624, L85
- Milosavljević M., Koda J., Nagai D., Nakar E., Shapiro P. R., 2007, *ApJ*, 661, L131
- Mohr J. J., Mathiesen B., Evrard A. E., 1999, *ApJ*, 517, 627
- Molendi S., Pizzolato F., 2001, *ApJ*, 560, 194
- Moore B., 1994, *Nat*, 370, 629
- Moore B., Governato F., Quinn T., Stadel J., Lake G., 1998, *ApJ*, 499, L5
- Moore B., Ghigna S., Governato F., Lake G., Quinn T., Stadel J., Tozzi P., 1999a, *ApJ*, 524, L19
- Moore B., Quinn T., Governato F., Stadel J., Lake G., 1999b, *MNRAS*, 310, 1147
- Moore B., Gelato S., Jenkins A., Pearce F. R., Quilis V., 2000, *ApJ*, 535, L21
- Munyanza F., Biermann P. L., 2005, *A&A*, 436, 805
- Munyanza F., Biermann P. L., 2006, *A&A*, 458, L9
- Nakajima T., Morikawa M., 2007, *ApJ*, 655, 135
- Narayan R., Medvedev M. V., 2001, *ApJ*, 562, L129
- Natarajan P., Loeb A., Kneib J.-P., Smail I., 2002, *ApJ*, 580, L17
- Navarro J. F., Frenk C. S., White S. D. M., 1996, *ApJ*, 462, 563
- Navarro J. F., Frenk C. S., White S. D. M., 1997, *ApJ*, 490, 493
- Navarro J. F. et al., 2004, *MNRAS*, 349, 1039
- Neumann D. M., 2005, *A&A*, 439, 465
- Neumann D. M., Arnaud M., 1999, *A&A*, 348, 711
- Nevalainen J., Markevitch M., Forman W., 1999, *ApJ*, 526, 1
- Noh W. F., 1987, *J. Comput. Phys.*, 72, 78
- Novicki M. C., Sornig M., Henry J. P., 2002, *AJ*, 124, 2413
- Nulsen P. E. J., 1986, *MNRAS*, 221, 377
- Nulsen P. E. J., Stewart G. C., Fabian A. C., Mushotzky R. F., Holt S. S., Ku W. H.-M., Malin D. F., 1982, *MNRAS*, 199, 1089
- Nulsen P. E. J., Stewart G. C., Fabian A. C., 1984, *MNRAS*, 208, 185
- Nunez D., Sussman R. A., Zavala J., Cabral-Rosetti L. G., Matos T., 2006, in Pérez M. A., Urrutia L., Villaseñor L., eds, *AIP Conf. Ser. Vol. 857, Particles and Fields: X Mexican Workshop*. Am. Inst. Phys., New York, p. 316

- Nusser A., 2008, MNRAS, 384, 343  
 Ostriker J. P., 2000, Phys. Rev. Lett., 84, 5258  
 O'Sullivan E., Vrtillek J. M., Harris D. E., Ponman T. J., 2007, ApJ, 658, 299  
 Peebles P. J. E., 2000, ApJ, 534, L127  
 Peterson J. R., Fabian A. C., 2006, Phys. Rep., 427, 1  
 Peterson J. R. et al., 2001, A&A, 365, L104  
 Peterson J. R., Kahn S. M., Paerels F. B. S., Kaastra J. S., Tamura T., Bleeker J. A. M., Ferrigno C., Jernigan J. G., 2003, ApJ, 590, 207  
 Piffaretti R., Jetzer P., Kaastra J. S., Tamura T., 2005, A&A, 433, 101  
 Plastino A. R., Plastino A., 1993, Phys. Lett. A, 174, 384  
 Plummer H. C., 1911, MNRAS, 71, 460  
 Pointecouteau E., Arnaud M., Pratt G. W., 2005, A&A, 435, 1  
 Ponman T. J., Cannon D. B., Navarro J. F., 1999, Nat, 397, 135  
 Ponman T. J., Sanderson A. J. R., Finoguenov A., 2003, MNRAS, 343, 331  
 Pratt G. W., Arnaud M., 2002, A&A, 394, 375  
 Pratt G. W., Arnaud M., 2003, A&A, 408, 1  
 Pratt G. W., Arnaud M., Pointecouteau E., 2006, A&A, 446, 429  
 Pratt G. W., Böhringer H., Croston J. H., Arnaud M., Borgani S., Finoguenov A., Temple R. F., 2007, A&A, 461, 71  
 Press W. H., Teukolsky S. A., Vetterling W. T., Flannery B. P., 1992, Numerical Recipes in c. The Art of Scientific Computing, 2nd edn. Cambridge Univ. Press, Cambridge  
 Prugniel P., Simien F., 1997, A&A, 321, 111  
 Quilis V., Bower R. G., Balogh M. L., 2001, MNRAS, 328, 1091  
 Read J. I., Saha P., Macciò A. V., 2007, ApJ, 667, 645  
 Romanowsky A. J., Douglas N. G., Arnaboldi M., Kuijken K., Merrifield M. R., Napolitano N. R., Capaccioli M., Freeman K. C., 2003, Sci, 301, 1696  
 Rood H. J., Page T. L., Kintner E. C., King I. R., 1972, ApJ, 175, 627  
 Russell P. A., Ponman T. J., Sanderson A. J. R., 2007, MNRAS, 378, 1217  
 Ruszkowski M., Begelman M. C., 2002, ApJ, 581, 223  
 Ruszkowski M., Brüggem M., Begelman M. C., 2004, ApJ, 611, 158  
 Rybicki G. B., Lightman A. P., 1979, Radiative Processes in Astrophysics. Wiley, New York  
 Rzepecki J., Lombardi M., Rosati P., Bignamini A., Tozzi P., 2007, A&A, 471, 743  
 Saha P., Read J. I., 2008, ApJ, in press (arXiv:0807.4737)  
 Saha P., Read J. I., Williams L. L. R., 2006, ApJ, 652, L5  
 Sakelliou I. et al., 2002, A&A, 391, 903  
 Sand D. J., Treu T., Ellis R. S., 2002, ApJ, 574, L129  
 Sand D. J., Treu T., Smith G. P., Ellis R. S., 2004, ApJ, 604, 88  
 Sand D. J., Treu T., Ellis R. S., Smith G. P., Kneib J.-P., 2008, ApJ, 674, 711  
 Sarazin C. L., O'Connell R. W., 1983, ApJ, 268, 552  
 Saxton C. J., Wu K., 1999, MNRAS, 310, 677  
 Saxton C. J., Wu K., Cropper M., Ramsay G., 2005, MNRAS, 360, 1091  
 Schnittman J. D., Buonanno A., 2007, ApJ, 662, L63  
 Sellwood J. A., McGaugh S. S., 2005, ApJ, 634, 70  
 Sérsic J. L., 1968, Atlas de galaxias australes. Observatorio Astronomico, Cordoba, Argentina  
 Sharon K. et al., 2005, ApJ, 629, L73  
 Shaw L. D., Weller J., Ostriker J. P., Bode P., 2006, ApJ, 646, 815  
 Silk J., 1976, ApJ, 208, 646  
 Silk J., 2005, MNRAS, 364, 1337  
 Silk J., Rees M. J., 1998, A&A, 331, L1  
 Simon J. D., Bolatto A. D., Leroy A., Blitz L., Gates E. L., 2005, ApJ, 621, 757  
 Sin S.-J., 1994, Phys. Rev. D, 50, 3650  
 Soker N., Sarazin C. L., 1990, ApJ, 348, 73  
 Soltan A., 1982, MNRAS, 200, 115  
 Spergel D. N., Steinhardt P. J., 2000, Phys. Rev. Lett., 84, 3760  
 Spergel D. N. et al., 2003, ApJS, 148, 175  
 Spergel D. N. et al., 2007, ApJS, 170, 377  
 Springel V., Farrar G. R., 2007, MNRAS, 380, 911  
 Stewart G. C., Fabian A. C., Nulsen P. E. J., Canizares C. R., 1984, ApJ, 278, 536  
 Suginohara T., Ostriker J. P., 1998, ApJ, 507, 16  
 Tabor G., Binney J., 1993, MNRAS, 263, 323  
 Tamura T. et al., 2001, A&A, 365, L87  
 Thomas P. A., Fabian A. C., Nulsen P. E. J., 1987, MNRAS, 228, 973  
 Tozzi P., Norman C., 2001, ApJ, 546, 63  
 Tribble P. C., 1989, MNRAS, 238, 1247  
 Tsallis C., 1988, J. Stat. Phys., 52, 479  
 Tucker W. H., Rosner R., 1983, ApJ, 267, 547  
 Tyson J. A., Kochanski G. P., dell'Antonio I. P., 1998, ApJ, 498, L107  
 Umetsu K., Broadhurst T., 2008, ApJ, 684, 177  
 Vernaleo J. C., Reynolds C. S., 2006, ApJ, 645, 83  
 Vikhlinin A., Forman W., Jones C., 1999, ApJ, 525, 47  
 Vikhlinin A., Markevitch M., Murray S. S., Jones C., Forman W., Van Speybroeck L., 2005, ApJ, 628, 655  
 Vikhlinin A., Kravtsov A., Forman W., Jones C., Markevitch M., Murray S. S., Van Speybroeck L., 2006, ApJ, 640, 691  
 Voigt L. M., Fabian A. C., 2004, MNRAS, 347, 1130  
 Voigt L. M., Fabian A. C., 2006, MNRAS, 368, 518  
 Voigt L. M., Schmidt R. W., Fabian A. C., Allen S. W., Johnstone R. M., 2002, MNRAS, 335, L7  
 Voit G. M., Kay S. T., Bryan G. L., 2005, MNRAS, 364, 909  
 Volonteri M., 2007, ApJ, 663, L5  
 Walker M. G., Mateo M., Olszewski E. W., Gnedin O. Y., Wang X., Sen B., Woodroffe M., 2007, ApJ, 667, L53  
 Walter F. et al., 2003, Nat, 424, 406  
 Weldrake D. T. F., de Blok W. J. G., Walter F., 2003, MNRAS, 340, 12  
 White D. A., Fabian A. C., Allen S. W., Edge A. C., Crawford C. S., Johnstone R. M., Stewart G. C., Voges W., 1994, MNRAS, 269, 589  
 White R. E. III, Sarazin C. L., 1987, ApJ, 318, 612  
 Willott C. J., McLure R. J., Jarvis M. J., 2003, ApJ, 587, L15  
 Xu H., Makishima K., Fukazawa Y., Ikebe Y., Kikuchi K., Ohashi T., Tamura T., 1998, ApJ, 500, 738  
 Yoshida N., Springel V., White S. D. M., Tormen G., 2000a, ApJ, 535, L103  
 Yoshida N., Springel V., White S. D. M., Tormen G., 2000b, ApJ, 544, L87  
 Zakamska N. L., Narayan R., 2003, ApJ, 582, 162  
 Zappacosta L., Buote D. A., Gastaldello F., Humphrey P. J., Bullock J., Brighenti F., Mathews W., 2006, ApJ, 650, 777  
 Zavala J., Núñez D., Sussman R. A., Cabral-Rosetti L. G., Matos T., 2006, J. Cosmology Astropart. Phys., 6, 8  
 Zhang Y.-Y., Böhringer H., Mellier Y., Soucail G., Forman W., 2005, A&A, 429, 85  
 Zhang Y.-Y., Böhringer H., Finoguenov A., Ikebe Y., Matsushita K., Schuecker P., Guzzo L., Collins C. A., 2006, A&A, 456, 55  
 Zhao H., 1996, MNRAS, 278, 488  
 Zhao H., 2007, Phys. Rev. D, submitted (arXiv:0704.0094)

## APPENDIX A: NATURAL UNITS

If the gas has approximately solar composition then the bremsstrahlung constant has a value  $B = B_{\odot} \approx 5.06 \times 10^{16} \text{ g}^{-1} \text{ cm}^4 \text{ s}^{-2}$ , calculated according to Rybicki & Lightman (1979) (for a Gaunt factor  $g_B = 1.25$ ) as in Saxton et al. (2005) with the abundance tables of Anders & Grevesse (1989). We parametrize the composition dependency of  $B$  relative to the solar value as a correction factor,  $\zeta \equiv B/B_{\odot}$ . Values of  $\zeta$  depend on the abundance-weighted ionic mass ( $\bar{m}$ ), charge ( $\bar{Z}$ ) and charge squared ( $\bar{Z}^2$ ),

$$\zeta \propto \frac{\bar{Z}^2}{\bar{Z}} \left( \frac{\bar{Z}}{\bar{m}/m_e + \bar{Z}} \right)^{3/2} \sqrt{\frac{\bar{Z}}{1 + \bar{Z}}} g_B. \quad (\text{A1})$$

For astrophysical plasmas,  $\zeta$  is close to unity: for the same  $g_B$  in a pure H plasma,  $\zeta \approx 0.979$ ; for a 9:1 mix of H and He,  $\zeta \approx 0.925$ .

If we define a system of units such that  $B = 1$  and the gravitational constant  $G = 6.6732 \times 10^{-8} \text{ g}^{-1} \text{ cm}^3 \text{ s}^{-2} = 1$  also, then the unit of length is

$$U_x \equiv B/G = 7.58 \times 10^{23} \zeta \text{ cm} = 0.246 \zeta \text{ Mpc}, \quad (\text{A2})$$

It may be significant that this scale, which is natural to any object governed by self-gravity and optically thin bremsstrahlung, is

typical of the observed X-ray core radii of galaxy clusters (e.g. Jones & Forman 1984).

If we adopt a velocity scale where  $\sigma^2 = 1$  corresponds to a temperature of 1 keV, then the unit of velocity is

$$U_v = 3.95 \times 10^7 \text{ cm s}^{-1}, \quad (\text{A3})$$

which implies a time unit

$$U_t \equiv U_x/U_v = 1.92 \times 10^{16} \zeta \text{ s} = 0.608 \zeta \text{ Gyr}. \quad (\text{A4})$$

The age of the universe (Spergel et al. 2003) is presently thought to be  $\sim 22.5/\zeta$ . The unit of mass arises from

$$U_m \equiv U_x^3 U_t^{-2} G^{-1} = 1.77 \times 10^{46} \zeta \text{ g} = 8.91 \times 10^{12} \zeta M_\odot, \quad (\text{A5})$$

and the unit of density is

$$U_\rho \equiv U_m U_x^{-3} = 4.07 \times 10^{-26} \zeta^{-2} \text{ g cm}^{-3}. \quad (\text{A6})$$

The critical density for the universe today is  $\rho_c = 2.33 \times 10^{-4} \zeta^2 U_\rho$ , and the mean matter density is  $\Omega_m \rho_c \approx 6.23 \times 10^{-5} \zeta^2 U_\rho$ . The unit of particle number density depends on plasma composition in a more complicated way:

$$U_n \equiv \frac{U_\rho}{\bar{m} + \bar{Z}m_e}. \quad (\text{A7})$$

For solar composition we have  $U_n \approx 3.96 \times 10^{-2} \text{ cm}^{-3}$ . The units of mass accretion and power are

$$U_{\dot{m}} \equiv U_m/U_t = 1.47 \times 10^4 M_\odot \text{ yr}^{-1}, \quad (\text{A8})$$

$$U_L \equiv U_m U_v^2/U_t = 1.44 \times 10^{45} \text{ erg s}^{-1} = 3.77 \times 10^{11} L_\odot, \quad (\text{A9})$$

and neither depends on composition,  $\zeta$ .

## APPENDIX B: SCALING RELATIONS

Given one steady cluster model, it is possible to construct a set of equivalent models that differ only by uniform multiplicative rescaling of the physical variables. Let us define the transformation factors as

$$\begin{aligned} r &\rightarrow X_r r, \\ m &\rightarrow X_m m, \\ \dot{m} &\rightarrow X_{\dot{m}} \dot{m}, \\ \sigma^2 &\rightarrow X_\sigma \sigma^2, \\ s &\rightarrow X_s s, \\ v &\rightarrow X_v v \end{aligned} \quad (\text{B1})$$

and

$$\rho \rightarrow X_\rho \rho.$$

Mass conservation (9) implies a constraint

$$X_{\dot{m}} = X_r^2 X_\rho X_v. \quad (\text{B2})$$

The equations of the mass profile, such as (15) or (41), require that

$$X_m = X_\rho X_r^3. \quad (\text{B3})$$

Mach numbers must be left unchanged during the transformation, and thus

$$X_v^2 = X_\sigma. \quad (\text{B4})$$

In each of the gas equations, say (31), all of the additive terms must rescale by the same product. After some evaluation, this implies that

$$X_m = X_\sigma X_r = X_\rho X_r^2. \quad (\text{B5})$$

Satisfaction of (B3) and (B5) implies that the spatial dimensions cannot vary,

$$X_r = 1. \quad (\text{B6})$$

Therefore, any valid similarity transformation parametrized by a scale  $X$ , implies the following scaling factors for the key physical variables:

$$\begin{aligned} X_m &= X_\rho = X_\sigma = X, \\ X_v &= X^{1/2}, \\ X_{\dot{m}} &= X^{3/2}, \\ X_s &= X^{(F-2)/F}. \end{aligned} \quad (\text{B7})$$

Luminosities and surface brightness scale as  $X_L = X_{\dot{m}} X_v^2 = X^{5/2}$ , so the X-ray luminosity scales as  $m^{5/2}$  within any family of solutions. The relations (B7) imply the existence of two invariant length-scales, associated with the mass inflow and temperatures:

$$R_m \equiv \sqrt{\gamma_1 \sigma_1 m / \dot{m}} \Big|_R, \quad (\text{B8})$$

$$R_\sigma \equiv Gm / \gamma_1 \sigma_1^2 \Big|_R. \quad (\text{B9})$$

The latter is algebraically equivalent to the sonic radius in simple, adiabatic Bondi accretion, although cooling and self-gravity mean that our models needn't develop a sonic point nor  $\mathcal{M}^2$  extremum at this radius. Together, the parameters ( $F_1$ ,  $F_2$ ,  $R$ ,  $R_m$ ,  $R_\sigma$ ) uniquely denote a set of homologous cluster models.

## APPENDIX C: EFFECTIVE DEGREES OF FREEDOM

The key property of an ideal fluid is  $F$ , the effective degrees of freedom. Thus  $F$  is a qualitatively decisive parameter of the halo models. In ordinary space, free particles have three translational degrees of freedom. If the particles are individual, point-like entities lacking substructure then  $F = 3$ . However, many physically motivated scenarios entail  $F > 3$  or non-integer values.

If individual particles can rotate, twist or distort then there are additional internal microscopic degrees of freedom (e.g.  $F = 5$  for a diatomic gas). Highly relativistic or radiation-dominated fluids have  $F = 6$  (e.g. cosmic ray contributions to ICM pressure). Larger integer values of  $F$  could also occur if the particles experience higher spatial dimensions, e.g. if their de Broglie wavelength is smaller than the scale of compact hidden dimensions. If a fluid includes subspecies that do not fully interact, then the effective  $F$  is larger than for single species.

Some alternative scenarios involve fewer degrees of freedom. If the fluid is a classical Bose–Einstein condensate (as in Goodman 2000; Arbey, Lesgourgues & Salati 2003; Böhmer & Harko 2007; Lee 2008) then  $F = 2$ , for an equation of state  $p \propto \rho^2$ . A case  $F = 1$  could describe constrained particles, analogous to beads on an abacus. An incompressible fluid corresponds to  $F = 0$ . Isobaric conditions can be described by  $F = -2$ .

If non-local physical interactions are important, and the medium is described by Tsallis' statistics (Tsallis 1988), then  $F$  is effectively some non-integer,  $F = (3q - 1)/(q - 1)$  for some constant  $q$  (Plastino & Plastino 1993; Hansen 2005; Nunez et al. 2006; Zavala et al. 2006). In a gravitational context, this includes and entails the ephemeral constraints and interactions present on all intermediate levels between the small scale of two-body scattering and the large scale of the global potential. Other mesoscale physics, such as the energy associated with turbulent eddies, can also provide larger, non-integer values of  $F$ . If highly efficient heat transport processes operate then the fluid approaches isothermality and  $F \rightarrow \infty$ .

## APPENDIX D: STANDARD GASLESS HALO MODELS

### D1 Comparative measures of a halo

To found our treatment of two-fluid cluster models, we will here review the intrinsic properties of polytropic haloes (without gas), and contrast them with other halo models in the literature. In order to compare theoretical and semi-empirical halo models with each other and with observations, it is necessary to define some global physical measurements. Every real halo ought to have a finite outer radius,  $R$ , but the invisibility of dark matter means that  $R$  is not directly determinable. In practice, the cluster's baryons are only visible out to certain detection limits (e.g. to a limiting X-ray flux) and this extent sets lower bounds on  $R$ . We prefer to characterize the models using spatial measurements (which can be compared to the true outer radius) since these are invariant under mass rescaling (Appendix B).

For non-singular and cored halo models, a ‘King radius’ is defined in terms of the central conditions (e.g. Binney & Tremaine 1987, p. 228)

$$R_K = \sqrt{9\sigma^2/4\pi G\rho} \Big|_{r=0}. \quad (D1)$$

This scale typifies the extent of the flat density core in many models. The cluster rescaling (Appendix B) leaves  $R_K$  invariant. However,  $R_K$  is undefined for cuspy haloes or those with a central point mass. Thus we require alternative measures of core size and overall halo concentration.

First, let us define a radius that contains a majority of the mass, or that typifies the central concentration. We refer to a sphere's total mass  $m$  and moment of inertia,

$$I = \frac{8\pi}{3} \int_0^\infty \rho r^4 dr \quad (D2)$$

which give a mass-weighted lever radius,

$$R_I \equiv \sqrt{5I/2m}, \quad (D3)$$

which is scaled such that  $R_I = R$  for a uniform sphere. The radius  $R_I$  is applicable to models where the core is not explicitly parametrized. Since density decreases monotonically in  $r$ , the inner layers dominate  $R_I$ . When the mass is centrally peaked or the core is small compared to the fringe, the ratio  $R_I/R$  is small. Though the true surface may be invisible below some flux or density thresholds, truncated observational estimates of  $R_I$  or  $R_I/R$  might still approximate the global values acceptably.

We define another radial scale measuring the cluster's self-gravity. The gravitational potential energy of a spheroid,

$$W = -4\pi G \int_0^\infty m \rho r dr = 2\pi \int_0^\infty \Phi \rho r^2 dr, \quad (D4)$$

is finite for realistic models. This leads to the definition of a gravitational radius,

$$R_w = -Gm^2/W \quad (D5)$$

(see Binney & Tremaine 1987, p. 68), which can be regarded as the size of energetically typical orbits in the halo.

Halo structure can be diagnosed by observable kinematic tracers, such as velocities of gas clouds or stars in circular orbits in a galaxy, or the motions of galaxies within a cluster. The circular orbital

velocity of test particles peaks at some radius  $R_0$  if

$$(4\pi\rho r^3 - m) \Big|_{r=R_0} = 0$$

and

$$\frac{d \ln \rho}{d \ln r} \Big|_{r=R_0} \leq -2. \quad (D6)$$

We denote a sequence of signature radii where the logarithmic density slope passes specific values:

$$\frac{d \ln \rho}{d \ln r} \Big|_{r=\{R_1, R_2, R_3, R_4, \dots\}} = \{-1, -2, -3, -4, \dots\}. \quad (D7)$$

For instance,  $\rho \propto r^{-3}$  at the slope 3 radius  $R_3$ , and so on. These slope radii may be multivalued, if the density profile undulates (i.e. exhibiting concentric, alternating steep and flat layers). If the halo is radially finite ( $R < \infty$ ) then all slope radii are finite too. Infinite models may lack some of the slope radii. If the rotation curve peaks anywhere, then (D6) implies that  $R_0 \geq R_2$ . The total mass cannot be finite without  $R_3$  existing. A finite moment of inertia and  $R_I$  requires finite  $R_5$ . Finite  $W$  and  $R_w$  require  $R_{2.5}$  and  $R_3$  to occur at least once in the outskirts.

The literature on cosmological simulations conventionally defines a ‘virial radius’,  $R_v$ , enclosing a mean density that is some multiple,  $\delta_c$ , of the cosmic critical density. This overdensity is in the range  $100 \lesssim \delta_c \lesssim 200$ , depending on the cosmological model. As in Bryan & Norman (1998), we use  $\delta_c = 18\pi^2 + 82(\Omega_m - 1) - 39(\Omega_m - 1)^2$ , corresponding to idealized spherical collapse, and  $\Omega_m = 0.27$  such that

$$\frac{3m_v}{4\pi R_v^3} \approx 97.01 \rho_c \approx 0.02259 U_\rho. \quad (D8)$$

The virial radius conveniently measures idealized, radially infinite models, or numerical simulacra which are unresolved in their fringes. The drawback of  $R_v$  is that it loses information about the outskirts. It also fails to characterize compact objects where  $R_v$  encloses the entire mass (e.g. the most compact ( $m_*$ ,  $\Upsilon$ )-optimal models with  $R < 1$  Mpc). Since  $R_v$  is defined relative to an absolute density, it does *not* transform neatly under mass and temperature rescaling (Appendix B). On the other hand, it is always possible to rescale the cluster masses so that  $R_v = R$  or some other signature radius (Section 3.5). The same is true for King models or any model with at least one free scale.

X-ray imagery and gravitational lensing studies constrain the column densities of gas and dark matter, as projected on to the plane of the sky. Thus it is useful to calculate comparative two-dimensional projected properties. An effective half-light radius,  $R_e$ , is conventionally defined by a line-of-sight cylinder that encircles half the emission (or projected mass). If the total mass and halo radius were known, then we can also define a radius  $R_\Sigma$  for the image contour with mean brightness (or column density),  $\bar{\Sigma} = m/\pi R^2$ .

### D2 Gasless polytropic halo

Here, for the sake of clarifying our main results, we review the intrinsic behaviour of finite polytropic dark haloes *without* gas. We will examine the influence of a central point mass. The upper blocks of Table D1 characterize a set of gasless polytropic haloes, of different degrees of freedom, with and without a central mass.

The first subset lack a central mass ( $m_* = 0$ ), and share the same entropy and central density:  $s = 1, \rho(0) = 1$ . Fig. D1 shows their density profiles. These solutions are classical Lane–Emden spheres

**Table D1.** Signature radii and masses of some representative gasless halo models. From left- to right-hand side, the columns are: dark degrees of freedom, surface radius; inertial concentration; gravitational concentration; the density slope radii with indices  $-2$ ,  $-3$  and  $-4$ ; the rotation-curve peak radius; the projected mean light radius and effective radius; total mass. Models marked ‘★’, ‘●’ and ‘●●’ contain a central point mass,  $m_* = 10^{-8}$ ,  $10^{-6}$  and  $10^{-5} m_*$ , respectively.

$F$	$R$	$R_I/R$	$R_w/R$	$R_2/R$	$R_3/R$	$R_4/R$	$R_o/R$	$R_\Sigma/R$	$R_e/R$	$m/\rho_s r_s^3$
2	1.253	0.8084	0.8000	0.6458	0.7286	0.7817	0.8733	0.6524	0.4636	2.507
3	1.630	0.7152	0.7368	0.5200	0.6141	0.6813	0.7500	0.6025	0.3980	3.026
4	2.127	0.6222	0.6667	0.4126	0.5076	0.5830	0.6229	0.5500	0.3353	3.534
5	2.826	0.5287	0.5882	0.3191	0.4076	0.4860	0.4989	0.4943	0.2748	4.040
6	3.891	0.4340	0.5000	0.2369	0.3135	0.3895	0.3810	0.4345	0.2162	4.555
7	5.706	0.3374	0.4000	0.1645	0.2251	0.2932	0.2708	0.3693	0.1594	5.091
8	9.444	0.2376	0.2857	0.1010	0.1426	0.1965	0.1695	0.2955	0.1043	5.668
9	21.06	0.1313	0.1540	0.04587	0.06678	0.09880	0.07829	0.2050	0.05094	6.323
9.5	44.91	0.07286	0.08027	0.02164	0.03198	0.04947	0.03722	0.1444	0.02509	6.707
9.5★	44.91	0.07286	0.01019	0.02164	0.03198	0.04947	0.03722	0.1444	0.02506	6.707
7●	5.706	0.3374	0.3999	0.1645	0.2251	0.2932	0.2708	0.3693	0.1594	5.091
8●	9.444	0.2376	0.04766	0.1010	0.1426	0.1965	0.1695	0.2955	0.1040	5.668
9●	21.06	0.003432	1.429(−5)	1.702(−4)	3.674(−4)	9.730(−4)	2.451(−4)	0.02658	2.754(−4)	6.323
9.5●	44.91	1.766(−4)	5.217(−6)	1.089(−5)	1.871(−5)	3.656(−5)	1.827(−5)	0.005347	1.474(−5)	6.707
6●●	3.891	0.4340	0.4999	0.2369	0.3135	0.3895	0.3810	0.4345	0.2161	4.555
7●●	5.706	0.3374	0.05895	0.1645	0.2251	0.2932	0.2708	0.3693	0.1594	5.091
8●●	9.444	0.04559	1.061(−6)	–	0.008330	0.04773	–	0.1138	0.004818	5.668
9●●	21.06	5.554(−5)	1.252(−7)	6.603(−7)	1.432(−6)	3.829(−6)	9.464(−7)	0.002563	1.072(−6)	6.323
9.5●●	44.91	2.688(−6)	5.486(−8)	8.617(−8)	1.481(−7)	2.894(−7)	1.445(−7)	5.631(−4)	1.167(−7)	6.707
SIS	$\infty$	$\sqrt{5}/3$	1	0	–	–	–	–	–	$\infty$
NIS	$\infty$	$\sqrt{5}/3$	1	$1.357R_K$	–	–	$2.998R_K$	–	–	$\infty$
PIS	$\infty$	$\sqrt{5}/3$	1	$\infty$	–	–	$1r_s$	–	–	$\infty$
Hubble	$\infty$	0	0	$\sqrt{2}r_s$	$\infty$	–	$2.920r_s$	–	–	$\infty$
NFW	$\infty$	0	0	$1r_s$	$\infty$	–	$2.163r_s$	–	–	$\infty$
Burkert	$\infty$	0	0	$1.521r_s$	$\infty$	–	$3.245r_s$	–	–	$\infty$
Hernquist	$\infty$	0	$6r_s$	$0.5r_s$	$2r_s$	$\infty$	$1r_s$	–	$1.815r_s$	$2\pi$
King $c=\frac{1}{2}$	$10^c R_K$	0.4685	0.5277	0.2484	0.3400	0.4316	0.4075	0.4535	0.2318	0.8142
$c=1$	$10^c R_K$	0.3514	0.3823	0.1174	0.2064	0.3476	0.2156	0.3721	0.1457	0.5436
$c=\frac{3}{2}$	$10^c R_K$	0.2557	0.2840	0.04112	0.1342	0.3493	0.08297	0.3236	0.08841	0.4024
$c=2$	$10^c R_K$	0.2098	0.2868	0.01340	0.1990	0.3738	0.02852	0.3276	0.07970	0.3951
$c=\frac{5}{2}$	$10^c R_K$	0.3238	0.2575	0.004282	0.2332	0.3831	0.009384	0.3559	0.1100	0.4669
Sérsic $n=2$	$\infty$	$3.421r_s$	$3.235r_s$	$0.4946r_s$	$1.557r_s$	$3.213r_s$	$0.9748r_s$	–	$1.002r_s$	33.27
$n=3$	$\infty$	$5.039r_s$	$3.132r_s$	$0.2541r_s$	$1.571r_s$	$4.840r_s$	$0.5355r_s$	–	$1.001r_s$	40.02
$n=4$	$\infty$	$7.418r_s$	$2.965r_s$	$0.1290r_s$	$1.578r_s$	$7.277r_s$	$0.2835r_s$	–	$0.9999r_s$	45.79

of index  $n = F/2$  (Lane 1870; Emden 1907; Chandrasekhar 1939; Horedt 1986). We prefer  $F$  as the more physically motivated notation. Each sphere has a core of nearly uniform density, surrounded by declining outskirts. For smaller  $F$  the core is a larger fraction of the volume, and the fringe is steeper. If  $F < 10$  then the halo possesses a zero-density outer surface at radius  $R$ . These finite polytropes do not tend to any asymptotic outer slope; the density index steepens infinitely as  $r \rightarrow R$ .

With central conditions held constant, the radius and mass increase with  $F$ , and the binding energy increases both in absolute terms and per unit mass. In absolute terms,  $R_I$  increases slightly with  $F$ . Proportionally, the core ( $R_I/R$ ), the gravitational radius ( $R_w/R$ ), the two-dimensional radii ( $R_\Sigma/R$ ,  $R_e/R$ ) and the rotation peak ( $R_o/R$ ) all shrink with  $F$ . The slope radii ( $R_2$ ,  $R_3$ ,  $R_4$ ) also shrink with rising  $F$ . They become multivalued for large  $F$  (the index of  $\rho$  wobbles in some layers). In such cases, we tabulate the steepening point farthest on the edge of the core. This tends to be near the peak of the rotation curve. We generally find that  $R_o > R_3$  and  $R_I > R_4$ . Consecutive slope indices ( $R_2, R_3, R_4, \dots$ ) occur in roughly even

steps, but the steps ultimately diminish near the true surface ( $R$ ). In non-singular haloes,  $R_w \approx R_I$ . As  $F$  increases, all the signature radii shrink relative to  $R$  in a common manner (see Fig. D2).

However, the non-singular model is a specially contrived condition. Most galaxies are thought to contain a point-like central mass such as a nuclear star cluster or black hole. At cluster scales, the analogous object is a cD galaxy or its black hole. To clarify the effect of such a mass, we tabulate singular polytropic haloes with central masses in astronomically realistic proportions:  $m_*/m = 10^{-8}, 10^{-6}, 10^{-5}$ . We fixed the total mass and  $R$  of corresponding Lane–Emden spheres, but vary the entropy. Fig. D3 shows density profiles for  $m_*/m = 10^{-8}$ . The central object draws a density spike about itself, of index  $-F/2$ . Beyond this sharp sphere of influence, the halo flattens into a core, then steepens into outskirts and a surface like those of non-singular models. For small or medium  $F$ , the addition of  $m_* > 0$  reduces the slope radii ( $R_2, R_3, R_4$ ) slightly. However, for sufficiently large  $F$  and  $m_*$ , the spike steepens the entire core, to the point where  $R_2$  and higher slope radii vanish.

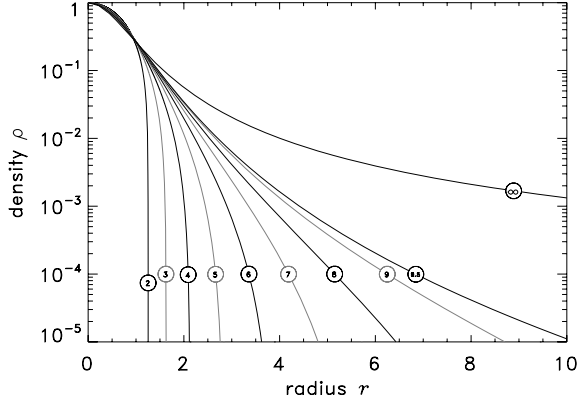


**Figure D1.** Density profiles of polytropic dark haloes with different adiabatic indices,  $\gamma = 1 + 2/F$ , but no gas and no central mass. We set  $s = 1$  and  $\rho = 1$  at the origin. Labels denote the effective degrees of freedom  $F$  in each case. For large  $F$  the flat core fills less of the total volume. The case  $F = \infty$  is the non-singular isothermal sphere ('NIS', Section D3).

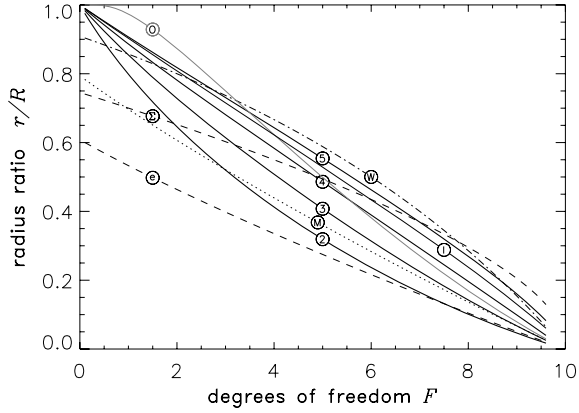


**Figure D2.** Signature radii (as fractions of the surface radius  $R$ ) of non-singular ( $m_* = 0$ ) finite polytropic halo models. Bold curves mark the density slope radii,  $R_2/R$ ,  $R_3/R$ ,  $R_4/R$  and  $R_5/R$ . 'I' marks the lever radius,  $R_l/R$ . 'M' marks the half-mass radius,  $R_m/R$ . 'W' marks the gravitational radius,  $R_w/R$ . 'O' traces peaks of the rotation velocity,  $R_o/R$ . Two-dimensional projected quantities are marked 'Σ' ( $R_\Sigma/R$  the mean-brightness radius) and 'e' ( $R_e/R$  the half-light radius). These radii stay bundled together but shrink in relation to the surface as  $F$  rises.

For  $F > 9$ , the spike develops density undulations (at subparsec scales for a cluster). In this tiny, deep core, the slope radii are multivalued and the rotation curve peaks multiply. Some undulations locally approach the brink of Jeans stability. The dense spike reduces  $R_l$  and  $R_w$  dramatically for  $F \geq 8$ .

Table D1 reveals several trends for as  $m_*/m$  varies. As  $m_*$  increases,  $R_w/R$  changes appreciably before the slope radii and rotation peak do. The two-dimensional projected quantities ( $R_\Sigma/R$ ,  $R_e/R$ ) are the least sensitive to the central mass. Large  $F$  enhances the sensitivity of all the of signature radii with respect to  $m_*$ .

If  $F \geq 10$  then the halo density attenuates indefinitely ( $R = \infty$ ), regardless of  $m_*$ . The borderline case of  $F = 10$  has an infinite radius but finite mass: this is the well-known Plummer (1911) model, where  $\rho \propto r^{-5}$  at large radii. In the isothermal limit,  $F \rightarrow \infty$ , the fringe declines like  $\rho \propto r^{-2}$  (Section D3).

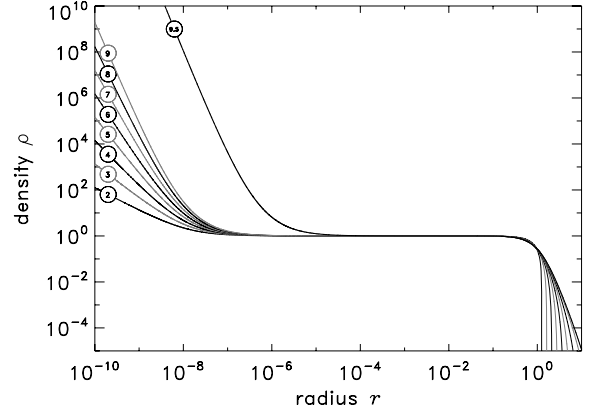


**Figure D3.** Density profiles of gasless polytropic halo models in the presence of a central gravitating mass ( $m_* = 10^{-8} m$ ). Curves are annotated with their respective  $F$  values.

### D3 Isothermal spheres

If the particle velocities are isotropic and  $\sigma^2$  is constant everywhere, then the halo is an 'isothermal sphere'. This is essentially an extreme polytrope in the limit  $F \rightarrow \infty$ . Isothermality is plausible when some strong mechanism asserts global thermal equilibrium: e.g. thorough and violent relaxation (Lynden-Bell 1967), or efficient thermal conduction. Isothermal spheres are popular toy models in gravitational lensing studies. Such haloes also predict flat rotation curves, resembling the observed outer parts of disc galaxies.

The density profile depends on the central boundary condition. The 'non-singular isothermal sphere' (NIS) has  $d\rho/dr = 0$  at the origin, exhibiting a shallow density core, but at large radii it tends to a decline  $\propto r^{-2}$  (see e.g. Binney & Tremaine 1987, and the  $F = \infty$  curve in Fig. D1). The 'singular isothermal sphere' (SIS) has a self-similar profile,

$$\rho = \sigma^2 / 2\pi G r^2. \quad (\text{D9})$$

For NIS and SIS,  $R_3$  and higher slope radii never occur. The density fails to vanish at any finite radius, so the halo lacks a distinct surface. Within some ad hoc truncation radius, the mass, moment of inertia and gravitational potential energy of the SIS are

$$m = 2\sigma^2 r / G, \\ I = 4\sigma^2 r^3 / 9G$$

and

$$W = -4\sigma^4 r / G. \quad (\text{D10})$$

It follows that the gravitational radius  $R_w = r$  and the effective lever radius  $R_l = \sqrt{5}r/3$ . For the SIS, the circular velocity is radially constant. A SIS gravitational lens bends light rays by a constant angle at all projected radii. The SIS virial radius is

$$R_v = \left[ \frac{3\sigma^2}{2\pi G \delta_c \rho_c} \right]^{1/2} \approx 4.598\sigma \quad (\text{D11})$$

which is  $\approx 1.130$  Mpc for a halo at 1-keV temperature.

### D4 Pseudo-isothermal sphere

In some observational studies the exact non-singular isothermal sphere is approximated by an empirical cored profile that also has  $\propto r^{-2}$  outskirts. The 'pseudo-isothermal sphere' (PIS) has a density

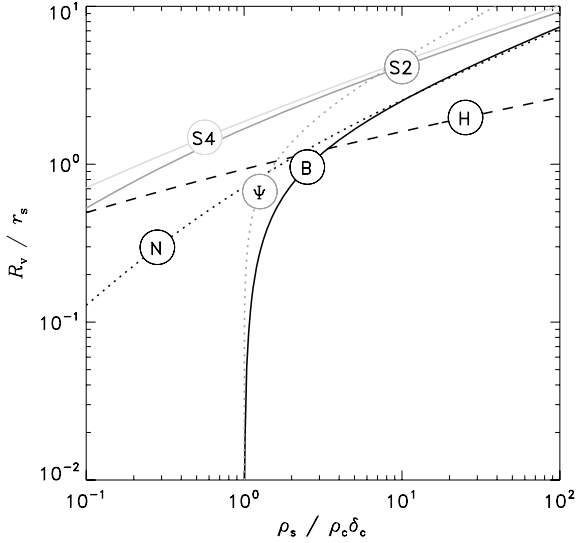


**Figure D4.** The dependency of the virial radius upon the halo's density at its scale radius, for: pseudo-isothermal ( $\Psi$ ); NFW (N); Burkert (B); Hernquist (H); Sérsic  $n = 2, 4$  (S2,S4) models.

profile

$$\rho = \frac{\rho_s}{1 + x^2}, \quad (\text{D12})$$

where  $x = r/r_s$  and  $(\rho_s, r_s)$  are some density and radial scales. The PIS has infinite radius, mass and moment of inertia. At large radii,  $R_I/r = \sqrt{5}/3$  and  $R_w/r = 1$ . The slope 2 radius is at infinity, as is the peak circular velocity ( $R_2 = R_o = \infty$ ). Fig. D4 shows numerical solutions for the virial radius depending on  $(\rho_s, r_s)$ , comparing PIS to some other radially infinite models.

### D5 Hubble profile and $\beta$ -model atmospheres

The modified Hubble profile (Hubble 1930; King 1972; Rood et al. 1972) approximates the projected mass or brightness of any non-singular cored sphere as

$$\Sigma \approx \frac{\Sigma_0}{1 + x^2}, \quad (\text{D13})$$

defined such that the intensity drops to half its central value ( $\Sigma_0$ ) at the projected radius scale  $r_s$ . This empirical fit has been applied to the stellar light profiles of elliptical galaxies, globular clusters and galaxy clusters. The corresponding spatial density profile is

$$\rho \approx \frac{\rho_s}{(1 + x^2)^{3/2}}. \quad (\text{D14})$$

This distribution yields more realistic rotation curves than the isothermal models, as there is a peak at finite radius,  $R_o \approx 2.920r_s$  (e.g. Binney & Tremaine 1987, p. 39). However, the model is only applicable in and near the core, otherwise it implies infinite radius, mass, potential energy and moment of inertia. As  $r \rightarrow \infty$  we have  $R_I \rightarrow \infty$ ,  $R_w \rightarrow \infty$ ,  $R_1/r \rightarrow 0$  and  $R_w/r \rightarrow 0$ . The density slope radii are  $R_2 = \sqrt{2}r_s$  and  $R_3 = \infty$ .

The model was extended to describe the X-ray emitting gas by assuming isothermality and local hydrostasis in cluster cores, e.g. Lea et al. (1973) who assigned identical temperatures to gas and galaxies. Cavaliere & Fusco-Femiano (1976) assumed a galaxy/gas temperature ratio of  $\beta = \sigma_*^2/\sigma_g^2$ , deriving a gas density profile

$$\rho = \rho_0 \left[ 1 + (r/r_c)^2 \right]^{-3\beta/2}, \quad (\text{D15})$$

and X-ray surface brightness profile

$$S = S_0 \left[ 1 + (b/b_c)^2 \right]^{-3\beta+1/2}, \quad (\text{D16})$$

where  $b$  is the projected radius. This became a commonplace fitting formula for X-ray imaging observations (e.g. Bahcall & Sarazin 1977; Gorenstein et al. 1978; Branduardi-Raymont et al. 1981; Jones & Forman 1984; Neumann & Arnaud 1999). Shorn of the original isothermal assumption, more recent studies adopt either (D15) or (D16) as a conventional template, and seek to infer actual radial variations of temperature from the data. It is worth emphasising that the  $\beta$ -model is a parametrization or an idealization of the innermost observable regions. The ultimate outer density index is  $-3\beta$ , and the implied asymptotic gas mass is infinite unless  $\beta > 1$  (according to D15). However, equation (D16) implies that the luminosity is infinite if  $1 < \beta < 2$ . This breakdown implies that the density and/or temperature must attenuate even more steeply in the outskirts of real clusters. Indeed, some observations show that  $\beta$  steepens (e.g. Vikhlinin, Forman & Jones 1999; Neumann 2005).

### D6 Hernquist profile

Hernquist (1990) proposed an analytic model for galaxy spheroids, with density profile that attenuates infinitely

$$\rho = \frac{m_\infty}{2\pi x(1+x)^3 r_s^3} \quad (\text{D17})$$

but none the less yielding a finite mass profile

$$m(r) = m_\infty \frac{x^2}{(1+x)^2}. \quad (\text{D18})$$

The moment of inertia is infinite. The density slope passes integer values at  $x_2 = 1/2$ ,  $x_3 = 2$  and  $x_4 = \infty$ . The rotation curve peaks at the scale radius,  $x_0 = 1$ . The projected central brightness is infinite, but the outskirts decline fast enough that  $R_e$  is finite. Fig. D4 shows the relation between virial radius and  $(\rho_s, r_s)$ .

### D7 N-body simulacra

Dubinski & Carlberg (1991) found that collisionless structures emerging in  $N$ -body cosmological simulations develop a cuspy, power-law central density profile. The 'NFW profile' (Navarro, Frenk & White 1996, 1997) is a popular empirical fit to such haloes, with a density that follows

$$\rho = \frac{\rho_s}{x(1+x)^2}, \quad (\text{D19})$$

where  $x = r/r_s$  and  $(\rho_s, r_s)$  are fitting parameters of a particular halo. These parameters follow trends in relation to the halo mass, which depend on cosmology (e.g. Bullock et al. 2001; Dolag et al. 2004; Shaw et al. 2006; Macciò et al. 2007). Physically, the scale radius  $r_s = R_2$ , the slope 2 radius. This radius defines a concentration,  $c \equiv R_v/r_s$ . A halo truncated at some finite radius has a mass and moment of inertia of

$$m = 4\pi\rho_s r_s^3 \left[ \ln(1+x) - \frac{x}{1+x} \right], \quad (\text{D20})$$

$$I = \frac{8\pi}{3} \rho_s r_s^5 \left[ \frac{3}{2} + \frac{1}{1+x} + \frac{(x+1)(x-5)}{2} + 3 \ln(1+x) \right]. \quad (\text{D21})$$

There is not an outer surface, and both  $m$  and  $I$  are infinite as  $x \rightarrow \infty$ . The inertial radius  $R_I \rightarrow \infty$  at infinity, while its concentration ratio vanishes ( $R_I/r \rightarrow 0$ ), which means that the rotational properties

depend on an ad hoc truncation radius. The gravitational potential energy is finite,

$$W = -8\pi^2 G \rho_s^2 r_s^5. \quad (\text{D22})$$

Thus  $R_w \rightarrow \infty$  and  $R_w/r \rightarrow 0$  at large radii. The rotation curve peaks at  $R_0 \approx 2.163 r_s$ . Using (D19) and (D20), the virial radius equation (D8) is transcendental. (See Fig. D4 for numerical solutions.)

Moore et al. (1999b) and Zhao (1996) proposed variations and generalizations to the NFW formula, consisting of a broken radial power law again, but with different indices. Expressions for the global quantities differ slightly from those above, but the models are qualitatively similar: infinite in mass and radius, and ill-defined rotational properties. More recent work (Merritt et al. 2005; Graham et al. 2006) suggests that Sérsic profiles (Section D10) fit simulated collisionless haloes better.

Density slopes of the simulacra are least certain on the outskirts and near the origin, both places where mass resolution degrades. Cuspy profiles emerge consistently from cosmological  $N$ -body simulations, but the causes of this shape still lack a comprehensive analytic derivation. Possible causes may involve: cosmic expansion, ongoing infall and accretion history; the simplifying assumption of a collisionless medium; the approximation of discretized mass; implicit low-pass filtration in numerical Poisson solvers; or perhaps other less obvious computational and physical factors.

### D8 Burkert profile

Burkert (1995) proposed an empirical halo model based on observed rotation curves of halo-dominated galaxies,

$$\rho = \frac{\rho_s}{(1+x)(1+x^2)}, \quad (\text{D23})$$

where we denote a normalized radius again,  $x = r/r_s$ . The density index is  $-2$  at  $R_2 \approx 1.521 r_s$ . The index ultimately approaches  $-3$ ;  $R_3 = \infty$ . There is a flat density core, like in the non-singular polytropic and King models (and unlike the cuspy NFW and Sérsic profiles). The mass and inertial moment enclosed at  $x$  are

$$m = \pi \rho_s r_s^3 [2 \ln(1+x) + \ln(1+x^2) - 2 \arctan x], \quad (\text{D24})$$

$$I = \frac{2\pi}{3} \rho_s r_s^5 \left\{ 2x^2 - 4x + 2 \arctan x + \ln \left[ \frac{(1+x)^2}{1+x^2} \right] \right\}, \quad (\text{D25})$$

and both are infinite as  $r \rightarrow \infty$ . As with NFW, the Burkert halo mass is intensely centrally concentrated:  $R_1/r \rightarrow 0$  as  $r \rightarrow \infty$ . The gravitational potential energy is finite,

$$W = -4\pi^3 \ln 2 G \rho_s^2 r_s^5, \quad (\text{D26})$$

and  $R_w/r \rightarrow 0$  at large radii. The rotation curve peaks at  $R_0 \approx 3.245 r_s$ . Like the NFW halo, the virial radius equation is transcendental (Fig. D4 shows numerical solutions).

### D9 King model

King (1966) presented a cored stellar dynamical model, derived from first principles. Its basis is a phase-space density function,

$$\mathcal{F}(\mathbf{r}, \mathbf{v}) = A \left[ e^{-a(\Phi + v^2/2)} - e^{-a\Phi_1} \right], \quad (\text{D27})$$

assuming locally isotropic particle velocities, truncating at some escape energy corresponding to the equipotential ( $\Phi_1$ ) of a zero-density outer surface at ‘tidal radius’,  $R = r_1$ . The model is a self-consistent description of a non-isolated, self-bound, collisionless

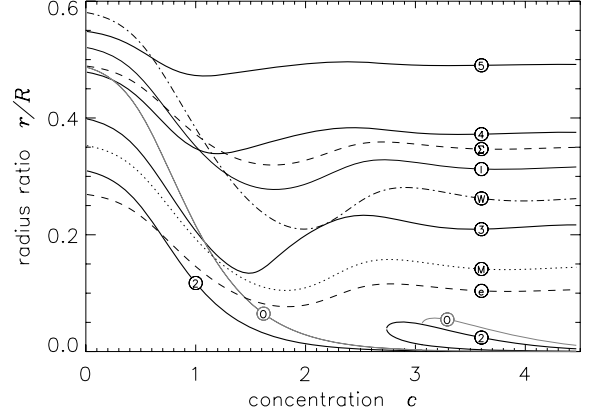


**Figure D5.** Signature radii relative to the tidal surface, for King models with various concentrations,  $c = \log_{10}(R/R_K)$ . Lines and annotations are the same as in Fig. D2. The signature radii span much of the halo volume (unlike high- $F$  polytropic haloes). Their ratios stay roughly steady as  $c$  increases.

sphere. It was originally applied to globular clusters with escaping stars. Firmani et al. (2001) reapplied it to cored, thermal, self-interacting dark haloes. The mass, moment of inertia and gravitational potential energy are all finite. The local density,

$$\rho = \frac{8\pi}{3} \sqrt{\frac{2}{a^3}} A e^{-a\Phi_1} e^\psi \Gamma\left(\frac{5}{2}, \psi\right), \quad (\text{D28})$$

depends on the dimensionless potential offset,

$$\psi \equiv a [\Phi_1 - \Phi(r)], \quad (\text{D29})$$

and  $\Gamma$  is the lower incomplete gamma function. At the outer boundary,  $\rho = \psi = 0$ . Radial coordinates for the equipotentials are obtained by solving the Poisson equation, subject to the inner boundary conditions  $\psi > 0$  and  $\nabla\psi = 0$ . The latter condition precludes a central mass,  $m_* = 0$ .

Like the  $F < 10$  polytropes, the King model is radially finite. Thus the slope radii ( $R_2, R_3, R_4$ ) are also finite, and the density index attains large negative values near the edge. Concentrations are conventionally denoted by  $c \equiv \log_{10}(R/R_K)$ . Fig. D5 shows the variation of signature radii with  $c$ . Both  $R_2/R$  and  $R_0/R$  drop rapidly with increasing  $c$ , and they are multivalued for highly concentrated models,  $c \gtrsim 2.7$ . The other main signature radii vary only within factors of a few in the shown domain ( $0 \leq c \leq 4.5$ ).

### D10 Sérsic profile

The Sérsic (1968) model is an empirical fit to the two-dimensional projected starlight of spheroids such as elliptical galaxies and spiral bulges:

$$\Sigma = \Sigma_e \exp[-b(x^{1/n} - 1)]. \quad (\text{D30})$$

The radial coordinate is scaled in terms of the half-light radius,  $x = r/R_e$ . The shape parameter  $n \approx 4$  for elliptical galaxies (the classic profile of de Vaucouleurs 1948) or  $n \sim 2$  for galaxy clusters. The parameter  $b$  depends on  $n$  implicitly, via lower incomplete and complete gamma functions,

$$2\Gamma(2n, b) = \Gamma(2n). \quad (\text{D31})$$

Ciotti & Bertin (1999) derived a series expansion,  $b \approx 2n - 1/3 + 4/405n + 46/25515n^2 + 131/1148175n^3 - 2194697/3069071750n^4$ . Sérsic profiles appear ubiquitous

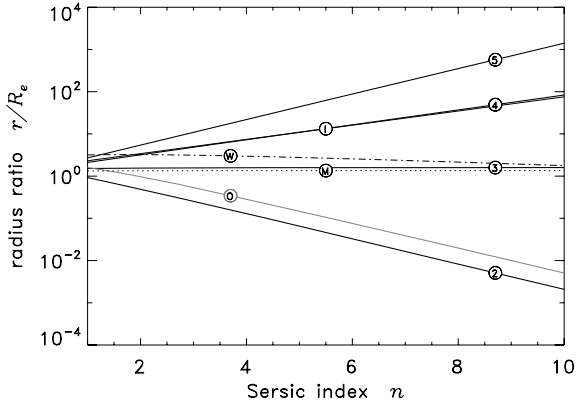


**Figure D6.** Signature radii (relative to  $R_e$ ) for Sérsic models with indices  $n$ . The curves are marked as in Fig. D2. In these halo models, the signature radii splay out enormously as  $n$  rises.

among stellar spheroids in nature, but the principal causes have not yet been shown analytically.

The cuspy density profile of Prugniel & Simien (1997),

$$\rho = \rho_s x^{-p} \exp[-b(x^{1/n} - 1)], \quad (\text{D32})$$

where  $x = r/r_s$  and  $r_s \approx R_e$ , fits the Sérsic light profile approximately. The index of the inner cusp,  $p \approx 1.0 - 0.6097/n + 0.05463/n^2$  (Lima Neto, Gerbal & Márquez 1999; Márquez et al. 2000). Expressed in terms of incomplete gamma functions, the mass and moment of inertia within some radius are

$$m = 4\pi n b^{n(p-3)} e^b \rho_s r_s^3 \Gamma[n(3-p), bx^{1/n}] \quad (\text{D33})$$

and

$$I = \frac{8\pi n}{3} b^{n(p-5)} e^b \rho_s r_s^5 \Gamma[n(5-p), bx^{1/n}]. \quad (\text{D34})$$

Evaluated as  $x \rightarrow \infty$ , the core lever radius is finite,

$$R_I = \left\{ \frac{5}{3b^{2n}} \frac{\Gamma[n(5-p)]}{\Gamma[n(3-p)]} \right\}^{1/2} r_s. \quad (\text{D35})$$

For  $n = 2$  we have  $R_I \approx 3.421 r_s$ , and for  $n = 4$  we have  $R_I \approx 7.418 r_s$ . The gravitational radius is finite but needs some numerical integration;  $R_w/r_s$  decreases with increasing  $n$ . The  $\sigma^2$  profile emerges from integration of a hydrostatic or Jeans equation, and it can be shown that the King radius vanishes,  $R_K \rightarrow 0$  as  $r \rightarrow 0$ . The dependence of the virial radius on  $(\rho_s, r_s)$  is shown by grey curves in Fig. D4.

The density index drops with radius. For all realistic  $n$ ,  $R_2$  exists uniquely, along with all higher slope radii. In general, for index  $-j$ , we have  $R_j/R_e = [n(j-p)/b]^p$ . For  $n > 1$  the consecutive integer-slope radii spread apart (vertical distribution of bold lines in Fig. D6). In contrast, finite polytropic haloes have slope radii spaced at shrinking intervals, converging at the true surface  $R$ . For  $n \gtrsim 2$ , the rotation curve peaks inside the effective radius,  $R_o < R_e$ . For  $n \gtrsim 1.2$  we have  $R_o < R_3$ . The lever radius and slope 4 radius are of similar magnitude,  $R_I \approx R_4$ , with  $R_I > R_4$  for  $n \lesssim 5$ . For  $n \geq 1$  we

have  $R_I \geq R_3$ . These signature inequalities are potentially testable by gravitational lensing and kinematic studies in halo outskirts.

## D11 Comparisons

Theoretical, numerical and observational halo models are in principle testable by measuring enough of their signature radii, derived from three-dimensional and projected quantities. Table D1 characterizes gasless polytropic halo models with various  $F$  values, and compares them to other models from the literature.

The density slope radii are the major discriminants between halo models. Isothermal and pseudo-isothermal models have no  $R_3$  radius, while the Hubble, NFW and Burkert models have  $R_3 = \infty$ . Galaxy densities in clusters appear to drop at least as steeply as  $r^{-3}$  in the outskirts (Carlberg et al. 1997; Adami et al. 2001). If this trend persists infinitely then it would fit NFW or Burkert interpretations. However, the detection of steeper slopes (by any technique) would call for more sophisticated models. All of the polytropic, King and Sérsic models have finite  $R_2$  and  $R_3$ , set in ratios depending on  $F$ ,  $c$  and  $n$ , respectively. In Sérsic models, the consecutive slope radii spread widely apart, but in the polytropes and King models these radii converge. Low-concentration King models have somewhat evenly spread values of  $\{R_2, R_3, R_4, \dots\}$  but for high concentrations  $R_2 \ll R_3 \sim R_e$ , and so the halo could be mistaken for an isothermal or NFW shape if it were probed at intermediate radii only. For finite polytropic haloes,  $R_2/R$ ,  $R_3/R$ ,  $R_4/R$ ,  $R_w/R$  and  $R_o/R$  remain similar to each other in order of magnitude (even as  $F \rightarrow 10$ ), while the projection scales  $R_\Sigma/R$  and  $R_e/R$  shrink slower with increasing  $F$ .

As their  $I$  and  $R_I/R$  values show, the concentrations and rotational properties of Hubble, NFW, Burkert and Hernquist models are hard to define. In one sense the mass is centrally concentrated. On the other hand, the outskirts dominate  $I$ . Therefore the ability to spin such a halo up or down (e.g. in tidal interactions between unbound neighbours) depends on an ad hoc truncation. The unphysical inability of simulacra to self-truncate may be part of the ‘angular momentum problem’ of simulated galaxy formation. The polytropic, King and Sérsic models are finite and consistent with respect to  $I$ .

Any real, isolated halo detaches from the Hubble flow possessing finite mass and energy. Its radius may also become finite, either due to intrinsic self-truncation (e.g. of a polytrope) or extrinsic harassment and evaporation (e.g. King models). Infinite models cannot be a final or comprehensive description of any real halo. They must be regarded as provisional approximations only. The best physically motivated, consistent and plausible models are the King, Sérsic and general polytropic descriptions. It is unclear how a Sérsic model should adapt in a potential shared with other components, so it was unsuitable as the basis for our present study. We chose the polytropic scenario, although a generalized King model has scope to represent a halo suffering surface evaporation or tidal truncation.

This paper has been typeset from a  $\text{\TeX}/\text{\LaTeX}$  file prepared by the author.